Mode control
with ultra-short pulse written
fiber Bragg gratings

DISSERTATION

zur Erlangung des akademischen Grades
doctor rerum naturalium (Dr. rer. nat.)

vorgelegt dem Rat der Physikalisch-Astronomischen Fakultät
der Friedrich-Schiller-Universität Jena

von Dipl.-Phys. Jens Ulrich Thomas
geboren am 5. März 1981 in Alzenau

1. Gutachter: Prof. Dr. Stefan Nolte, Friedrich-Schiller-Universität Jena

2. Gutachter: Prof. Dr. Hartmut Bartelt, Friedrich-Schiller-Universität Jena

3. Gutachter: Prof. Dr. Axel Schülzgen, University of Central Florida

Datum der Disputation: 5.1.2012

Contents

1 Introduction

Modern optics greatly profits from routing light with glass fibers instead of mirrors, prisms and lenses. Inside a fiber, the light is confined to a number of certain transversal states called "modes", that propagate along the fiber. The smaller the transversal dimensions of the light conduit, the fewer the number of modes. Eventually the conduit can be made so narrow that it only supports a single mode. With such single mode fibers, signals can be transmitted with very low losses over very long distances [Kao66]. Today, nearly all terrestrial telecommunication networks rely on optical fibers. Multi mode fibers on the other hand find wide-spread application as sensors. Higher order modes in such fibers can be harnessed to detect any changes to the fiber, like bends or twists as well as changes to its exterior, like temperature and refractive index. These robust, low cost sensors are applied in many different areas, ranging from life-science to modern architecture [Ker96].

Cost and efficiency of high power lasers are improved by using rare earth doped glass fibers as a gain medium instead of crystals: Firstly, the exceptional thermo-optical properties allow to significantly reduce the number of active cooling elements in the laser setup. Secondly, almost all of the pump light can be converted due to the long interaction length of the fiber. However, the downside of this geometry is that the tight confinement also enforces non-linear effects like stimulated Raman scattering, that ultimately hamper power scaling. In order to reduce these effects, the power density has to be reduced by increasing the cross-section of the guiding core. Within the last decade, power scaling to the kilo Watt regime has been enabled by *large mode area fibers* (LMA), that support only a single mode despite their large cross-section [Tün05]. A new approach for fiber setups with ultra-large cross-sections are multi mode fibers, that are enabled to lase at a high order mode with the appropriate filters [Ram08].

For all the aforementioned applications of fibers, there is a great demand for integrated solutions which replace bulk with fiber integrated components. The most prominent example are intra core fiber gratings. They can be used as narrow or broad band filters, reflectors and also as mode converters [Hil78, Hil90]. These diffraction gratings are realized as a periodic refractive index change within the core. Reflectors can be realized with short period gratings. Typically, such a *fiber Bragg grating* (FBG) has a short period of less than one micro meter. In contrast, fiber gratings designed to couple power between forward propagating modes only need to overcome a small phase difference. Consequently, the period of a *long period grating* (LPG) can range from several hundred micrometer to a millimeter or longer.

Established fiber grating writing approaches rely on the index change that arises of one photon absorption of UV light. Because the band gap of the glass is usually too large for these processes, it has to be artificially lowered by introducing defects. Thus, in a preceding procedure, the core glass is doped with germanium or boron or is loaded with hydrogen. Afterwards, the core is exposed with UV laser light for the final grating inscription [Kas99]. This way fiber gratings with elaborately designed spectral features can be realized in single mode fibers [BH04]. However, this approach is difficult to apply to the rare earth doped fibers without compromises, because a careful balancing of the different dopant concentrations is required [Loh98, PM05, Jet07]. Additionally, pre-processing and exposure times increase with core size. A common workaround is to realize the fiber grating in standard photosensitive fibers and to splice this piece of fiber to the active fiber. For this solution, the mode fields of active and grating fiber need to be matched, which often requires elements like tapers. While these solutions work well at low powers, they become the bottleneck for power scaling.

In the last decade, ultra short pulse laser have gained a lot of attention since they enable high precision micro-machining of metals [Nol97], glasses [Dav96, Nol03, Gat08] and crystals [Tho11a]. In transparent media, focussed ultra short pulses can supply enough intensity to trigger nonlinear absorption that eventually leads to permanent structural changes [Ito06]. Since these changes are confined to the focal volume, three-dimensional structures can be realized *inside* the material by translating the sample [Nol03, Gat08]. Nowadays, ultra short lasers are also increasingly employed for fiber grating inscription

[Fer01, Mih04, Mar04, Tho07, Bec08]. Due to the non-linear absorption processes ultra short laser pulses enable, they allow for

- inscription in non photo sensitive fibers [Fer01],

- especially in rare earth doped fibers [Mar04, Wik06] and

- non-sinusoidal gratings, displaying strong higher order Fourier reflections [Sme07],

- that provide both high contrast and low insertion losses [Mar10].

In addition, very resilient gratings can be inscribed, that withstand temperatures of up to 1000° C [Mar05].

Ultra short pulse lasers enable fiber gratings largely independent of the fiber geometry: The photo sensitivity of the core no longer restricts the refractive index changes. Instead, the cross-section of the grating can be shaped by controlling the focus during inscription. *Large cross-section fiber Bragg gratings* (LCFBG) can be realized, which cover the whole core of a fiber and its surrounding cladding as well as *highly localized FBG* (HLFBG) which only affect a small part of the core. This thesis explores the resulting possibilities for tailoring few and multi-mode fiber gratings.

The work is structured as follows: **Chapter 2** reviews the coupled mode theory for multi mode fiber gratings. In **chapter 3**, the coupling properties that directly follow from the nature of the fiber modes are identified. These findings are essential for understanding how the grating cross-section can be used to support or suppress coupling between different mode classes. The technological approaches to realize FBG with tailored cross-section with ultra short pulse laser inscription are discussed in **chapter 4**. **Chapter 5** details how mode coupling in single and few mode LMA fibers can be controlled with ultra short pulse written LCFBG. The possibilities to access higher order modes provided by HLFBG are explored in **chapter 6**. The last **chapter 7** discusses the impact of these findings for selected applications. Concluding remarks and an outlook on future applications are given in **chapter 8**.

2 Fundamentals of fiber Bragg gratings

The coupled mode theory is a well-established, straight forward approach that allows for accurate computation of the spectral characteristics of integrated waveguide devices [Kog79]. T. Erdogan specialized that framework for cylindrical fibers, providing an analytical apparatus for conventional fiber Bragg gratings (FBG) [Erd96, Erd97a, Erd97b, Erd00].

Sec. 2.1 and Sec. 2.2 recapitulate the coupled waveguide mode theory, closely following the classic treatment by Herwig Kogelnik [Kog79]. After a short summary of the fiber modes and their notation (Sec. 2.3), Kogelnik's expressions are adapted for fiber gratings in Sec. 2.4. Deviating from Erdogan's treatment [Erd97b], a more generalized expression for the longitudinal grating structure is used. This Fourier expansion allows to correctly render higher order resonances of non-sinusoidal gratings.

2.1 Waveguide modes

The guiding properties of a longitudinally invariant waveguide are determined by its dielectric constant

$$\epsilon = \epsilon_0 n^2(x, y), \tag{2.1}$$

which depends on its transversally varying refractive index profile (Fig. 2.1). The behavior of the complex electric and magnetic fields can be fully described with Maxwells equations. For fields with periodic time dependence of frequency $\omega = 2\pi c/\lambda$, they can be written down as

$$\nabla \times \mathbf{E} = -i\omega\mu_0\mathbf{H}, \tag{2.2a}$$

$$\nabla \times \mathbf{H} = i\omega\epsilon\mathbf{E} + i\omega\mathbf{P}, \tag{2.2b}$$

assuming constant permeability. The boundary conditions are set by the discontinuities of the dielectric constant. Solving this system for a lossless, source free medium ($\mathbf{P} = 0$) yields a set of orthogonal solutions called modes. The solutions of (Eq. 2.2) are a linear, orthogonal set of Eigenmodes.
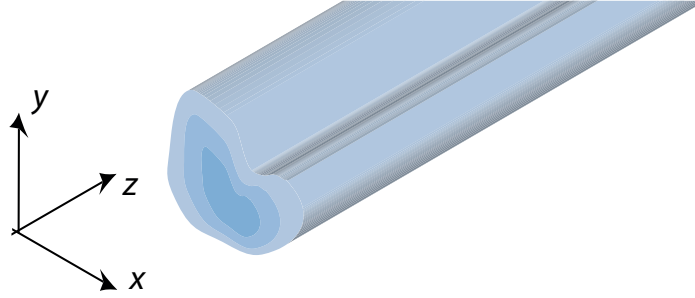

Fig. 2.1 Schematic of an arbitrary waveguide geometry, which remains constant along one axis (z)

Because of the z- invariance, the forward traveling solutions have the form

$$\mathbf{E}_\nu(x, y, z) = \mathbf{e}_\nu(x, y) \exp(-i\beta_\nu z), \tag{2.3}$$

$$\mathbf{H}_\nu(x, y, z) = \mathbf{h}_\nu(x, y) \exp(-i\beta_\nu z). \tag{2.4}$$

In the following abstract labels μ and ν are used as a short hand notation that will be replaced with two integer mode indices[1]. Here the propagation constant β_ν has been introduced, which is positive and real for bound modes.

The modes are normalized by the magnitude of the time averaged Poynting-vector

$$\langle \mathbf{S}_{\nu\mu} \rangle_t = \iint \mathrm{d}x\mathrm{d}y \ \Re(\mathbf{S}_{\nu\mu}) = \frac{1}{2} \iint \mathrm{d}x\mathrm{d}y \ \Re(\mathbf{e}_\nu \times \mathbf{h}_\mu^*)_z$$

$$= \frac{1}{4} \iint \mathrm{d}x\mathrm{d}y \ (\mathbf{e}_\nu \times \mathbf{h}_\mu^* + \mathbf{e}_\nu^* \times \mathbf{h}_\mu)_z = \delta_{\nu\mu} \quad (2.5)$$

to be equal to 1 Watt for $\nu = \mu$ and zero for $\nu \neq \mu$. Any transversal field can now be expanded in terms of modes to be

$$\mathbf{E}^\mathrm{T} = \sum_\nu (a_\nu + b_\nu)\mathbf{e}_\nu^\mathrm{T}, \qquad \mathbf{H}^\mathrm{T} = \sum_\nu (a_\nu - b_\nu)\mathbf{h}_\nu^\mathrm{T}, \tag{2.6}$$

---

[1] In the case of the vectorial fiber modes μ is to be replaced with lm and ν with $l'm'$, ($\mu = \nu$ is when $l = l'$ and $m = m'$).

where a_ν are the complex coefficients for the forward and b_ν for the backward traveling modes. All vectors marked with T are in the plane perpendicular to the propagation direction z, with their z component being zero. Using the orthonormality relation (Eq. 2.5), these coefficients equate to

$$a_\nu = \frac{1}{4} \iint \mathrm{d}x\mathrm{d}y \; (\mathbf{E}^\mathrm{T} \times \mathbf{h}_\nu^* + \mathbf{e}_\nu^* \times \mathbf{H}^\mathrm{T}),$$ (2.7)

$$b_\nu = \frac{1}{4} \iint \mathrm{d}x\mathrm{d}y \; (\mathbf{E}^\mathrm{T} \times \mathbf{h}_\nu^* - \mathbf{e}_\nu^* \times \mathbf{H}^\mathrm{T}).$$ (2.8)

2.2 Coupled mode theory

Only in a perturbed waveguide, power can be exchanged between modes. It is common to introduce these perturbations in (Eq. 2.2) via a non-zero polarization vector $\mathbf{P}(x, y, z)$ for the resulting field $\mathbf{E}_1$. The divergence of the power cross-product can then be written as

$$\nabla \cdot (\mathbf{E}_1 \times \mathbf{H}_2^* + \mathbf{E}_2^* \times \mathbf{H}_1) = -i\omega \mathbf{P} \cdot \mathbf{E}_2^*,$$ (2.9)

which becomes

$$\iint \mathrm{d}x\mathrm{d}y \; \frac{\partial}{\partial z}(\mathbf{E}_1 \times \mathbf{H}_2^* + \mathbf{E}_2^* \times \mathbf{H}_1)_z = -i\omega \iint \mathrm{d}x\mathrm{d}y \; \mathbf{P} \cdot \mathbf{E}_2^*,$$ (2.10)

by applying the divergence theorem. Without loss of generality, the unperturbed field consists of only one mode $\mathbf{E}_2 = \mathbf{e}_\mu$. The resulting field $\mathbf{E}_1$ is a linear combination of the transversal modes as in (Eq. 2.6). The expansion coefficients are now z-dependent by

$$\frac{\partial a_\mu}{\partial z} + i\beta_\mu a_\mu = -i\frac{\omega}{4} \iint \mathrm{d}x\mathrm{d}y \; \mathbf{P} \cdot \mathbf{e}_\mu^*$$ (2.11)

$$\frac{\partial b_\mu}{\partial z} - i\beta_\mu b_\mu = i\frac{\omega}{4} \iint \mathrm{d}x\mathrm{d}y \; \mathbf{P} \cdot \mathbf{e}_\mu^*.$$ (2.12)

The slowly varying part of these coefficients can be separated from the fast oscillations of the propagating part by

$$a_\mu = A_\mu \exp(-i\beta_\mu z) \qquad \text{and} \qquad b_\mu = B_\mu \exp(i\beta_\mu),$$ (2.13)

which yields the formal coupled mode equations

$$\frac{\partial A_\mu}{\partial z} = -i\frac{\omega}{4} \iint \mathrm{d}x\mathrm{d}y \; \mathbf{P} \cdot \mathbf{e}_\mu^* \exp(i\beta_\mu z)$$ (2.14)

$$\frac{\partial B_\mu}{\partial z} = i\frac{\omega}{4} \iint \mathrm{d}x\mathrm{d}y \; \mathbf{P} \cdot \mathbf{e}_\mu^* \exp(-i\beta_\mu z).$$ (2.15)

Evidently there is no power exchange in absence of sources ($\mathbf{P} = 0$). The formal coupled mode equations are exact and can be used to describe all optical mode conversion processes which can be modeled by $\mathbf{P}$. Most commonly are scalar perturbations of the dielectric constant, that result in

$$\mathbf{P} = \Delta\epsilon\mathbf{E}. \tag{2.16}$$

The impact of periodically modulated ϵ will be discussed in detail in Sec. 2.4. Also common are tensor perturbations of the form $P_{ijk} = \Delta\epsilon_{ij}E_k$, as provided with materials with high second order nonlinear susceptibility, e.g. $\Delta\epsilon_{ij} = \epsilon_0\chi_{ijk}^{(2)}E_k$.

Assuming a scalar perturbation, the transversal parts of $\mathbf{P}$ can be evaluated by the linear combination (Eq. 2.6) to

$$\mathbf{P}^T = \Delta\epsilon\mathbf{E}^T = \Delta\epsilon\sum(a_\nu + b_\nu)\mathbf{e}_\nu^{\mathrm{T}}. \tag{2.17}$$

The longitudinal parts are not orthogonal but can be derived [Kog79] to be

$$P_z = \Delta\epsilon E_z = \frac{\Delta\epsilon}{\epsilon + \Delta\epsilon}\frac{1}{i\omega}\nabla^T \times \mathbf{H}^T = \frac{\Delta\epsilon}{\epsilon + \Delta\epsilon}\sum(a_\nu - b_\nu)e_{z\nu} \tag{2.18}$$

by using the Maxwell equations (Eq. 2.2). The differential equations for the slowly varying amplitudes are then

$$\frac{\mathrm{d}A_\mu}{\mathrm{d}z} = -i\sum_\nu\{A_\nu(K_{\nu\mu}^T + K_{\nu\mu}^z)\exp[-i(\beta_\nu - \beta_\mu)z]$$

$$+ B_\nu(K_{\nu\mu}^T - K_{\nu\mu}^z)\exp[i(\beta_\nu + \beta_\mu)z]\} \tag{2.19a}$$

$$\frac{\mathrm{d}B_\mu}{\mathrm{d}z} = i\sum_\nu\{A_\nu(K_{\nu\mu}^T - K_{\nu\mu}^z)\exp[-i(\beta_\nu + \beta_\mu)z]$$

$$+ B_\nu(K_{\nu\mu}^T + K_{\nu\mu}^z)\exp[i(\beta_\nu - \beta_\mu)z]\}, \tag{2.19b}$$

where the transversal and perpendicular coupling coefficients

$$K_{\mu\nu}^T = \frac{\omega}{4}\iint_{-\infty}^{+\infty}dxdy\Delta\epsilon\mathbf{e}_\nu^{\mathrm{T}} \cdot \mathbf{e}_\mu^{\mathrm{T}*} \tag{2.20}$$

$$K_{\mu\nu}^z = \frac{\omega}{4}\iint_{-\infty}^{+\infty}dxdy\frac{\Delta\epsilon \cdot \epsilon}{\epsilon + \Delta\epsilon}e_\nu^z \cdot e_\mu^{z*}. \tag{2.21}$$

determine how a mode μ couples with a mode ν. The most prominent feature in (Eq. 2.19) are the oscillating complex exponential functions on the right hand side

(RHS). Here the oscillating frequency in z-direction is controlled by the difference of the propagation constants for modes traveling into the same direction and the sum for opposed modes. Efficient non-oscillating conversion occurs for a constant RHS. For these cases, the coupling coefficients have to be matched with the phase of the propagating modes. This can be achieved with a periodic $\Delta\epsilon$ as detailed in Sec. 2.4. Also note that for co-directional modes, the $\nu = \mu$ term is automatically phase matched, the so-called self-coupling term.

2.3 Fiber modes

The bound modes propagating in positive z-direction of a cylindrical symmetric wave-guide have the form

$$\mathbf{E}_{lm}(r, \phi, z) = \mathbf{e}_{lm}(r) \exp(i\phi l) \exp(-i\beta_{lm}z), \tag{2.22a}$$

$$\mathbf{H}_{lm}(r, \phi, z) = \mathbf{e}_{lm}(r) \exp(i\phi l) \exp(-i\beta_{lm}z), \tag{2.22b}$$

with $l = 0, \pm 1, \pm 2, \ldots$ being the azimuthal and $m = 1, 2, \ldots$ the radial index. The propagation along the z-axis is expressed with the second exponential terms of Eq. 2.22 (a,b). The propagation constant $\beta_{lm}(\lambda)$ is positive and real. It is also common to characterize a mode with its effective refractive index $\bar{n}_{lm} = c\beta_{lm}/\omega$.

The fields of modes with $l = 0$ are cylindrical symmetric and either purely azimuthally or radially polarized. The electric field of an azimuthally polarized mode is always parallel to a cylindrical surface. Thus the electric field has no z-component and such modes are transversally electric (TE). The same holds for the magnetic field of fully radially polarized modes, which are transversally magnetic (TM). In contrast, all modes with $l \neq 0$ always have longitudinal electric and magnetic field components. They are called hybrid modes and are denoted EH or HE depending on their transversal fields, as will be detailed in chapter 3. Historically, the fiber modes with no cut-offs, the so-called *fundamental* modes are designated $HE_{1,m}$ [Sni61a]. They represent a special class of hybrid modes, because they are linearly polarized. Of all modes, the mode with the highest effective refractive index $\bar{n}$ is the fundamental $HE_{1,1}$ mode. Modes with $l \neq 0$ always appear in degenerate pairs, since $\beta_{lm} = \beta_{-lm}$. They can be linearly

combined by addition or subtraction. These combinations are called *even* and *odd* modes respectively [Sny78, Sny83].
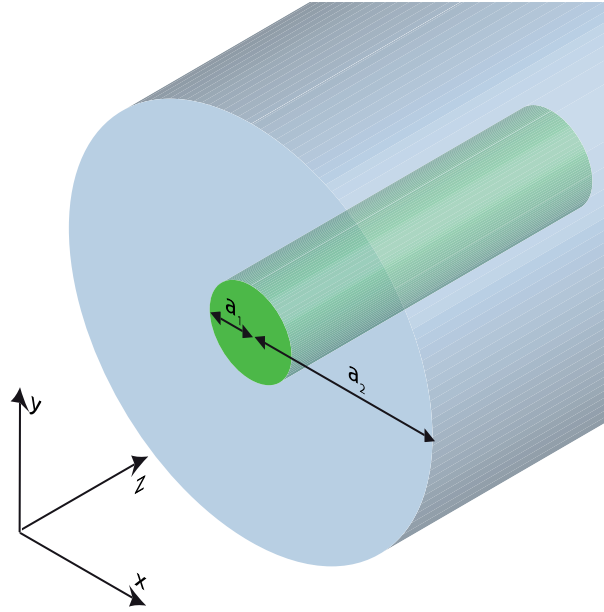

Fig. 2.2 Schematic of a step index fiber. Light can be guided within the core of higher refractive index and also within the cladding, if its refractive index is higher than the exterior.

The most prominent fiber geometry is that of a two step-index-fiber (Fig. 2.2), consisting of a core of refractive index n_1 and radius a_1, surrounded by a cladding of lower refractive index n_2 and radius a_2. If the index contrast between core and cladding is small, the fields in the core can be expressed in terms of scalar modes [Sal91]. The dimensionless parameter

$$V = \frac{2\pi a_1}{\lambda}\sqrt{n_1^2 - n_2^2} \tag{2.23}$$

depends on the free space wavelength λ and yields the number of scalar mode. The radial part $\mathbf{e}_{lm}(r) \propto J_l(ur)$ of the fields (Eq. 2.22) are then proportional to Bessel functions, with $u = (2\pi/\lambda)\sqrt{n_1^2 - \bar{n}^2}$. A core mode is guided within the core, if $ua_1 < V$. If $V < 2.4$, the radial core fields have no root, thus only one mode can propagate and the fiber is single mode (see also Section 3.2). For large V, the number of modes is $M \approx 4V^2/\pi^2$.

The scalar solutions can be related to the true vector modes of the fiber via linearly polarized LP(p,q) pseudo-modes characterized by the azimuthal index $p = 0, 1, 2\ldots$ and the radial index q [Bla10]. There are two sets of LP polarized pseudo modes: LP_x modes,

which are polarized along the x-axis and LP_y-modes. The fundamental $\mathrm{LP}_x(0,\mathrm{q})$ and $\mathrm{LP}_y(0,\mathrm{q})$ are directly proportional to the true even and odd $\mathrm{HE}_{1,m}$ modes. Since the fields of the higher azimuthal order ($p > 0$) pseudo modes exhibit an azimuthal dependence, each higher order mode must have a degenerate counterpart in order to take its rotation into account. Analog to the true fiber modes discusses above, these pseudo modes are referred to as "even" and "odd" as well. Thus, for each $p > 0$, there are four pseudo modes. Each of them is a superposition of two true vector modes. For $p = 1$ they are either the sum or difference of the $\mathrm{TE}_{0,m}$ or $\mathrm{TM}_{0,m}$ with even or odd $\mathrm{HE}_{2,m}$ modes. For $p > 1$ they can be formed with even or odd $\mathrm{EH}_{p-1,m}$ and $\mathrm{HE}_{p+1,m}$ modes [Bla10, Sny78].

2.4 Fiber gratings

In order to achieve power transfer between the fiber modes, the fiber has to be manipulated to exhibit a polarization vector (Eq. 2.16). The linear way to let the modes interact is to induce a weak index modification $\Delta n(r, \phi, z)$ within the fiber that perturbs the dielectric profile (Eq. 2.1) of the fiber by

$$\Delta\epsilon(r, \phi, z) = \epsilon_0 \left((n(r, \phi) + \Delta n(r, \phi, z))^2 - n^2(r, \phi) \right) \approx 2\epsilon_0 n(r, \phi)\Delta n(r, \phi, z). \quad (2.24)$$

An arbitrary refractive index profile of period Λ along the fiber axis z (Fig. 2.3 (a)) can be expressed as superposition of sinusoidal gratings of period Λ/m with

$$2\epsilon_0 n(r, \phi)\Delta n(r, \phi, z) = \epsilon_0 n(r, \phi) \left(\Delta n_0(r, \phi) + \sum_{m=1}^{\infty} \Delta n_m(r, \phi)2\cos(k_m z) \right), \quad (2.25)$$

where the wavenumber $k_m = 2\pi m/\Lambda$ and the integer m denotes the Fourier order. The Fourier terms $\Delta n_m(r, \phi)$ can be computed from the refractive index profile with

$$\Delta n_0(r, \phi) = \tfrac{4}{\Lambda} \int_0^{\Lambda/2} \mathrm{d}z \Delta n(r, \phi, z) \quad \text{and} \quad (2.26\mathrm{a})$$

$$\Delta n_m(r, \phi) = \tfrac{4}{\Lambda} \int_0^{\Lambda/2} \mathrm{d}z \Delta n(r, \phi, z) \cos(k_m z) \quad (2.26\mathrm{b})$$

For a rectangular, periodic refractive index modulation of width w (Fig. 2.3 (b)) as defined for a $z \in [-\Lambda/2, \Lambda/2]$ with

$$\Delta n(r, \phi, z) = \begin{cases} 0 & |z| > w/2 \\ \Delta n_{\max} & |z| \leq w/2 \end{cases} \quad (2.27)$$

the Fourier integrals (Eq. 2.26) can be evaluated to

$$\Delta n_0(r, \phi) \quad = \frac{2w}{\Lambda} \Delta n_{\max}(r, \phi) \qquad \text{and} \tag{2.28a}$$

$$\Delta n_m(r, \phi) \quad = \frac{2}{\pi m} \sin\left(\pi m \frac{w}{\Lambda}\right) \Delta n_{\max}(r, \phi). \tag{2.28b}$$
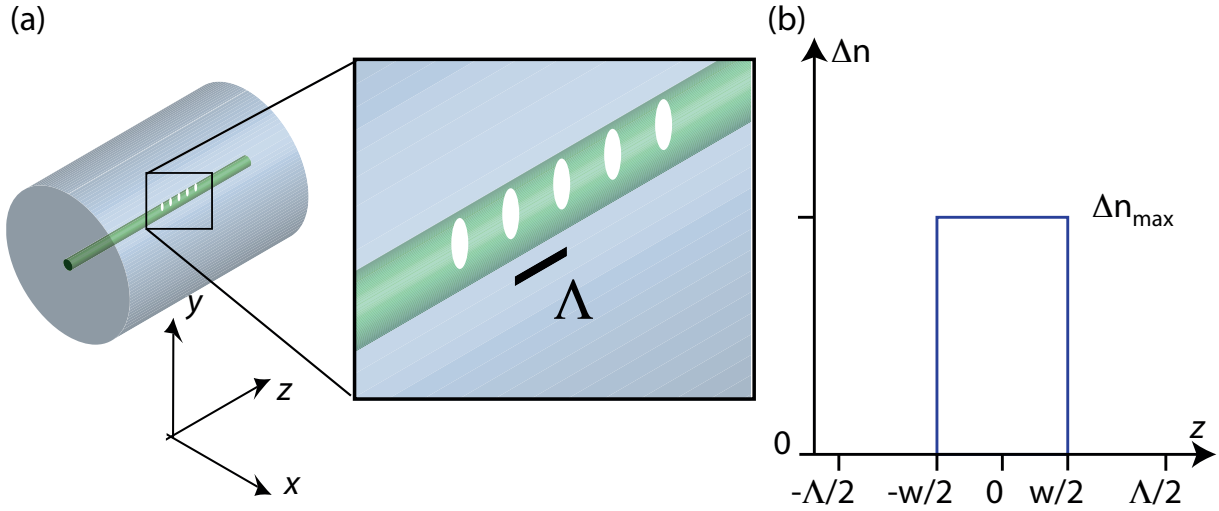

Fig. 2.3 Schematic of an intra-core fiber grating of period Λ (a) and sketch of a periodic rectangular refractive index profile (b).

Since the longitudinal fields of the fiber modes are usually small compared to the transversal ones $K^T \gg K^z$, it is a good approximation to neglect longitudinal coupling [Erd97b]. Inserting the refractive index profile (Eq. 2.25) into the transversal coupling coefficient (Eq. 2.20) yields

$$K_{\mu\nu}^T = \kappa_{\mu\nu}^0 + \sum_{m>0} 2\cos(k_m z)\kappa_{\mu\nu}^m, \tag{2.29}$$

with

$$\kappa_{\mu\nu}^m = \epsilon_0 \frac{\omega}{4} \iint \mathrm{d}r \ \mathrm{d}\phi \ r\, n(r,\phi)\Delta n_m(r,\phi)\mathbf{e}_\nu^\mathrm{T} \cdot \mathbf{e}_\mu^{\mathrm{T}*} \exp[i(l_\nu - l_\mu)\phi]. \tag{2.30}$$

Many terms of the coupled mode equations (Eq. 2.19) do not contribute much to the power exchange of the modes, since they are oscillating with a high frequency. Basically these are all the exponential terms with an argument that cannot become zero. Using

this so-called synchronous approximation [Kog79] after inserting (Eq. 2.29) leads to

$$\frac{\mathrm{d}A_\mu}{\mathrm{d}z} = -iA_\mu\kappa^0_{\mu\mu} - i\sum_{m>0}\sum_{\nu\neq\mu}\{A_\nu\kappa^m_{\nu\mu}(e^{-i(\beta_\nu-\beta_\mu+k_m)z} + e^{-i(\beta_\nu-\beta_\mu-k_m)z}) \tag{2.31}$$

$$+ B_\nu\kappa^m_{\nu\mu}(e^{i(\beta_\nu+\beta_\mu+k_m)z} + e^{i(\beta_\nu+\beta_\mu-k_m)z})\} \tag{2.32}$$

$$\frac{\mathrm{d}B_\mu}{\mathrm{d}z} = iB_\mu\kappa^0_{\mu\mu} + i\sum_{m>0}\sum_{\nu\neq\mu}\{A_\nu\kappa^m_{\nu\mu}(e^{i(\beta_\nu+\beta_\mu+k_m)z} + e^{i(\beta_\nu+\beta_\mu-k_m)z}) \tag{2.33}$$

$$+ B_\nu\kappa^m_{\nu\mu}(e^{i(\beta_\nu-\beta_\mu+k_m)z} + e^{i(\beta_\nu-\beta_\mu-k_m)z})\}. \tag{2.34}$$

Still, even for these equations most terms do not contribute: Only at certain wavelengths, the propagation constants match the grating wavenumber and the arguments of the exponential functions become zero. These are the resonances of the grating, where the modes do interact. Usually, the relevant spectrum of a grating is narrow enough, so that only one Fourier component Δn_m has to be taken into account. The resonances are then referred to as mth order.

Mode coupling between modes travelling in the same direction occurs at

$$k_m = |\beta_\nu - \beta_\mu|. \tag{2.35}$$

Because the phase difference between the modes is small, so is the grating wavenumber. Thus the grating periods can become large. Such a grating is called a long period grating (LPG).

In order to couple the light into a counter-propagating mode, a much larger phase

$$k_m = \beta_\nu + \beta_\mu \tag{2.36}$$

has to be provided by the wavenumber. A grating with such a short period is called a fiber Bragg grating (FBG).

In general, for a given k_m, a grating in a fiber with N non-degenerate modes can have up to $N(N+1)/2$ resonances:

- N so-called *self-coupling* resonances with $\mu = \nu$ and

- $N(N-1)/2$ *mode-converting* resonances, with $\mu \neq \nu$.

The magnitude of these peaks depends on the coupling integral (Eq. 2.30). Thus, depending on the cross-section of the fiber grating, many resonances might not appear. This will be discussed in detail in chapter 3.

3 General coupling properties of the fiber modes

The aim of this chapter is to determine which classes of fiber modes can efficiently interact with each other through a given fiber grating. Primarily, the coupling properties of the modes are set by the symmetry properties of the fiber modes. If the transversal shape of the fiber grating follows those symmetries, coupling to different classes of fiber modes can be enhanced or suppressed. In the first section fundamental coupling properties are summarized that directly follow from the cylindrical geometry of the fiber. In the following sections, these concepts are enlarged upon for step index fiber geometries. Sec. 3.2 details the coupling properties of the core mode. The coupling properties of the cladding mode can be classified by their core fields as will be shown in Sec. 3.4. The chapter closes with a summary on how the geometry of the fiber cross section allows to control coupling between different azimuthal mode classes.

3.1 Fundamental coupling properties

Sec. 2.4 detailed, how the power transfer between the modes of fibers can be determined by their coupling constants. The transversal coupling constants (Eq. 2.30)

$$\kappa_{\mu\nu}^m = \epsilon_0 \frac{\omega}{4} \iint \mathrm{d}r\ \mathrm{d}\phi\ r\, n(r,\phi)\Delta n_m(r,\phi)\mathbf{E}_\nu^\mathrm{T} \cdot \mathbf{E}_\mu^{\mathrm{T}*}. \tag{3.1}$$

are the integrals over the product of the refractive index profile $n(r,\phi)$ of the fiber and the fiber gratings $\Delta n(r,\phi)$ with the mode overlap $\mathbf{E}_\nu^\mathrm{T} \cdot \mathbf{E}_\mu^{\mathrm{T}*}$. The latter can be used to derive some fundamental, grating independent coupling rules. Inserting the field

expression (Eq. 2.22) gives

$$\mathbf{E}_\nu^T \cdot \mathbf{E}_\mu^{T*} = \left(\mathbf{e}_\nu(r) \cdot \mathbf{e}_\mu^*(r)\right) \exp(i\phi(l_\mu - l_\nu)). \tag{3.2}$$
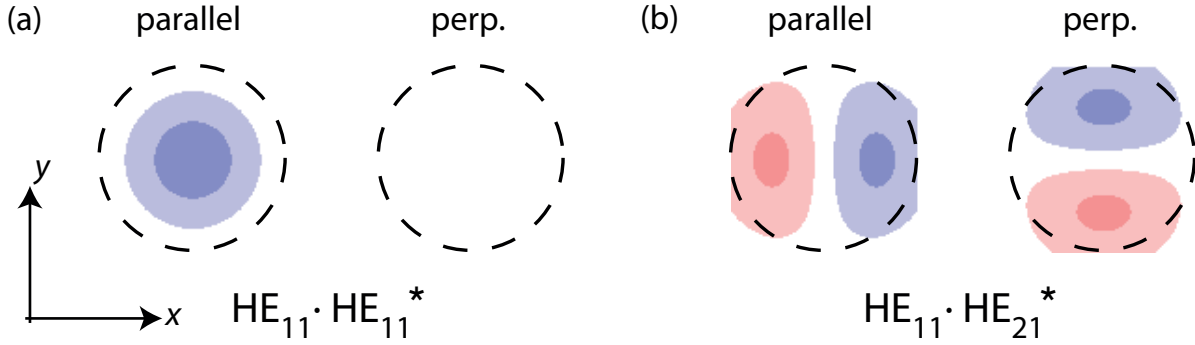

Fig. 3.1 Two exemplary overlaps: (a) displays the overlap of the fundamental core mode with itself, which is always positive; (b) displays an overlap of the fundamental mode with an higher order mode (HE$_{1,1}$), which yields positive and negative contributions. The fundamental mode is assumed to be *even*. The parallel overlap means that the second mode is also *even*, in the perpendicular case, it is *odd*.

Two examples of such an overlap are plotted in Fig. 3.1. Depending on the modes, this overlap is either

1. zero, or is

2. positive and real everywhere, or has

3. positive and negative contributions and is not necessarily real.

In the first case, the modes can never directly couple through a single grating. In the second case, the modes always couple independent of the transversal cross-section of the fiber grating. (It has to have some index change, though.) In the last category all coupling possibilities fall, that can be accessed with a transversally inhomogeneous fiber grating. This leads to the following fundamental coupling properties of the fiber modes:

1. Coupling to the similar mode is always possible, since the exponential term in (Eq. 3.2) is then equals one and the radial field product $\mathbf{e}_\nu \cdot \mathbf{e}_\nu^* > 0$ at all positions. In the following, these resonances are called *self-coupling resonances*.

2. *Mode conversion* ($\mu \neq \nu$) can be enabled by gratings that do not cover the whole mode-field, so that positive and negative contributions of radial and exponential terms of the overlap do not cancel out by integration.

Taking the vectorial nature of the radial part of the fields into account, the overlaps that are always zero can be identified:

- Coupling from a TE to a TM mode is never possible, since the field vectors ($\mathbf{e}_\nu^{\mathrm{TE}} \propto \hat{e}_\phi$, $\mathbf{e}_\mu^{\mathrm{TM}} \propto \hat{e}_r$) are at every point perpendicular to each other.

- Coupling from an even or odd LP$_x$ mode ($\mathbf{e}_\nu^{\mathrm{e}} \propto \hat{e}_x$) to an even or odd LP$_y$ mode ($\mathbf{e}_\mu^{\mathrm{o}} \propto \hat{e}_y$) is impossible for the same reason.

- Coupling is also impossible, if at least one of the modes has no electric field in the area of the fiber cross-section, where the refractive index is modulated.

More coupling properties can be derived, if the radial refractive index profile of the fiber is known. This will be shown in the following for core and cladding modes of a step index fiber.

3.2 Core mode coupling in a step-index fiber

Light in step index fibers is guided by internal reflection at fiber layers with different refractive indices. Analytic solutions for these refractive index profiles exist for cylindrical symmetric fibers with two [Sni61a] and three layers [Erd97a, Tsa89a]. While the latter are given in the Appendix A, in the following the modes derived by Snitzer [Sni61a] will be used to derive some fundamental coupling properties. The inner cylinder of radius a_1 is called the core, the outer shells are the cladding with radii a_i, where the last shell is usually used to simulate the exterior of the fiber. In the following analysis and subsequent experiments, fibers are investigated, where the refractive index of each layer n_i is assumed to be smaller than n_{i-1}, with the core having the highest refractive index. An example geometry is plotted in Fig. 2.2. Solving the dispersion relation for these geometries yields a set of discrete propagation constants, the guided modes. Their effective refractive indices reveal in which layer the mode is contained. For a single step index fiber, exposed to air $n_1 > n_2 > n_3 = 1$. In this case, if $\bar{n} > n_2$, the mode is guided

within the core, for $1 < \bar{n} < n_2$ it is contained within the cladding.

In cylindrical coordinates (r, ϕ, z), the electric $\mathbf{E}$ and magnetic $\mathbf{H}$ fields of the modes inside the core ($r < a_1$) can be expressed in terms of Bessel functions J_n of the first kind

$$E_z = \quad E_{lm}\frac{u_1^2}{\beta}P J_l(u_1 r)\sin(l\phi + \varphi)e^{i(\beta z - \omega t)} \tag{3.3a}$$

$$E_r = \quad iE_{lm}\frac{u_1}{2}\left[(1 - P)J_{l-1}(u_1 r) + (1 + P)J_{l+1}(u_1 r)\right]\sin(l\phi + \varphi)e^{i(\beta z - \omega t)} \tag{3.3b}$$

$$E_\phi = \quad iE_{lm}\frac{u_1}{2}\left[(1 - P)J_{l-1}(u_1 r) - (1 + P)J_{l+1}(u_1 r)\right]\cos(l\phi + \varphi)e^{i(\beta z - \omega t)} \tag{3.3c}$$

$$H_z = \quad E_{lm}\frac{\bar{n}}{Z_0}\frac{u_1^2}{\beta}J_l(u_1 r)\cos(l\phi + \varphi)\,e^{i(\beta z - \omega t)} \tag{3.3d}$$

$$H_r = \quad iE_{lm}\frac{\bar{n}}{Z_0}\frac{u_1}{2}\left[-\left(1 - P\frac{n_1^2}{\bar{n}^2}\right)J_{l-1}(u_1 r) + \left(1 + P\frac{n_1^2}{\bar{n}^2}\right)J_{l+1}(u_1 r)\right]\cos(l\phi + \varphi)\,e^{i(\beta z - \omega t)} \tag{3.3e}$$

$$H_\phi = -iE_{lm}\frac{\bar{n}}{Z_0}\frac{u_1}{2}\left[-\left(1 - P\frac{n_1^2}{\bar{n}^2}\right)J_{l-1}(u_1 r) - \left(1 + P\frac{n_1^2}{\bar{n}^2}\right)J_{l+1}(u_1 r)\right]\sin(l\phi + \varphi)\,e^{i(\beta z - \omega t)}, \tag{3.3f}$$

with the transverse wave vector $u_1 = (2\pi/\lambda)\sqrt{n_1^2 - \bar{n}^2}$. In the following the notation employed by Erdogan [Erd97a] is used, however, the azimuthal dependence is expressed in trigonometric rather than exponential form as in [Sni61a]. The constant $Z_0 = \sqrt{\mu_0/\epsilon_0} \approx 376.7\ \Omega$ is the electromagnetic impedance in vacuum. All constants $\bar{n}, \beta, u_1, E_{lm}$ and P depend on the mode indices l and m. Sometimes this is explicitly indicated by including the mode indices as subscripts. Each normalization constant E_{lm}^{cl} is set such that all modes carry one Watt of power (Eq. 2.5).

The azimuthal dependence is given in the trigonometric form: in contrast to the exponential form (Eq. 2.22) the azimuthal index $l \geq 0$ and a phase φ is introduced. With $\varphi = 0$ for *even* modes and $\varphi = -\pi/2$ for *odd* modes, two degenerate sets of modes are established and their superposition allows to express any angle of orientation of the mode fields. Without loss of generality, the incident field is always assumed to be even. Hence, if the mode also couples to odd modes with similar indices, the axis of polarization of the resulting pattern is rotated.

The dimensionless *mode parameter* P_{lm} in Eq. 3.3 determines the contributions of the individual Besselfunctions and thus which field components are predomiant. Tab. 3.1 summarizes different cases for P and the resulting mode designation in accordance

$P = 0$	$E_z = 0$	TE
$P \to \infty$	$H_z \to 0$	TM
$P = -1$	$\mathbf{E}^{\mathrm{T}}, \mathbf{H}^{\mathrm{T}} \propto J_{l-1}$	HE
$P = \frac{n_1^2}{n_2^2} \approx 1$	$\mathbf{E}^{\mathrm{T}}, \mathbf{H}^{\mathrm{T}} \propto J_{l+1}$	EH

Tab. 3.1 Mode parameter P and resulting core fields and designations for a step index fiber.

with Sec. 2.3.

Note that P_{lm} is closely connected to the dispersion relation, since the fields have to be continious at the core-cladding boundary. Thus, for a core bound mode ($\bar{n} > n_2$) its mode parameter becomes

$$P_{lm} = \frac{l\nu_{21}}{a_1^2(J+K)},$$

(3.4)

with

$$\nu_{21} = \frac{1}{w_2^2} + \frac{1}{u_1^2}, \qquad J = \frac{J_l'(u_1 a_1)}{u_1 J_l(u_1 a_1)}, \qquad K = \frac{K_l'(w_2 a_1)}{w_3 K_l(w_2 a_1)}.$$

and

$$u_1^2 = (2\pi/\lambda)^2(n_1^2 - \bar{n}^2), \qquad w_2^2 = (2\pi/\lambda)^2(n_2^2 - \bar{n}^2).$$

The overlap (Eq. 3.2) with the fields (Eq. 3.3) allows for evaluating, which classes of modes can couple, and what symmetry the gratings need to support this coupling. The azimuthal index $l = 0$ for TE and TM modes and $l > 0$ for all hybrid HE/EH modes. As said before, coupling from TE to TM modes is impossible, since their fields are always perpendicular. However, coupling from a hybrid mode to TE or TM is possible, since the hybrid mode has both radial and azimuthal components. The overlap

$$\mathbf{E}_\nu^{\mathrm{T}} \cdot \mathbf{E}_\mu^{\mathrm{T}*} \begin{cases} = E_\nu E_\mu u_\nu u_\mu J_{l_\nu \mp 1}(u_\nu r) J_0(u_\mu r) \cos\{l_\nu \phi + \varphi_\nu\} & \text{for HE/EH} \leftrightarrow \text{TE,} \\ = E_\nu E_\mu u_\nu u_\mu J_{l_\nu \mp 1}(u_\nu r) J_0(u_\mu r) \sin\{l_\nu \phi + \varphi_\nu\} & \text{for HE/EH} \leftrightarrow \text{TM.} \end{cases}$$

(3.5)

for this conversion has the same azimuthal symmetry l as the involved hybrid mode. Coupling within the hybrid modes can be expressed with

$$\mathbf{E}_\nu^{\mathrm{T}} \cdot \mathbf{E}_\mu^{\mathrm{T}*} \begin{cases} = E_\nu E_\mu u_\nu u_\mu J_{l_\nu-1}(u_\nu r) J_{l_\mu-1}(u_\mu r) \cos\{(l_\nu - l_\mu)\phi + \varphi_\nu - \varphi_\mu\} & \text{for HE} \leftrightarrow \text{HE,} \\ \approx E_\nu E_\mu u_\nu u_\mu J_{l_\nu+1}(u_\nu r) J_{l_\mu+1}(u_\mu r) \cos\{(l_\nu - l_\mu)\phi + \varphi_\nu - \varphi_\mu\} & \text{for EH} \leftrightarrow \text{EH,} \end{cases}$$

(3.6)

where the approximation $P \approx 1$ was used to simplify the expression for the EH modes. Here, the azimuthal dependence is set by the difference $l_\nu - l_\mu$. For $l_\nu = l_\mu$, the overlap has no azimuthal dependence. Thus, the axis of polarization is conserved and the coupling strength is independent of any asymmetries of the grating cross-section. The cosine term becomes one, if the phases φ are equal, and zero if $\phi_\nu - \phi_\mu = \pm\pi/2$. This means that coupling between even and odd hybrid modes of equal l is impossible. The overlap

$$\mathbf{E}_\nu^{\mathrm{T}} \cdot \mathbf{E}_\mu^{\mathrm{T}*} = -E_\nu E_\mu u_\nu u_\mu J_{l_\nu-1}(u_\nu r) J_{l_\mu+1}(u_\mu r) \cos\{(l_\nu + l_\mu)\phi + \varphi_\nu + \varphi_\mu\}\text{for HE} \leftrightarrow \text{EH},$$

(3.7)

for HE to EH mode coupling has always an azimuthal dependence, because the cosine follows $\phi(l_\nu + l_\mu)$.

3.3 Core mode coupling in the weak guiding limit

In case of a weakly guiding fiber, the true vector modes degenerate and add up to linearly polarized modes (Sec. 2.3). Naturally, this superposition principle appears in the overlap of the true vector modes. For example, if mode ν is a $\mathrm{LP}_{0,m} = \mathrm{HE}_{1,m}$ mode, the overlaps for $\mathrm{TE}_{0,m}$ are identical to even $\mathrm{HE}_{2,m}$. Thus coupling to these classes of modes is always equally strong and they superpose to even $\mathrm{LP}_{1,m}$. In a similar fashion, the overlap of $\mathrm{TM}_{0,m}$ falls together with the odd $\mathrm{HE}_{2,m}$. For $l_\mu > 2$ the overlaps to the $\mathrm{HE}_{l,m}$ agree with $\mathrm{EH}_{(l-2),m}$ and the equally strong conversion efficiencies would result in a $\mathrm{LP}_{l+1,m}$ mode. One can summarize the coupling properties in the weak coupling limit for the LP pseudo modes for

- $\mathrm{LP}_x \leftrightarrow \mathrm{LP}_y$ coupling is always impossible,
- even $\leftrightarrow$ even coupling is possible as well as
- odd $\leftrightarrow$ odd, whereas
- even $\leftrightarrow$ odd is possible only for inhomogenous FBG.

3.4 Cladding mode coupling in a step index fiber

A mode is guided within the cladding of the fiber, if its effective refractive index $\bar{n}$ is smaller than the refractive index of the cladding and larger than the refractive index of the exterior. Coupling from a core mode to one or more cladding guided modes is commonly referred to as *cladding mode coupling*. Since most fiber gratings are a modulation of the fiber core, the electric field overlap within that area is also the relevant quantity for predicting the coupling strength for cladding mode coupling. Thus, the relevant feature of a cladding mode is its field at the core. The aim of this section is therefore to classify the cladding modes according to this feature.

In order to properly describe cladding modes, at least two interfaces and three layers (core, cladding and exterior) have to be considered [Erd97a]. TE and TM cladding modes are either parallel or perpendicular to the cladding interfaces and their vectorial properties do not differ from their core guided counterparts. More interesting are the hybrid modes: Their vector fields at the core do change considerably depending on the radial and azimuthal order of the mode.

For the analytic solution, dispersion relation and field expressions have to take three layers into account (Eq. A.3). However, the field expressions for the core take the same mathematical form as in the simple, two layer case. This allows to characterize and classify the hybrid cladding modes in terms of their field at the core. Hence, the overlaps of the previous section can also be used to predict core-cladding mode coupling.

What changes in (Eq. 3.3) in contrast to the two layer model are the normalization constants E_{lm}, which now also have to take the amount of power into account that is guided in the cladding. Most notably, the mode parameter

$$P = P_{lm} = -\frac{\bar{n}_{lm} i \zeta_0}{n_1^2} \tag{3.8}$$

becomes more complex, since it characterizes the relative strength of the longitudinal field components and depends on the boundary conditions of the three layers.

The imaginary parameter ζ_0 is determined by the outer layers of the fiber. It is given in the appendix as part of the dispersion relation (Eq. A.3). For a single mode fiber, the P
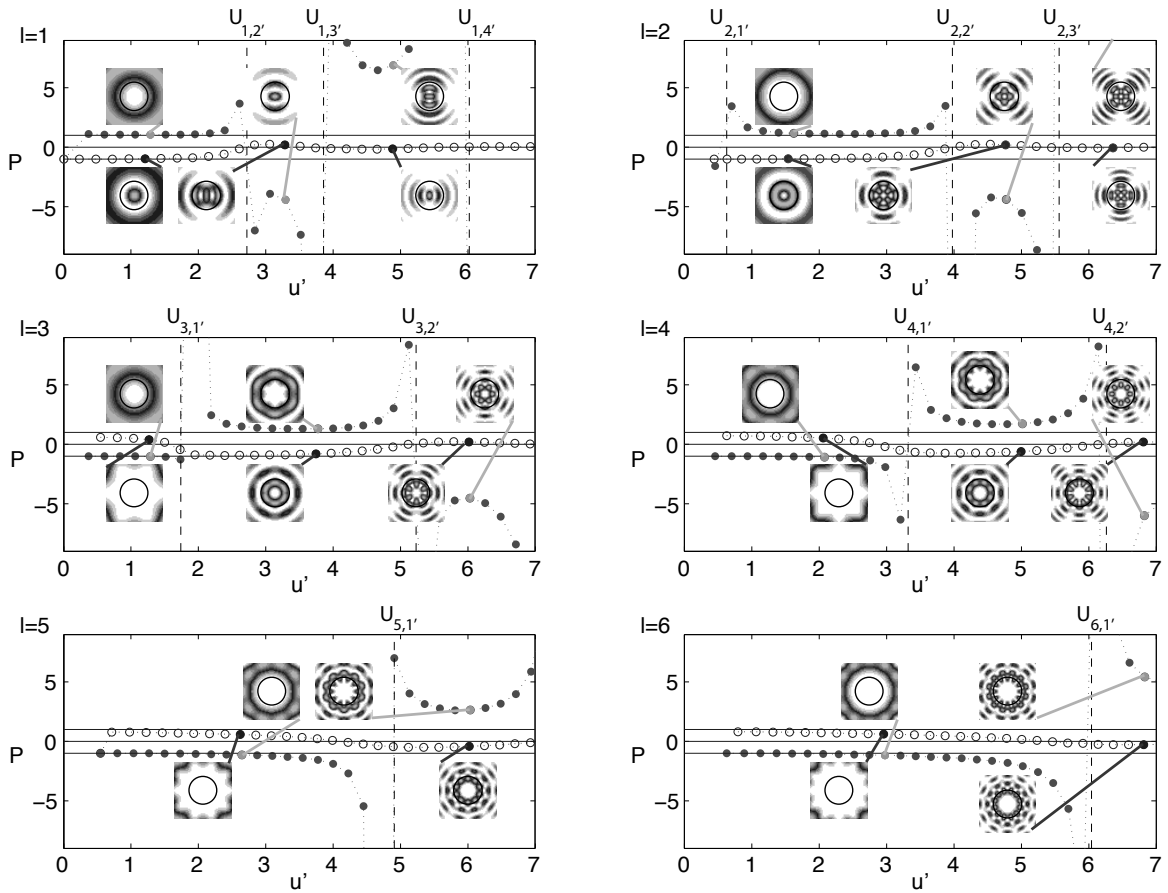
Fig. 3.2 The mode parameter P plotted for hybrid cladding modes with $l \leq 6$. Note that a normalized wave number (Eq. 3.9) has been used in order to better spread the lower order cladding modes. The hollow circles are fiber modes, that are formally HE, while filled circles mark formal EH modes. The horizontal lines are drawn for $P = -1$ and $P = 1$, highlighting the behavior of the core fields as detailed in the text.

for all modes is plotted in Fig. 3.2. For more clarity, a normalized wave vector

$$u'_{lm} = \frac{2\pi a_1}{\lambda} \frac{n_1}{n_2} \sqrt{n_1^2 - \bar{n}_{lm}^2},$$
(3.9)

has been introduced. It corresponds to the normalized frequency a cladding mode would have, if refraction on the core-cladding mode boundary would be ignored.The insets depict the intensity of the indicated modes for $r < 3a_1$.

Most strikingly in Fig. 3.2 is, that $-1 < P < n_1^2/n_2^2$ no longer holds for all modes. Consistency is regained by designating modes with $|P_{lm}| \leq 1$ as HE modes and those with $|P_{lm}| > 1$ EH modes. This way, HE and EH modes appear in strictly alternating order, marked in Fig. 3.2 as hollow and filled circles respectively. The values of P exhibit discontinuities at certain wavenumbers, where the denominator of the dispersion relation becomes zero (Eq. A.3). For reasons apparent soon, these discontinuities are called "virtual cut-offs". They are marked with vertical dashed lines in Fig. 3.2 and are referred to as $U_{l,m'}$, where l is the azimuthal index and m' an ascending integer. As it is an argument of the field expressions (Eq. 3.3), the mode parameter determines how the field intensity is shaped (insets of Fig. 3.2). It drastically changes at each virtual cut-off. For $l = 1$ modes below the $U_{1,2'}$ cut-off, $P \approx \pm 1$ as for strongly bound modes in the two-layer case. In accordance, the HE- and EH-cladding modes behave like such core modes. However, the EH modes carry almost no intensity at the core and will therefore not couple to any core mode. This changes after the $U_{1,2'}$ cut-off. Now both classes of modes exhibit some intensity within the core region. However, since $P \approx 0$ for HE and $P \ll 1$ for EH modes, these modes now have a field that is similar to TM and TE respectively. Thus, beyond that cut-off, they become *quasi-TM* and *quasi-TE*. For cladding modes with $l > 1$ the virtual $U_{l,1'}$ cut-off also marks an important regime: below this cut-off, both hybrid mode classes have no field at the core. This cut-off moves to higher and higher wavenumber for higher l. Thus it is a very good criteria to limit the azimuthal mode-classes that have to be considered for a certain wavelength range. Since $HE_{1,m}$ modes are the fundamental modes, they always guide some light within the core. Consequently, the $U_{1,1'}$ cut-off is 0.

3.5 Implications for fiber grating design

Tab. 3.2 summarizes the coupling properties derived from the overlaps in the previous sections. The possible mode conversions are sorted after the azimuthal symmetries of the overlap. The upper part of the table list the true vector modes, while the lower part details the LP pseudo vector modes. In the following the different transversal fiber grating designs will be discussed.

Tab. 3.2 Summary of possible mode conversions, sorted by the symmetry of their overlap.

Azimuthal symmetry $\cos \ell\phi$	Possible mode conversion
$\ell \geq 0$	within the same azimuthal mode class
$\ell \geq 1$	HE/EH $\leftrightarrow$ TE/TM ($\ell = l$)
	HE $\leftrightarrow$ HE, EH $\leftrightarrow$ EH ($\ell = l_\nu - l_\mu$)
$\ell \geq 2$	HE $\leftrightarrow$ EH ($\ell = l_\nu + l_\mu$)
$\ell \geq 0$	within the same azimuthal mode class
$\ell \geq 1$	LP $\leftrightarrow$ LP ($\ell = p_\nu - p_\mu$)

Due to the ease in manufacturing, the most wide spread fiber gratings are those in photosensitive step index fibers. Here, the expression for the coupling coefficient (Eq. 2.30) can be further simplified [Erd97b]. Due to the photo sensitivity and the relatively small core, solely the refractive index of the core is transversally homogeneously modified. The refractive index n_1 and the refractive index change Δn_m are hence constants and

$$\kappa_{\mu\nu}^m = \epsilon_0 n_1 \Delta n_m \frac{\omega}{4} \int_0^{a_1} r \, \mathrm{d}r \, \mathbf{e}_\nu^{\mathrm{T}}(r) \cdot \mathbf{e}_\mu^{\mathrm{T*}}(r) \int_0^{2\pi} \mathrm{d}\phi \exp[i(l_\nu - l_\mu)\phi] \qquad (3.10)$$

after inserting the electric fields of the fiber modes (Eq. 2.22). Evidently, *classic fiber gratings* can only couple between modes of the same azimuthal order l, since the last part of the integral is equivalent to the Dirac delta function $\delta(l_\mu - l_\nu)$. This selectivity however is not given for the radial index m, since the grating only integrates up to a_1. Thus mode conversion is possible: for core modes with $m_\mu \neq m_\nu$, the missing evanescent field parts at the cladding do contribute to a non-zero integral. Coupling to cladding modes of the same l is possible for the same reason. A prominent example is the conversion

of the fundamental $HE_{1,1}$ mode of a single mode fiber to $HE_{1,m}$ and $EH_{1,m}$ cladding modes [Erd97a]. With classical inscription techniques suppression of cladding mode coupling is not easily feasible, since the index change is restricted to the core. Special fiber designs are need, e.g. fibers with a depressed cladding, that shifts the cladding fields away from the core. This way, most but not all cladding mode resonances can be avoided [Hew96].

For complete suppression of all mode converting resonances, the coupling integral (Eq. 3.1) has to be equivalent to the orthogonality relation of all fiber modes (Eq. 2.5). Thus the prerequisite is that

$$n(r, \phi)\Delta n_m(r, \phi) = \text{const.} \tag{3.11}$$

for the whole cross-section of the fiber. This criteria can be weakened to only apply to the area of the overlaps of the modes of interest. For example for cladding mode coupling of the fundamental $HE_{1,1}$, its evanescent field does not have any significant contributions beyond $r > 2a_1$. A *large cross-section fiber Bragg grating* can provide these condition as will be shown in chapter 5.

Conversion between modes with different azimuthal index l requires a grating that provides at least a $\cos\phi$ dependence (Tab. 3.2). The classic means for such mode converting gratings are *tilted gratings* [Lee00]. The refractive index remains constant, but the grating planes are inclined by an angle θ to the normal of fiber axis z. Such gratings have a wavenumber $k'_m = k_m \cos\theta$ along the fiber axis. Their coupling constants are

$$\kappa_{\mu\nu}^m(z) = g_{\mu\mu}^+ \exp(ik_m z \cos\theta) + g_{\mu\nu}^- \exp(-ik_m z \cos\theta) \quad \text{with} \tag{3.12a}$$

$$g_{\mu\nu}^{\pm} = \epsilon_0 \frac{\omega}{4} n_1 \Delta n_m \int_0^{2\pi} \mathrm{d}\phi \int_0^{a_1} r\,\mathrm{d}r\, \exp(\mp ik_m r \cos\phi \sin\theta)\mathbf{E}_\nu^{\mathrm{T}} \cdot \mathbf{E}_\mu^{\mathrm{T}*} \quad \text{for } x\text{-tilt and} \tag{3.12b}$$

$$g_{\mu\nu}^{\pm} = \epsilon_0 \frac{\omega}{4} n_1 \Delta n_m \int_0^{2\pi} \mathrm{d}\phi \int_0^{a_1} r\,\mathrm{d}r\, \exp(\mp ik_m r \sin\phi \sin\theta)\mathbf{E}_\nu^{\mathrm{T}} \cdot \mathbf{E}_\mu^{\mathrm{T}*} \quad \text{for } y\text{-tilt.} \tag{3.12c}$$

The tilt angle (blaze) can be used to maximize coupling to certain higher order modes. For fiber Bragg gratings that convert in reflection, the blaze has to increase with higher order modes [Lee01].

Ideal mode converting fiber gratings however would provide a cross-section that mimics

the overlap of the desired conversion (Tab. 3.2) with

$$\Delta\epsilon(r,\phi) \propto \cos\ell\phi. \tag{3.13}$$

Up to now, there seems no fabrication process being able to realize such gratings. However, gratings that only fill a very small part of the core can exhibit a similar coupling behaviour. Since the shape and position of such a modification has to be taken into account, general expressions of $\Delta\epsilon$ do not exist and the coupling constants are directly computed from (Eq. 3.1). An example of such a *highly localized fiber Bragg grating* is investigated in detail in chapter 6.

4 Ultra short pulse inscription of fiber gratings

This chapter details the inscription methods used to realize the FBG with ultra short laser pulses. The first section summarizes the properties of ultra short pulse modifications in glass fibers. In the second section, the influence of the focussing conditions on the feature size are discussed. Phase mask scanning with low numerical aperture (NA) cylindrical optics can be used to achieve large cross section fiber Bragg gratings as described in the third section. Highly localized fiber Bragg gratings can be written with high NA optics. The last section describes the setup used for direct inscription of such FBG.

4.1 Ultra short pulse written fiber gratings

Common laser inscription of FBG is based on one-photon absorption processes using UV light. However, the energy gap of glasses is usually so large (3-6 eV, [Gat08]), that it has to be artificially lowered to enable absorption. This is done in a pre-treatment, by exposing the fiber glass of the core to Boron, Germanium or Hydrogen [Kas99]. The laser light hence only affects those photosensitive regions of the fiber. Thus, the properties of common continuous wave or long pulse written fiber gratings depend on the chemical composition of the fiber glass. The grating properties are thus not only determined by the intensity and duration of the illumination, but on how the fiber material has been treated before the inscription and how it is treated afterwards [Can08]. In general, the modifications of the fiber are classified, whether the material has not been

damaged (Type I) or if the incident light intensity has been above the damage threshold (Type II) [Can08]. Type I modifications can be attributed to defect center formation in the glass, which results in a homogeneous raise of the refractive index. Type II modification usually mean destruction of the glass matrix, resulting in a darkening and negative refractive index contribution. Most recently, very thermally robust gratings have been discovered, that form out of annealed Type I gratings after prolonged heating (Type R) [Can08, Ban08, Lin11a, Lin11b].

In contrast to that, ultra short pulse laser pulses provide enough intensity to enable non-linear absorption due to multi-photon or tunneling processes. Several studies [Ito06, Wil04, Dav96, Gat08] have identified three modification regimes in bulk fused silica, which depend on the incident energy density. For a Ti:Sapphire system that provides 800 nm pulses of 100 fs duration, the following intensity regimes have been identified [Ito06]:

- isotropic color-center / densification regime: $I > 2 \cdot 10^{13} \text{W/cm}^2$
- anisotropic birefringence / nanograting regime: $I > 8 \cdot 10^{13} \text{W/cm}^2$
- micro-void regime: $I > 30 \cdot 10^{13} \text{W/cm}^2$

The refractive index change of both the color-center and birefringence regime is of the order of $\Delta n \approx 10^{-3}$, the contrast of the micro-voids can be up to two orders of magnitude stronger. The mentioned threshold values are not absolute, but a mere orientation. They are given for one particular pulse width, focussing and pulse shape. The role of the latter and the dispersion of the pulses are still subject of research.

Note that within the isotropic regime, the refractive index raise increases monotonically with the number of pulses for repetition rates < 200 kHz [Eat08]. This dependence is more complex in the anisotropic regime, where an initial decrease of the refractive index can be annealed with subsequent pulses [Wik09]. A micro-void is caused by a single high intensity pulse [Gam07].

Illumination with ultrashort pulses often taps into several modification regimes at once, since the intensity of the laser beam is not homogeneous but decays gradually from the beam center. For low fluences, ultra short pulse fiber gratings can be regarded as Type I modification – with the distinction, that the multi photon absorption that

created these color-centers, does not require photosensitive material. Nevertheless, prior hydrogen loading can increase the grating strength [Mih08] as in the case of conventional UV laser inscription. Gratings written with higher fluences would be classified to be of Type II. This classification however can obscure many of the features of the ultra short pulse induced modifications, most prominently the sub periodicity in the nanometer regime [Kaz07]. micro-void gratings for example, have a more complex shape, combining both Type I and Type II modifications [Jov09, Gam06] as will be detailed in Sec. 6.1.

4.2 Focussing and feature size

In contrast to conventional photosensitive techniques, ultrafast fiber grating inscription heavily depends on the focussing conditions of the laser beam, because the nonlinear absorption processes require an intensity above certain thresholds (see Sec. 4.1). The intensity of the ultra short pulses at the core are affected by the parameters of the initial laser beam (beam waist, pulse duration and profile), the focussing objective or lens, the alignment of the optical components of the setup and the fiber, the curvature of the fiber and the inner fiber geometry (especially for micro-structured fibers). The resulting intensities can be computed beforehand, usually requiring heavy numerical calculations. The reason is that the dynamics of self-focussing and filamentation have to be taken into account, because their threshold intensities are of the same order of magnitude than the absorption thresholds [Mar75, Val07, Gam06, Mau10].

To some extend, Gaussian optics can be used for estimating the dimensions of the modification for high NA inscription optics. Using the well known expressions for the focussed Gaussian beam (e.g. [Sal91]), the dimensions of the focus (Rayleigh-range z_0' and beam waist radius W_0') can be estimated to be

$$W_0' \approx \frac{\lambda_0}{\pi \mathrm{NA}} \qquad \text{and} \qquad z_0' \approx n_2 \frac{\lambda_0}{\pi \mathrm{NA}^2}. \tag{4.1}$$

for focussing into a planar piece of fiber of refractive index n_2 with an oil immersion objective. E.g. for inscription with a laser emitting a $\lambda_0 = 800$ nm and an oil-immersion objective (NA $= 0.8$) the width and height of the focus are $2W_0' = 0.6$ μm and $2z_0 =$

1.2 μm. However, the inscribed structures are in most cases smaller than the focus, because of the nonlinear absorption as will be shown in Sec. 6.1, but they might also be larger due to aberrations.

The analytical expressions fail for focussing with lower NA (< 0.2) into free standing fibers because of two reasons: Firstly, the Rayleigh length is often as long as the fiber diameter itself and the effect of the fiber curvature cannot be neglected [Tho07]. Secondly, filamentation within the fiber occurs already in close proximity of the outer cladding surface [Val07]. In general, it could be observed that refractive index changes written with low NA optics are much longer as the Rayleigh length of the beam. Modifications ranging from 10 μm [Dür04, Ber07] to 50 μm [Mih08, Tho07, Wik04] in length could be observed. A FBG with a very large cross-section that covers almost half of the fiber can be inscribed by translating the fiber perpendicular to the beam [Gro04] as detailed in Sec. 4.3.

4.3 Phase mask scanning

Side illumination techniques dominate commercial fiber Bragg grating production. Similar to photographic exposition, the fiber core is illuminated with a periodic intensity pattern along its axis, which is provided by an interferometric setup. This assures excellent reproducibility and period stability [Kas99, Oth97]. For increasing the intensity, the laser beam is usually focussed with a cylindrical lens of low NA < 0.1, which is aligned parallel to the fiber axis (Fig. 4.1).

Because of the short coherence length (typically $l_{coh} \approx 30$ microns for 100 fs pulses) of the pulse, free beam interferometric setups with ultra short pulse lasers are non-trivial to align [Bec08, Bec09]. Therefore, the approach to place a phase mask in close proximity to the fiber seems to be more apt [Mil00, Mih04]. One problem of this approach is, that if the non-diffracted zeroth order is not suppressed, the interference pattern after the phase mask has an additional periodicity along the axis of propagation. This so-called Talbot effect is caused by three beam interference of the zeroth order with both first order diffracted beams [Mil00].
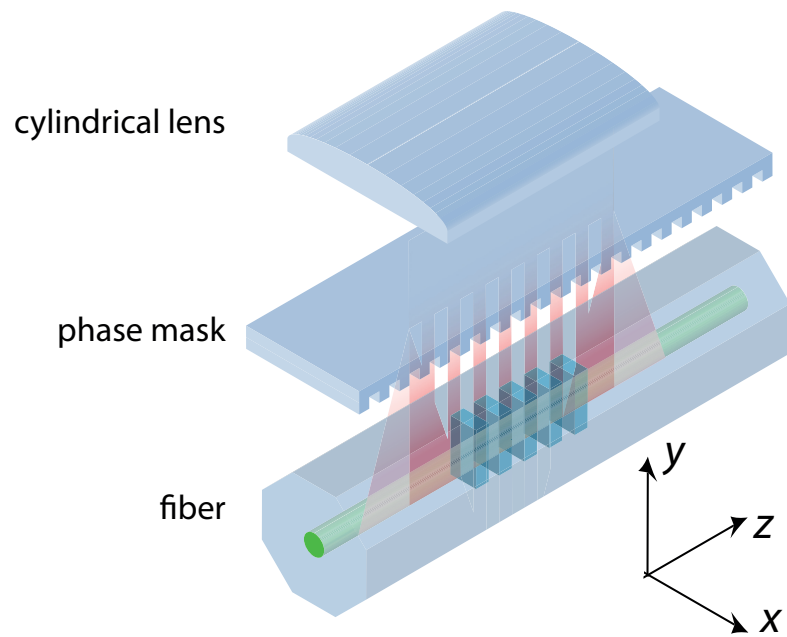
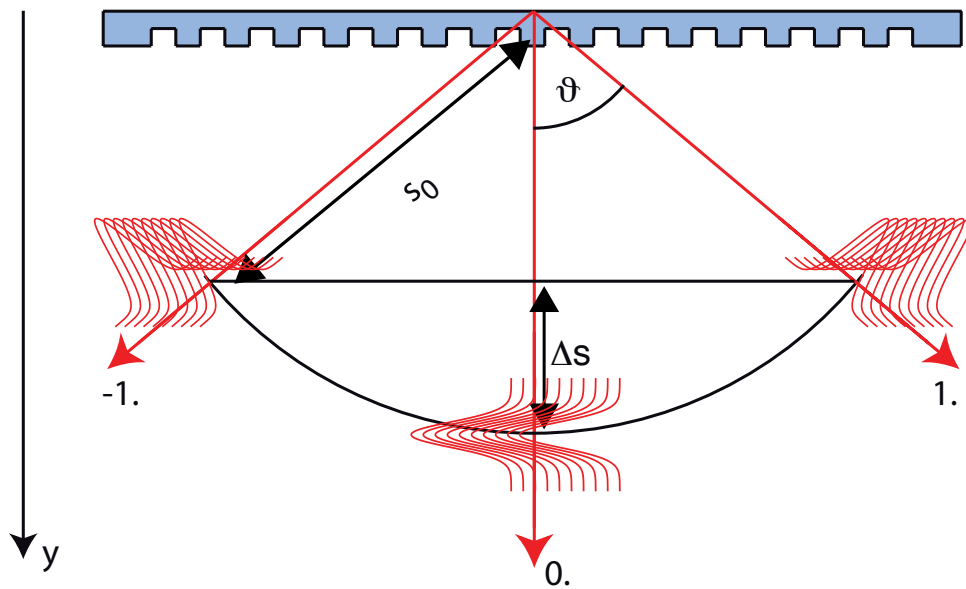**Fig. 4.1** Schematic of FBG inscription with a phase mask in close proximity.

Fig. 4.2 Principle of the ultra short pulse propagation after the phase mask.

Using an ultra short pulse laser actually solves this problem, because of the "order walk-off effect" due to its short spatial coherence length [Sme04]. Because the pulse fronts of the first diffraction orders leave the phase mask under a certain angle ϑ, they are spatially separated by $\Delta s = s_0(1 - \cos \vartheta)$ from the zeroth order for the distance of s_0 behind the phase mask (Fig. 4.2). By simply placing the fiber far enough ($\Delta s > l_{\mathrm{coh}}$) from the phase mask, the trails of pulse fronts do no longer overlap and a pure two beam interference pattern can be obtained at the fiber core [Tho07].

This approach was used and adapted for the inscription of large cross-section FBG based on a commercial ultrashort pulse laser system (Clark MRX Inc. CPA2110) as ultra short pulse source. The laser system delivers pulses of 150 fs at a repetition rate of 1.0 kHz at 775 nm. The maximum pulse energy is 1 mJ, the $1/e^2$ beam width 5.6 mm. The stage for phase mask inscription (Fig. 4.3) is designed for inscription with maximal reproducibility in a free-standing fiber. The beam of the laser can be attenuated with a polarizer and a rotating half wave plate. It is then routed with mirrors to the translation stage, where it is focussed with a cylindrical lens (focal length $f = 20$ mm). Firstly the fiber is placed at the groove, where it is held by reduced air pressure (Fig. 4.4 (b)). Secondly, it is fixed by two fiber clamps, which are mounted on micro-blocks. With these blocks, the fiber is pulled, so it is under a defined tension (typically 0.3 N), measured with an in-build dynamometer. Hence, the phase mask is placed on top of the fiber, so that the distance between fiber and phase mask is 2.5 mm. This assures, that the fiber is exposed to a pure two beam interference pattern due to the order walk off.

The fiber holder block includes a mirror and a diffusion screen in order to image the diffraction orders of the phase mask behind the fiber (Fig. 4.4 (a)). This allows for accurate positioning of the fiber with respect to the beam. Even a small displacement greatly affects the diffracted light pattern (Fig. 4.4 (c)). For example, if the light does not hit the center of the fiber, the beam gets refracted and the diffraction orders will be at different locations. The same holds true for a misaligned phase mask or cylindrical focussing lens.

The setup allows for static inscription as well as for translating the fiber holder block during illumination. The latter allows for extended stitch-free grating structures, since the position of the phase mask is fixed with respect to the fiber. This assures a constant
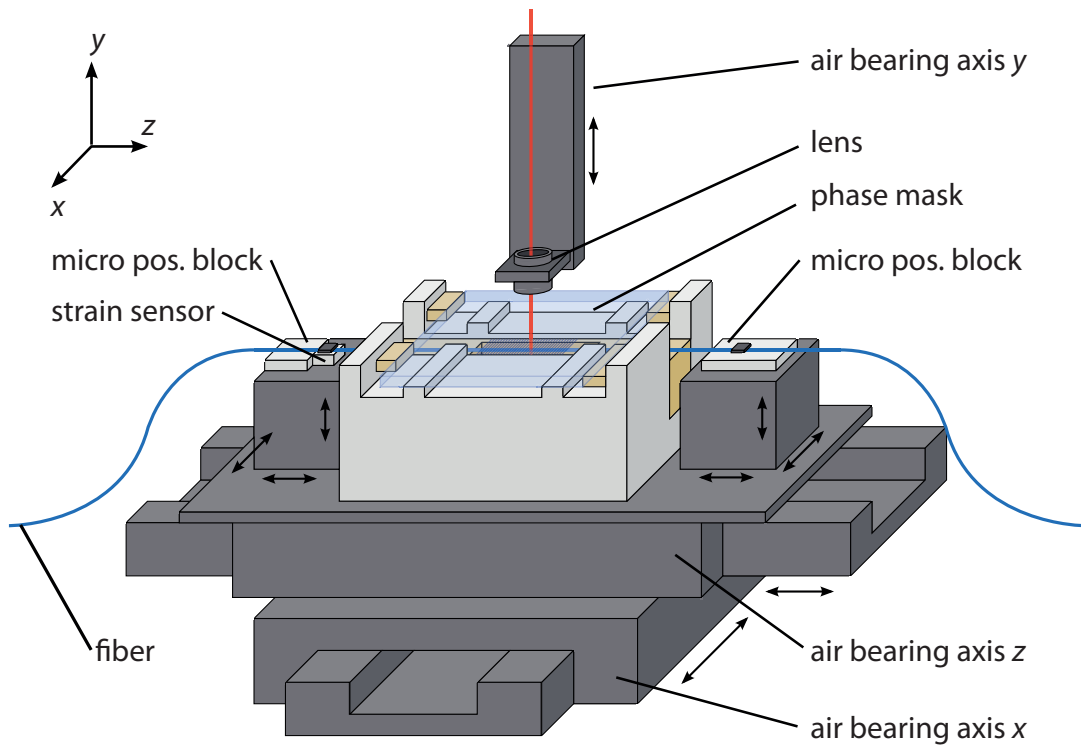
Fig. 4.3 Schematic of the inscription stage. The whole block with fiber and phase mask is moved with respect to the laser beam incident from above.
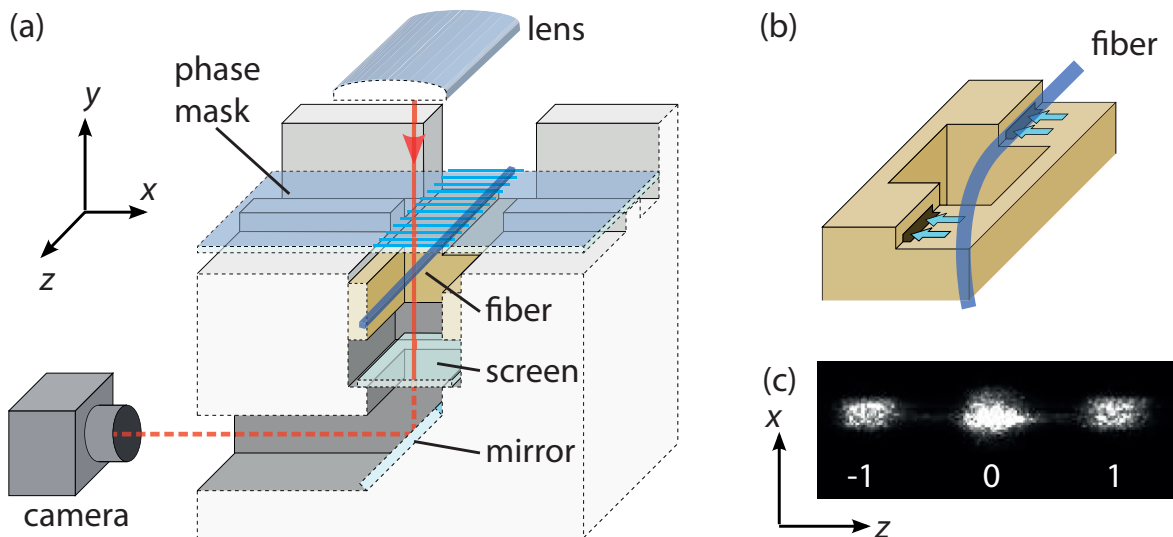

Fig. 4.4 Cut-away of the fiber and phase mask holder of the inscription stage (Fig. 4.3), revealing fiber, screen, mirror and camera (a); close up of the suction fiber holder (b); diffraction pattern of the inscription laser beam after phase mask and fiber (c).

position of the intensity pattern along the fiber core during translation. In the following, translating the stage along the fiber is referred to as z-scanning, while scanning perpendicular to the fiber axis and perpendicular to the optical axis of the inscription optics is referred as x-scan. Translating the inscription optic itself with respect to the fiber holder block is y-scanning.

4.4 Direct writing

Direct writing techniques have initially been based on excimer-lasers [Hil90] for realizing long period gratings. With focussed near-infrared ultra short pulses, modifications of less than one micron can be achieved, thus enabling the direct inscription of short period FBG, too. The ultra short pulse laser is usually focussed with a high NA (> 0.4) objective in order to achieve the small feature size (Fig. 4.5). The center piece of a direct write setup is the translation stage, where the fiber is mounted upon. The fiber core is illuminated for a certain time and hence the stage moves for the desired period Λ. This procedure is repeated for realizing fiber gratings of arbitrary length.

However, since this approach depends on the relative positioning precision of the translation stage, position variances directly result in variances of the grating period $\Delta\Lambda$. This deteriorates the efficiency of the FBG by increasing its band width [Erd97b]. With the translation accuracy provided by a modern air bearing stage (< 100 nm), point by point written FBG with period of $\Lambda = 2.1$ µm could be achieved [Wik04]. A way to minimize $\Delta\Lambda$, is to move the fiber with a constant velocity v and modulate the laser output with the frequency f, e.g. with a shutter. The resulting period of the grating is then $\Lambda = v/f$. If one realizes a modification with a single pulse of the laser, the repetition rate of the laser itself can serve as the modulation frequency [Mar10].
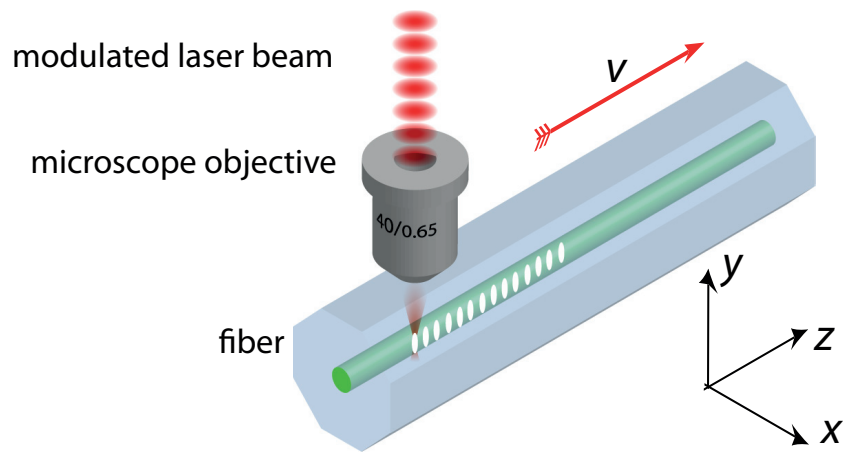
Fig. 4.5 Direct writing of FBG by translating the fiber under a microscope objective with high NA.

This approach is implemented in the setup shown in Fig. 4.6. This setup has been realized at the Macquarie University [Mar10] and has been used for the inscription of the highly localized FBG investigated for this thesis. The inscription laser is a commercial CPA-System (Spectra-Physics, Hurricane), which delivers 110 fs short pulses at 800 nm with a repetition rate of $f_R = 1$ kHz. Pulse energies of 200-500 μJ were used in order to achieve micro-void modifications. The photograph (Fig. 4.6) shows the part of the setup, where the beam is focused and the FBG is inscribed. For realizing a very small spot, a 20x oil immersion objective (NA=0.8) was used. The fiber mount itself is a glass ferule with a diameter that matches the fiber diameter (≈ 125 μm) and is flatly polished along one side. The fiber itself is uncoated completely, before it is threaded through the micro ferule and fixed on an air bearing stage (Aerotech ABL3000) using a fiber clamp. Index matching immersion oil is used in between writing objective and ferule as well as for threading the fiber through the ferule in order to avoid big index jumps. Hence, ferule and objective are aligned with respect to each other with the help of a piezo-assisted micro-block, so that the focus of the objective coincides with the center of the fiber. This alignment is supported by the imaging system, which consists of a telescope and a camera, sitting behind a dichroic mirror (HR for 800 nm, transparent for VIS). This way the micro structuring can be directly imaged through the processing objective.
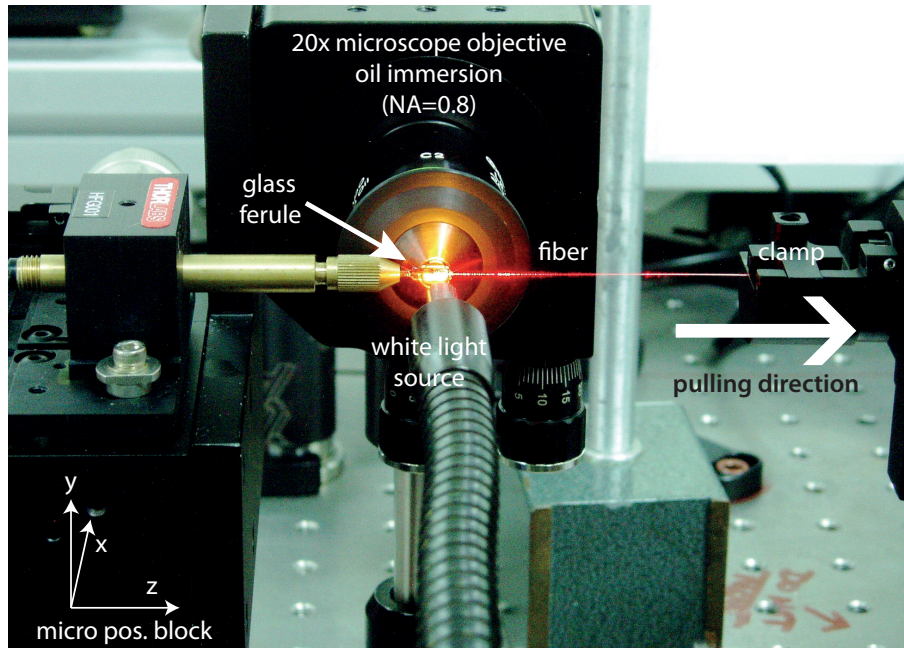
Fig. 4.6 Photograph of the part of the setup, where the incription laser beam and fiber are aligned. Red light of a Helium-Neon-laser has been coupled into the fiber in order to highlight the fiber.

For inscription, the fiber is pulled while the ultra short pulses are incident. This way, periodic chains of micro-voids are written inside the fiber core. Typical FBG realized by this setup have a period Λ of 1.06 μm and reflect light at 1.5 μm in the second order. While the accuracy perpendicular to the fiber axis (Δx and $\Delta y \approx 0.3$ μm) is limited by the micro block and the play the fiber has inside the ferule, the longitudinal accuracy Δz is several orders better, due to the smooth movement of the air-bearing stage and the clock-work precision of the lasers repetition rate [Mar10].

5 Large cross-section fiber Bragg gratings in single and few mode fibers

The aim of this chapter is to investigate properties and possibilities of large cross-section fiber Bragg gratings. *Large cross-section* means fiber gratings, that cover more than the cross section of the core. They are especially interesting for high-power all fiber lasers, because the fibers employed here have a large cross-section in order to avoid non-linear effects. In the first section comprises the design and fabrication parameters of the large cross-section FBG and the anticipated resonances. Both large cross-section FBG with partly and fully modified cross-sections can be realized with low NA optics and the phase mask scanning technique. Their spectral and spatial properties are explored for the single- and few mode regime in the second and third section. FBG that are good mode converters are demonstrated as well as FBG that suppress mode conversion entirely.

5.1 Fiber grating design

Stability and beam quality are the reasons, why most fiber lasers aim for single mode operation. Although single mode operation is also possible in multi mode fibers [Fer98], single mode fibers are more apt for robust setups. Thus it is common to use fibers with a V-parameter < 2.4 (Eq. 2.23) for the lasing wavelength. However, to facilitate power scaling by avoiding non-linear effects, the cross-section of the fiber core has to be as

large as possible. For step-index fibers, these goals require the contrast between core and cladding refractive index has to be as small as possible. For example, a fiber laser that emits 1060 nm and has a fiber core with 20 µm diameter requires an index contrast of $n_1 - n_2 < 5 \cdot 10^{-4}$. Such low contrasts are very difficult to achieve, especially in glasses where the concentration of several dopants has to be balanced. This is the reason why most active step-index fibers with large cross sections cannot be fabricated to be truly single mode but usually support few modes.

While FBG inscription in such low index contrast active LMA fiber is demonstrated in Sec. 7.1, the aim of this chapter is to characterize the fundamental properties of large cross section FBG for the single mode and the few mode regime. Throughout this chapter, a standard step index single mode fiber for telecommunication is used (j-fiber IG-09/125/245). The core has a diameter of $2a_1 = 9$ µm, the cladding is of $2a_2 = 125$ µm. The fiber has a numerical aperture of $\text{NA} = \sqrt{n_1^2 - n_2^2} = 0.12$. This fiber is truly single mode for the telecommunication wavelength of $\lambda = 1.5$ µm. At $\lambda = 1.0$ µm, it also supports the $\text{LP}_{1,1}$ mode.

For the following investigations, gratings with a period of $\Lambda = 1.075$ µm were inscribed into the fiber. The second order resonant wavelength of these gratings lies in the single mode regime of the fiber at 1555 nm, while the third order resonances are in the two mode regime at 1040 nm (Tab. 5.1). In this chapter, all resonances are identified with linearly polarized pseudo modes, since for low V, even and odd $\text{HE}_{2,1}$ modes cannot be spectrally resolved from the $\text{TE}_{0,1}$ and $\text{TM}_{0,1}$ modes and can thus be treated as degenerate [Sny83].

Using the effective refractive indices $\bar{n} = \beta(\lambda/2\pi)$ the FBG phase relation (Eq. 2.36) can be rewritten for the resonant wavelength as

$$\lambda_{\mu\nu} = (\bar{n}_\mu + \bar{n}_\nu)\frac{\Lambda}{m}, \qquad (5.1)$$

where Λ is the actual period of the FBG and the integer m denotes the Fourier component (Eq. 2.25) which is used. Note that in the two mode regime, three resonance peaks are predicted: two self-coupling resonances with $\mu = \nu$ and one mode-converting peak which sits right in between the self-coupling resonances (see also Sec. 2.4).

m	λ_{Bragg}	V	LP modes
2	1555 nm	2.0	$LP_{0,1}$
3	1037 nm	3.1	$LP_{0,1}$, $LP_{1,1}$

Tab. 5.1 Fourier order, reflection wavelength of the fundamental mode and supported scalar modes in that wavelenth range for the investigated FBG ($\Lambda = 1.075$ µm , $\bar{n} = 1.447$)

5.2 Single mode fiber Bragg gratings

Since the core of the single mode fiber allows only for one mode to propagate, the setup for characterizing is straight forward: light of a super luminescence diode (B&W Tex BWC SLD, emitting 1.4-1.6 µm) is directly butt-coupled via a single mode transportation fiber to the fiber piece that incorporates the FBG. The transmitted light is spectrally analyzed (Yokogawa AQ6375, detecting 1.2-2.4 µm with a resolution of 0.05 nm). The transmitted signal decreases at each resonant wavelength, where the light of the fundamental mode is coupled to other modes (in that case, the backward travelling fundamental or cladding and radiation modes). Since the spectrum can be directly measured at the inscription setup before and after inscription, the spectrum can be normalized, exposing eventual broadband losses.

Fig. 5.1 displays the spectrum of a FBG, where only a part of the cross-section of the fiber is modified (see inset of Fig. 5.1). Here, the fiber has been translated along its axis (z-scan) during inscription, yielding a 40 mm long grating of approximately 2-3 µm width and 40 micron height (set by the low NA focussing optics [Tho07]). The distance between fiber and phase mask was $\Delta y = 1.25$ mm. Inscription energy was 400 µJ while $v_z = 6$ mm/min. A microscope image of the fiber cross-section is shown in the inset of Fig. 5.1. The major resonance at the highest wavelength at 1555 nm is the self coupling resonance of the fundamental mode. Multiple resonances can be observed below 1554 nm, which result from mode conversion to cladding guided modes. Their onset wavelength is determined by the refractive index of the cladding n_2, since their effective refractive index $\bar{n}_\nu < n_2$ (Eq. 5.1). When exposed to air, the cladding support several thousands of modes since $V \approx 275$ (Eq. 2.23). A detailed analysis of this conversion to high order mode coupling is the subject of chapter 6.
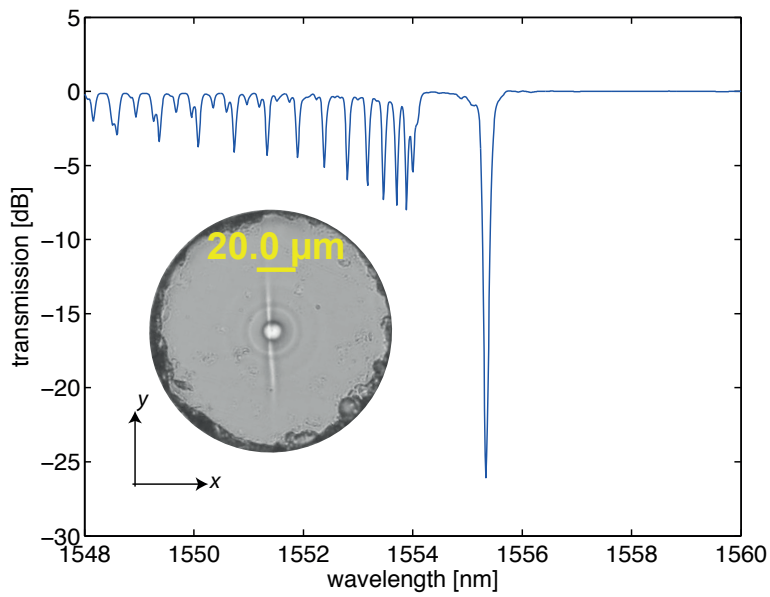
Fig. 5.1 Transmission spectrum of a FBG that only partly fills the core. Strong coupling to cladding modes can be observed to the short wavelength side of the fundamental Bragg peak.
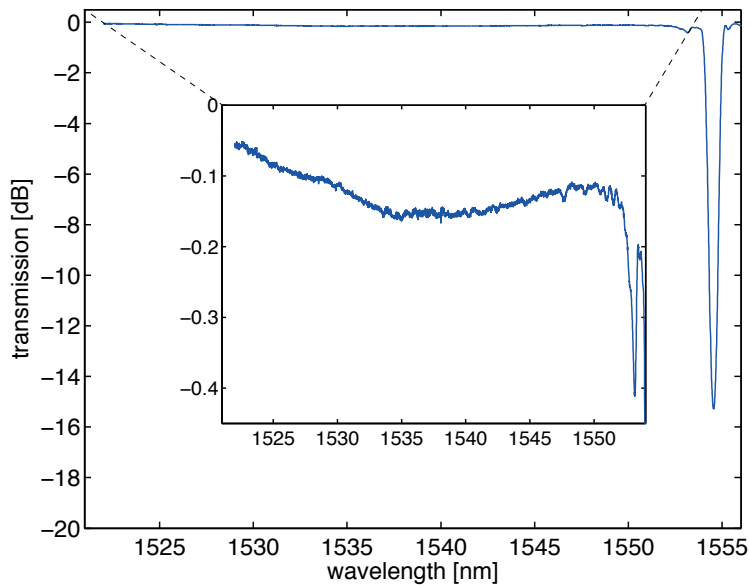

Fig. 5.2 A femtosecond pulse written FBG that homogeneously covers the core and its surroundings exhibits no cladding mode coupling. The transmission spectrum has been scaled in the inset to highlight the lack of resonances to the shorter wavelength side as well as the exceptionally low insertion losses.

In contrast, Fig. 5.2 shows a spectrum of a FBG that covers the whole cross-section of the fiber. It has been inscribed by symmetrically translating the fiber by $d_x = 40$ µm with $v_x = 0.1$ mm/min, so that the grating completely covers the fiber core and its surrounding. The spectrum exhibits only a single resonance, which is the self-coupling peak of the core guided fundamental mode. Although the cladding was exposed to air, no cladding resonances at all can be observed. The insertion losses are below 0.2 dB over the whole measurement range. Only at a small notch next to the fundamental Bragg resonance at 1555 nm, losses of 0.4 dB occur. This exceptionally good suppression of mode conversion reproduces the results achieved by [Gro04]. As detailed in Sec. 3.5, this complete suppression of all mode converting resonances means that the transversal refractive index profile complies with Eq. 3.11: A fiber integrated filter that mimics the orthogonality relation of the modes (Eq. 2.5) has been inscribed.

5.3 Gratings in few mode fibers

5.3.1 Probing

Probing a FBG in the multi mode regime requires a more sophisticated setup. One reason is the possibility to excite several modes. A transmission spectrum is hence no longer unambiguous, since the contributions of the higher oder mode remains unknown. Since these contributions travel the fiber with a slight phase change they result in a periodic beating of the transmission signal. This beating can be used to indirectly determine the modal contributions [Nic08] in combination with imaging the modal content.

In the following a more straight forward approach is applied, which aims for a clean excitation of solely one mode. This approach relies on a spatial light modulator (SLM) supported setup (Fig. 5.3). The collimated light beam is directed on a reflecting SLM (SXGA-R2/CRL OPTO, 1280×1024 pixels, ferroelectric liquid crystal) that is glued onto a silver mirror. On this SLM, a binary phase only grating is generated. The first diffraction order of this grating is used to control the beam position and shape. The beam is then coupled into the fiber using a standard lens ($f = 75$ mm).
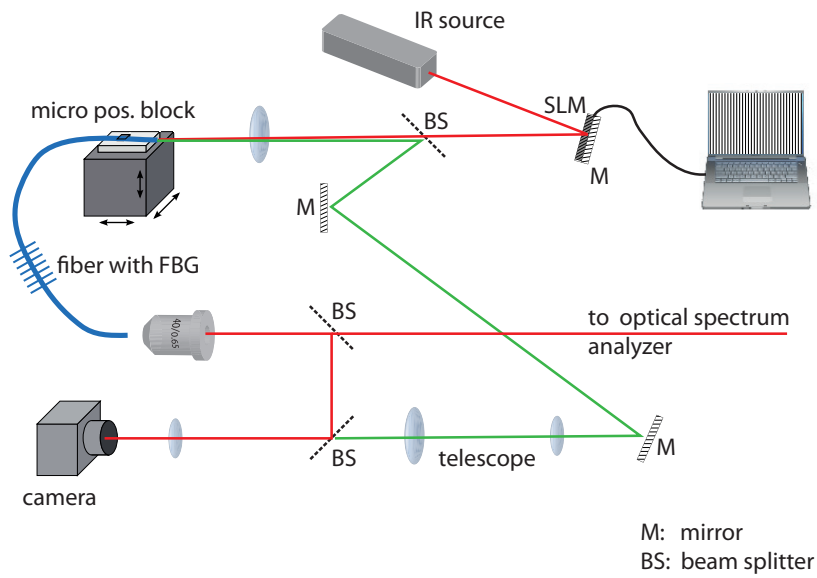
Fig. 5.3 Setup for probing few mode fibers using a spatial light modulator (SLM) for shaping the input beam. Both reflected and transmitted light are imaged onto the same camera for comparison.
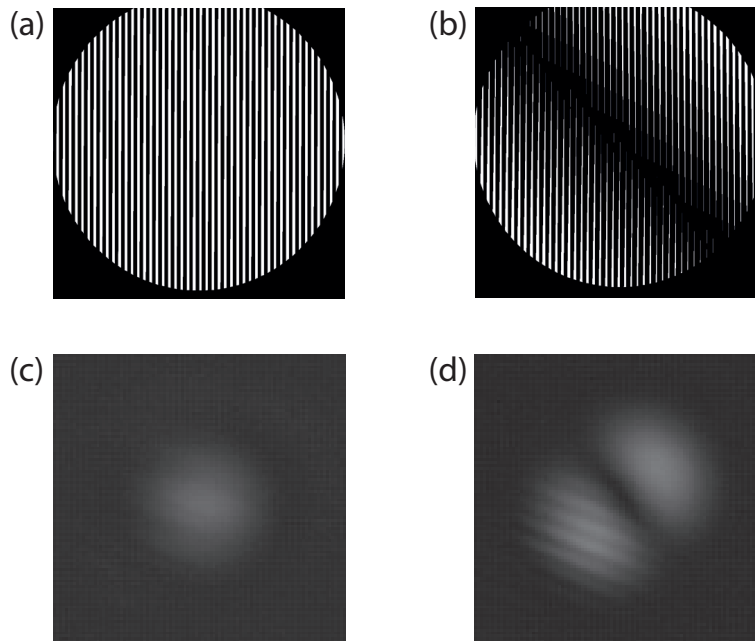

Fig. 5.4 Binary grating on the SLM (a,b) and resulting intensity distribution that has been excited in the fiber (c,d).

The SLM is directly addressed by the graphics processing unit of the computer, which allows real time manipulation of the diffracted beam [Gra09]. Typical patterns of the SLM are shown in Fig. 5.4 (a,b). With the period and angle of the binary grating, the spatial position of the first order diffracted beam on the fiber end facet can be precisely controlled. The wavefront curvature of the beam can be controlled as well, allowing for longitudinally shifting the focus and correcting for aberrations [Nei02]. The beam can also be modulated with more complex pattern. For example, the binary pattern in Fig. 5.4(b) results in a Hermite-Gaussian beam [Sal91].

This precise control of the light pattern incident on one fiber end facet allows for excitation of single fiber modes. The patterns in Fig. 5.4 (c,d) have been imaged at the other end of the fiber: By centering the incident Gaussian beam exactly at the fiber axis and optimizing both radius and wavefront curvature, it can be achieved that almost all of the light couples to the fundamental fiber mode (Fig. 5.4 (c)). These parameters can then serve as a reference point to realize more elaborate pattern in order to excite higher order modes: Fig. 5.4 (d) displays a successful excitation of solely the $LP_{1,1}$ mode. Thus, after an initial alignment via the computer controlled SLM, the setup offers the ability to switch between different mode excitations. In contrast to classic means [Sni61b], no mechanical parts of the setup have to re-aligned for different fiber mode excitations, which greatly improves reproducibility.

Using beam splitters, the setup (Fig. 5.3) allows to image transmitted and reflected mode pattern as well as to record the corresponding transmission spectrum. Two infrared (IR) light sources were used: A self-build fiber broadband ASE-source (emitting from 1000 nm to 1100 nm with 5 mW output power) for recording the spectra and a commercial tunable single frequency laser (Toptica, 980-1075 nm, 20 mW output power) for mode excitation. Since both sources use similar delivery fibers, they can be exchanged without altering the coupling. All spectra were recorded using the ASE source, while the tunable laser was used for optimizing the coupling and imaging the modes.

5.3.2 Mode conversion

Fig. 5.5 displays the spectra of the FBG with the partially modified cross-section discussed in the previous section (Fig. 5.1), only probed at 1040 nm instead of 1555 nm. For clarity, the cladding mode resonances have been suppressed. The spectra were recorded for the fundamental $LP_{0,1}$ mode (solid line) and the $LP_{1,1}$ mode (dotted line) being incident. The incident intensity patterns are shown as insets. Three major resonances (a),(b), and (c) can be identified. Resonance (a) is only visible, if the $LP_{1,1}$ mode in the fiber is excited, while resonance (c) only appears for excitation of the fundamental mode. The resonance (b) can be observed for both incident modes and sits right in between (a) and (c).
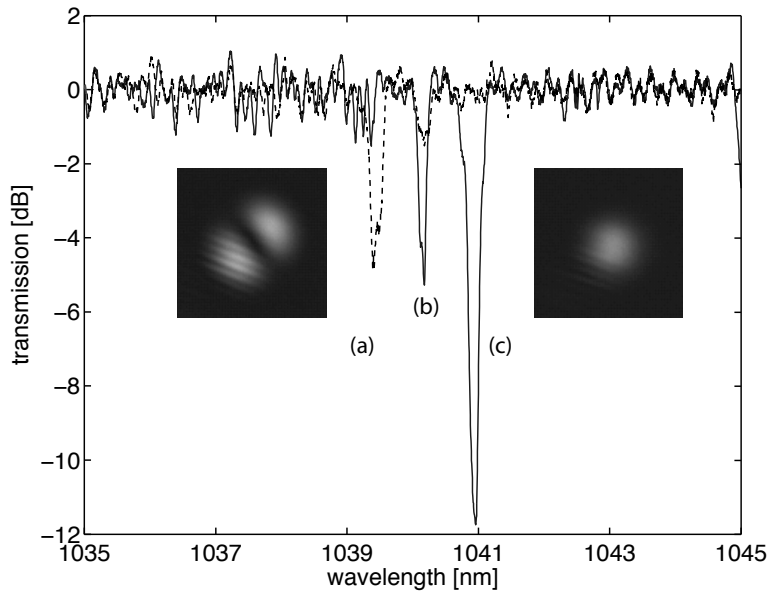

Fig. 5.5 Transmission spectra of a mode converting FBG in a few mode fiber. The insets display the modal content the fiber has been exited with (each of the patterns has been recorded off resonance). While the resonances (a) and (c) only appear for one of the mode excitations, resonance (b) is always visible.

The images of transmitted (T) and reflected modes (R) at each resonance are shown in Fig. 5.6. In the first column, the wavelength of the setup has been tuned off the resonances. Note that the Fresnel reflection of each pattern cannot be avoided and is visible as slight background. At resonance (a), all light in the fundamental $LP_{0,1}$ mode

is transmitted. Only light travelling as $LP_{1,1}$ mode is reflected. Similarly, the higher order mode is not affected by the grating at resonance (c) and only the $LP_{0,1}$ mode is reflected. Thus, these resonances can be identified as *self-coupling*. Resonance (b) is *mode converting*: $LP_{0,1}$ is reflected into the $LP_{1,1}$ mode, while $LP_{1,1}$ converts into $LP_{0,1}$.
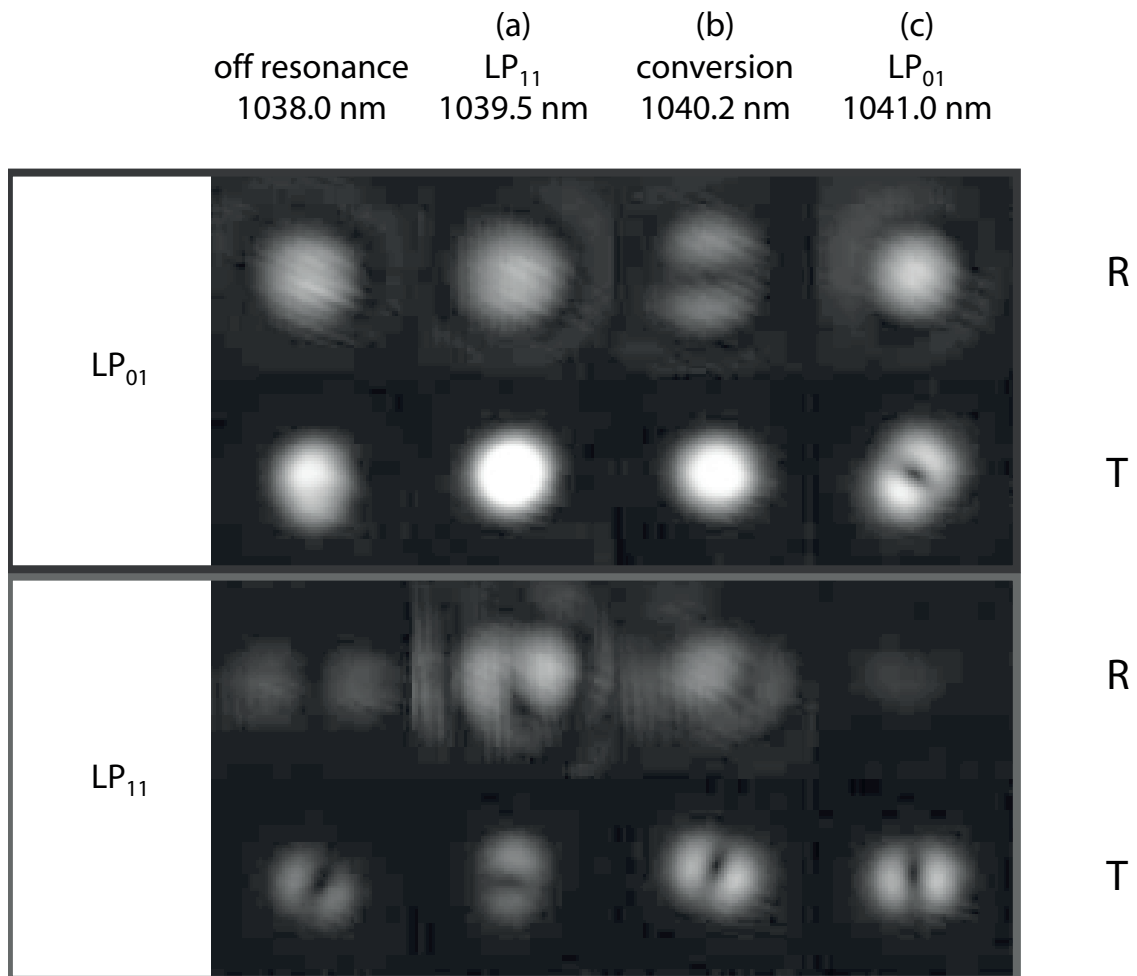

Fig. 5.6 Imaged mode patterns, which are reflected (R, every odd row) or transmitted (T, every even row) by the transversally inhomogeneous FBG. The first column displays the patterns off resonance, while the patterns of columns (a,b,c) were recorded at the peaks displayed in Fig. 5.5.

5.3.3 Mode conversion suppression

A large cross-section FBG with a transversally homogeneous cross section can suppress all cladding mode resonances as demonstrated in Sec. 5.2 for the single mode regime. This result implies an exceptional feature: coupling should only be possible if incident and reflected modes are equal. The remaining question is, if this suppression of *mode-converting* resonances also holds for wavelength regimes, where several core modes are supported. Indeed, when probed in the two mode regime, the grating of Fig. 5.1 only displays a single resonance when excited with a single mode (Fig. 5.7): if the light coupled in the fiber excites only the $LP_{0,1}$ mode, one resonance can be observed at 1041.3 nm (solid line). Probing with $LP_{1,1}$ light results in a single resonance at 1039.5 nm (dotted line). A mode converting peak like resonance (b) in Fig. 5.5 cannot be observed. This perfect suppression is of special interest for fiber laser cavities and will be applied in Sec. 7.1.
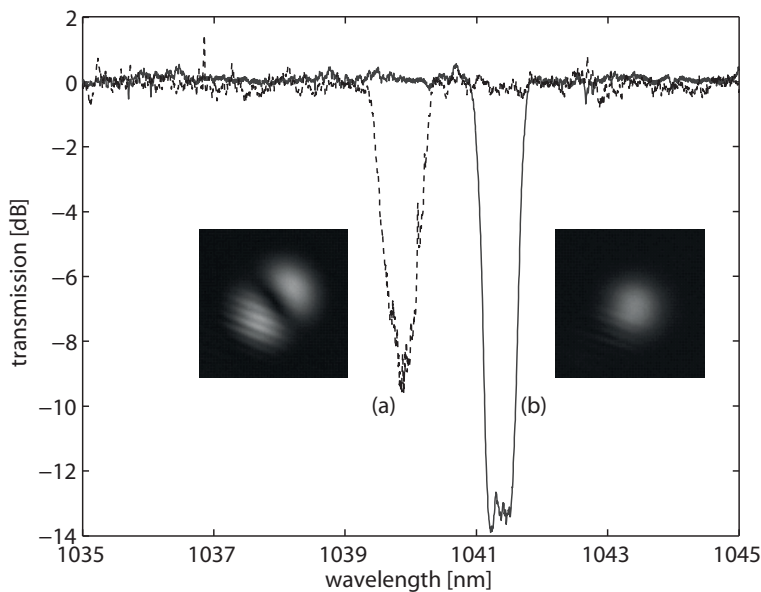

Fig. 5.7 Spectra for the large cross-section FBG with transversally homogeneous cross section, when operated in the few mode regime of the fiber. The spectrum plotted with a solid line displays the spectrum for almost pure $LP_{0,1}$ excitation, while the dotted line spectrum has been obtained by launching predominately $LP_{1,1}$ light.

6 Cladding mode coupling in highly localized fiber Bragg gratings

In the previous chapter, the possibilities of femtosecond pulse written fiber Bragg gratings to either suppress or support mode conversion in a few mode fiber were demonstrated. The remaining question is now, whether the additional flexibility to modify parts of the core allows for mode conversions that were not possible before with classic approaches like tilted fiber gratings [Erd96]. To which azimuthal mode classes can a femtosecond fiber grating enable coupling? This question can be systematically investigated in a highly multi mode fiber. However, the more modes a fiber supports, the more difficult it becomes to experimentally quantify how much power is carried in each mode [Kai09, Sha05].

This is the reason, why the coupling to cladding modes in a single mode fiber is better suited for experimentally demonstrating higher order mode coupling properties. The premise for this approach is the similarity of the coupling properties of core and cladding modes as detailed in Sec. 3.4. In the following, a single mode fiber for telecommunication wavelength (Corning SMF-28e) is used as a 'guinea pig'. Its properties and those of the inscribed FBG are summarized in Tab. 6.1. In this fiber, at $\lambda = 1.5$ µm the core supports only the fundamental mode, while all higher order modes are cladding modes. In order to achieve the strongest possible coupling to higher modes, the inscribed modifications have to possess two properties: on one hand, they have to be small compared to the core, so that higher azimuthal modes, which oscillate with higher spatial frequency do not cancel out. On the other hand, the modifications have to be of strong contrast, in order to provide significant coupling constants despite their small cross section. Such modifications are best inscribed with high NA optics. Therefore, the point by point

Radius	Refractive index
$a_1 = 4.15\ \mu m$	$n_1 = 1.4670$
$a_2 = 62.5\ \mu m$	$n_2 = 1.4618$
	$n_3 = 1.0$
$L = 20\ mm$	$\Lambda = 1.062\ \mu m$

Tab. 6.1 Fiber geometry (Corning SMF-28e) and grating properties.

method was chosen for inscription. The fiber Bragg gratings discussed in the following have a period Λ of 1.062 μm and have a length L of 20 mm.

The first part of this chapter reviews the details the micro-void modifications in order to establish a simplified model of the cross-section of the highly localized FBG. Hence, the abilities of these highly localized fiber Bragg gratings to enable coupling of the core mode to cladding modes of higher azimuthal order are explored. The modes of a fiber with a higher azimuthal mode are in most cases degenerate with modes of lower azimuthal order. However, it will be shown, that the number of degenerate modes to be considered at a resonance can be limited. The chapter closes with a detailed study of the multiple cladding mode coupling of a highly localized fiber Bragg grating.

6.1 Highly localized FBG

Fig. 6.1 shows microscope images from the top (a) and side (b) of the micro-void fiber Bragg gratings, which have been taken with the imaging system of the inscription setup (Sec. 4.4). The center of the modification appears dark and corresponds to a refractive index decrease, a Type II modification (Sec. 4.1). This modification is approximately 0.4 μm in width and 1.9 μm in height. In the following it is referred to as *micro-void* in accordance with studies in bulk glasses [Gam06]. The void is surrounded by a shell of increased refractive index, which is approximately 1.0 μm wide and 8 μm long. This shell is a Type I modification, which can be healed out, if the fiber is exposed to temperatures above 300 °C [Mih08].
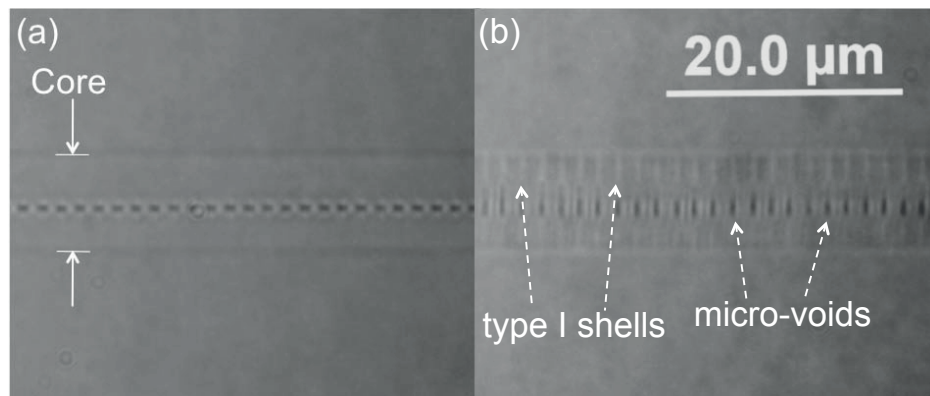
Fig. 6.1 The point by point written highly localized FBG viewed from the top (a) and side (b) by the build-in imaging system of the setup.
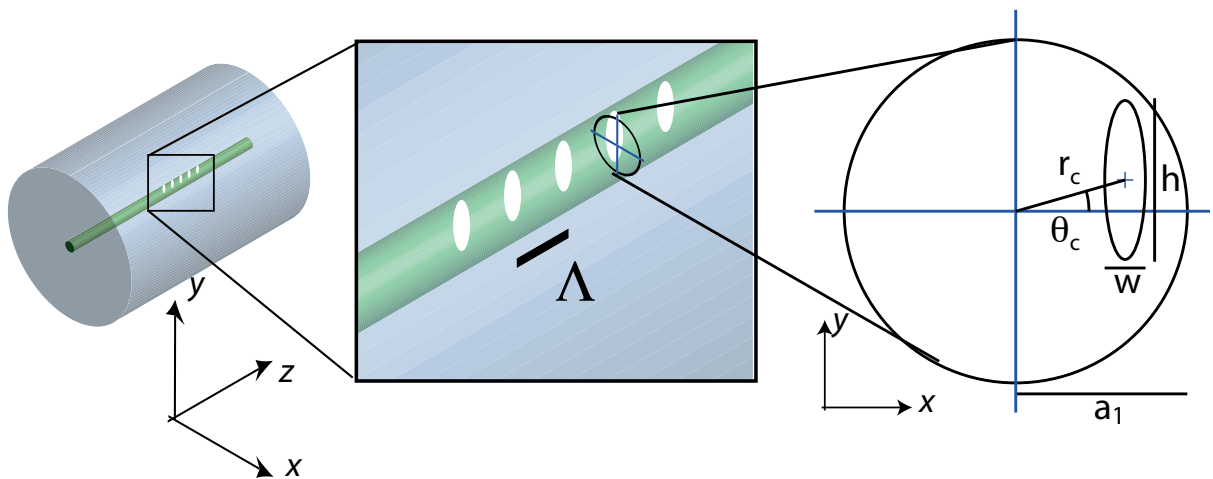

Fig. 6.2 Schematic of the micro-void and of the simplified transversal geometry, used to model its coupling behavior.

In the following, the densification is neglected and the birefringence and difference in grating strength are evaluated for the void only in order to simplify the calculation. This approximation is reasonable since the magnitude of the index change of the void is at least one order of magnitude greater than that of its shell [Jov09].

Transversally, the micro-void is modelled as an ellipse with the width w and height h of the refractive index decrease. The displacement of the center of the modification from the center of the fiber core is measured in ϕ_c and r_c, as shown in Fig. 6.2. Because of the steep edges of the void [Gam06], the longitudinal refractive index profile is in good approximation rectangular with the width w and the maximum refractive index change $\Delta n_{\mathrm{max}} = n_1 - n_{\mathrm{void}} \approx 0.45$. As in [Jov09], the refractive index of the void is assumed to be ≈ 1. The point by point written micro-void gratings typically have a period of $\Lambda = 1.07$ µm and reflect in second order within the telecommunication range ($\lambda \approx 1.5$ µm) (Eq. 2.36). For the second order Fourier resonances , the corresponding refractive index components can be evaluated using Eq. 2.28 to be

$$\Delta n_2(r, \phi) = \frac{\Delta n_{\mathrm{max}}}{\pi} \sin\left(\frac{2\pi w}{\Lambda}\right) \Theta(r - r_c, \phi - \phi_c) \approx 0.1 \cdot \Theta(r - r_c, \phi - \phi_c), \quad (6.1)$$

with $\Theta(r, \phi) = 1$ inside the ellipse and zero elsewhere. This homogeneity can be assumed without loss of generality: For an inhomogeneous void, the bary-center would have to be shifted by a small amount and the dimensions of the void would also be smaller.

6.2 Coupling properties

Clearly, the micro-void is a very good example of a highly localized modification inside of the fiber core. Firstly, it is much smaller than the typical fiber core (diameter of the order of 10 µm). Secondly, it provides a high index contrast.

In the case of a highly localized FBG as provided by a micro-void gratings (Sec. 6.1), the coupling strength is rather determined by the radial position of the FBG within the fiber than its shape. This becomes clear, when the overlap integrals of the cladding modes (Eq. 2.30) are evaluated for the perturbation $\Delta\epsilon$ introduced by the micro-void (Eq. 6.1). The coupling constants of the first six hybrid modes are plotted in Fig. 6.3 (a). The center

of the micro-void is located at the x-axis of the fiber cross-section (Fig. 6.2), with $\phi_c = 0$ and the radial position r_c being varied from 0 to the fiber diameter $a_1 = 4.5\,\mu m$. Placing the center of the micro-void exactly at the x-axis causes all coupling coefficient to odd hybrid modes to be zero. A different azimuthal position with respect to the incident polarization (which is set by assuming that only the even $HE_{1,1}$ mode is incident) causes coupling into the odd hybrid modes but has no significant polarization effect.

Coupling to the $l = 1$ hybrid modes is at its maximum, if the micro-void is centered. For all higher modes, coupling becomes only significant for an off-center micro-void. As a rule of thumb, the higher the azimuthal index l of the mode is, the more the micro-void has to be placed apart from the center.

In Sec. 3.4, virtual cut-offs have been introduced as transition points, where the core fields of the cladding modes significantely changes. These cut-offs are drawn as horizontal white dashed lines in Fig. 6.3. The $U_{l,1'}$ cut-offs marks, where the cladding modes start to have a field within the core. This is also reflected in the coupling constants: The higher the azimuthal index l is, the higher the radial order of the first mode of that class, that can efficiently couple with the core mode. The $U_{l,2'}$ cut-off marks a significant change in the coupling behavior since beyond this cut-off, the coupling strength is highly selective: strong for HE modes and negligible for EH modes. Only for higher radial index m does coupling to EH mode become comparable to HE modes.

Fig. 6.3 (b) shows the corresponding transmission spectra for increasing radial micro-void position. For each set of coupling constants κ_{lm}, the transmission spectrum $T = |A_{11}(z = L/2|)$ has been computed by solving the coupled mode equations (Eq. 2.31) with the boundary conditions $A_{11}(z = -L/2) = 1$ and $B_{lm}(z = L/2) = 0$ set by the length L of the FBG [Erd97b]. Because the core mode $HE_{1,1}$ carries less light towards the core-cladding boundary, the overall strength of the resonances decreases with increasing decenter r_c. There are two combs of cladding modes, the odd l comb, that is purely $l = 1$ for a perfectly centered micro-void grating and the even l comb, that arises for decentered gratings. In the following section, it will be shown that even and odd resonance combs are caused by coupling to degenerate $l = 0, 2, 4 \ldots$ and $l = 1, 3, 5 \ldots$ modes. Despite this degeneracy, not all l mode classes have to be considered for the correct computation of a spectrum. Depending on the highest m in the region
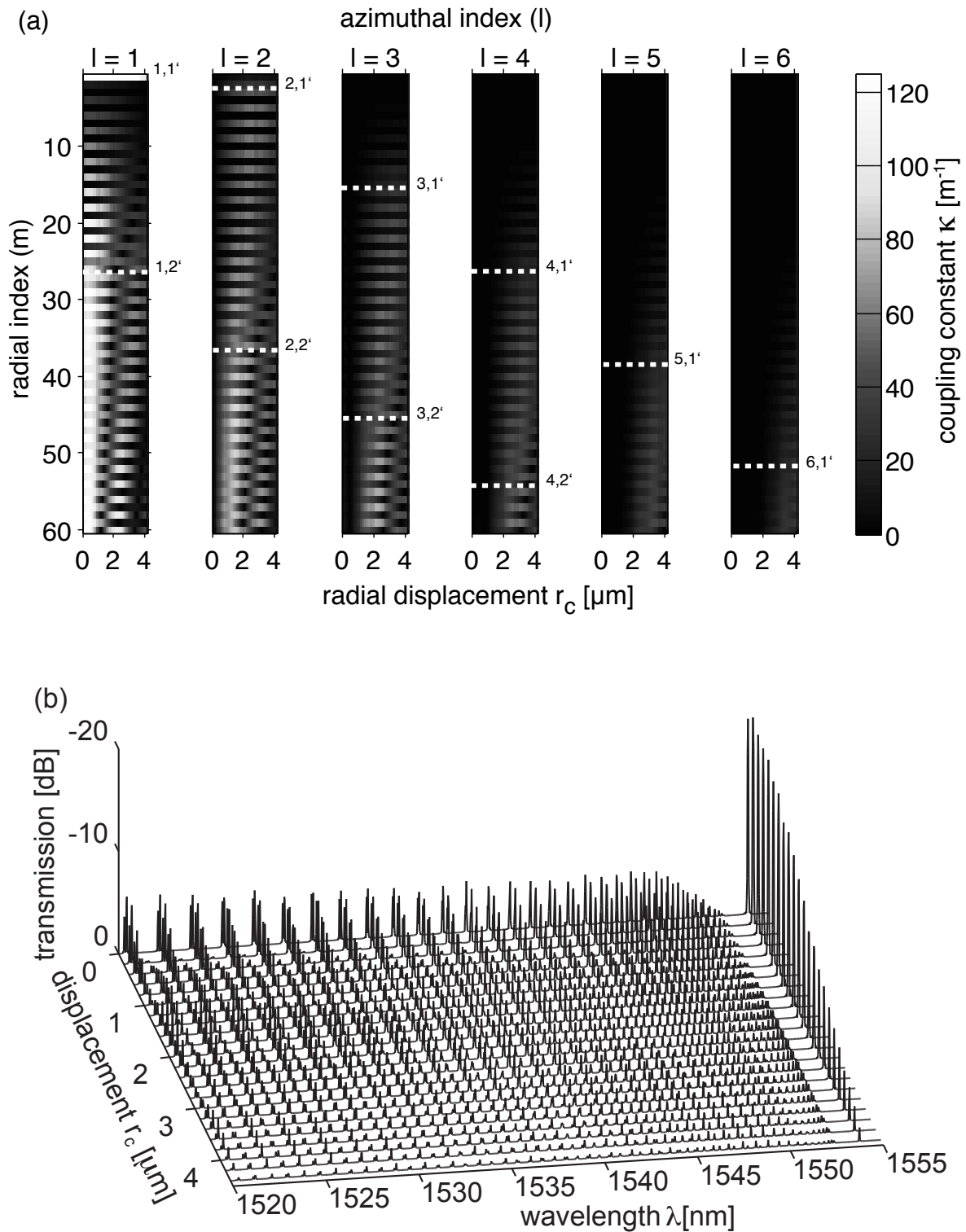
Fig. 6.3 Influence of the radial position r_c of the micro-void on the coupling constants fo the hybrid modes (a) and the corresponding transmission spectra (b).

of interest, most l can be neglected, if their $U_{l,1'}$ cut-off lies beyond that m. E.g. if the spectrum to be considered does not include cladding modes with $m > 30$, only cladding modes with $l \leq 4$ have to be taken into account (compare Fig. 6.3(a)).

6.3 Resonances and degeneracies

All effective refractive indices $\bar{n}_{lm}$ of the cladding modes were calculated with the fiber data provided in Tab. 6.1 by solving the dispersion relations for TE, TM and hybrid HE and EH modes (Eq. A.1, Eq. A.2 and Eq. A.3).

Calculating the resonance wavelengths λ_{lm} from the effective refractive indices $\bar{n}_{lm}$ and the grating period Λ is not as straight forward as in the few mode case (Eq. 5.1), since the resonances spread over a broad wavelength range. Thus, waveguide dispersion has to be taken into account and $\bar{n}_{lm} = \bar{n}_{lm}(\lambda)$. A way to avoid having to solve the dispersion relations for each resonant wavelength, is to interpolate the propagation constants from the effective refractive indices computed at the highest wavelength λ_0, which is the resonance wavelength of the fundamental core mode in this case. For a highly multimode fiber, the propagation constants can be approximated [Sal91] by

$$\beta_{lm} \approx \left(n_1^2 \left(\frac{2\pi}{\lambda} \right) - A_{lm} \right)^{1/2} \text{ with } A_{lm} = (n_1^2 - \bar{n}_{lm}^2) \left(\frac{2\pi}{\lambda_0} \right). \tag{6.2}$$

Inserting these terms into the FBG phase condition (Eq. 2.36) yields a quadratic equation for the wavelength of the (l, m) resonance, which has two solutions [Tho11b]

$$\lambda_{lm} = \frac{\frac{\bar{n}_{11}}{\Lambda} \pm \left[\left(\frac{\bar{n}_{11}}{\Lambda} \right)^2 + \frac{1}{4\pi^2} \left(\tilde{A}_{lm} + \left(\frac{2\pi}{\Lambda} \right)^2 \right) (\bar{n}_{lm}^2 - (\bar{n}_{11})^2) \right]^{1/2}}{\frac{1}{4\pi^2} \left(\tilde{A}_{lm} + \left(\frac{2\pi}{\Lambda} \right)^2 \right)}, \tag{6.3}$$

where the positive root gives the FBG solution for coupling into the counterpropagating mode, while the negative root would be for the LPG case (coupling to modes propagating in the same direction). Hence, all fields were computed by inserting the effective refractive indices $\bar{n}_{lm}$ into the field expressions (Eq. A.12) and evaluating the field overlap (Eq. 2.30).

The spectral positions of the cladding mode resonances are plotted as vertical lines in Fig. 6.4, where the length of the line corresponds to the amplitude of the respective

coupling constant κ_{lm}. The resonances are also sorted by their azimuthal order: From bottom to top, the azimuthal index l increases from 0 to 4.

All resonances appear in pairs, except for the fundamental $HE_{1,1}$ resonance at 1555 nm. TE and TM resonances are plotted in the bottom row ($l = 0$). The TE modes are marked as solid lines and the TM modes as dotted lines. For wavelengths above $U_{0,2'}$ TE and TM resonances are degenerate. Below $U_{0,2'}$, they appear in doublets, with TE modes being on the higher wavelength side.

The hybrid modes are plotted with acending $l \geq 0$ in the rows above with solid lines for HE modes and dotted ones for EH modes. HE and EH modes are strictly alternating. At each resonance doublet, the HE resonance is at the higher wavelength side. In certain wavelength regimes, the difference between the propagation constants of HE and EH resonances also becomes small. This happens between the $U_{1,2'}$ an the $U_{1,3'}$ cut-off as well as between the $U_{1,2'}$ an the $U_{1,3'}$ cut-off.

The azimuthal classes of cladding mode resonances form to sets: TE/TM doublets are degenrate with hybrid doublets of $l = 2, 4, 6, \ldots$, while the fundamental $l = 1$ resonances are acompagnied by $l = 3, 5, 7, \ldots$. In the following, all resonances are labelled with $\ell = 2$ and $\ell = 1$ depending if coupling to modes with even or odd l occurs. These ℓ, m labels are displayed in the bottom row of Fig. 6.4. The integer m increases with decreasing $\bar{n}$. For clarity, only every second label has been plotted.

The fields of the hybrid modes are not circularly symmetric, in contrast to the TE and TM fields. Therefore, each hybrid mode has a rotated, degenerated counterpart in order to realize any orientation of the field by superposition of them. As explained in Sec. 3, these subclasses are referred to as even and odd sets. As long as the modification is only translated on the coordinate axis perpendicular to the axis of polarization, no coupling from even to odd set occurs.

For any other orientation of the micro-void with respect to the polarization axis of the incident mode, this requirement is not met. For example, if the microvoid (as described by Eq. 6.1) has been displaced by 800 nm in x-direction and 700 nm in y-direction as depicted in the inset of Fig. 6.4. Without loss of generality it is assumed that only the even $HE_{1,1}$ mode is incident. The amplitudes of the odd coupling constants κ_{lm}^{odd} are
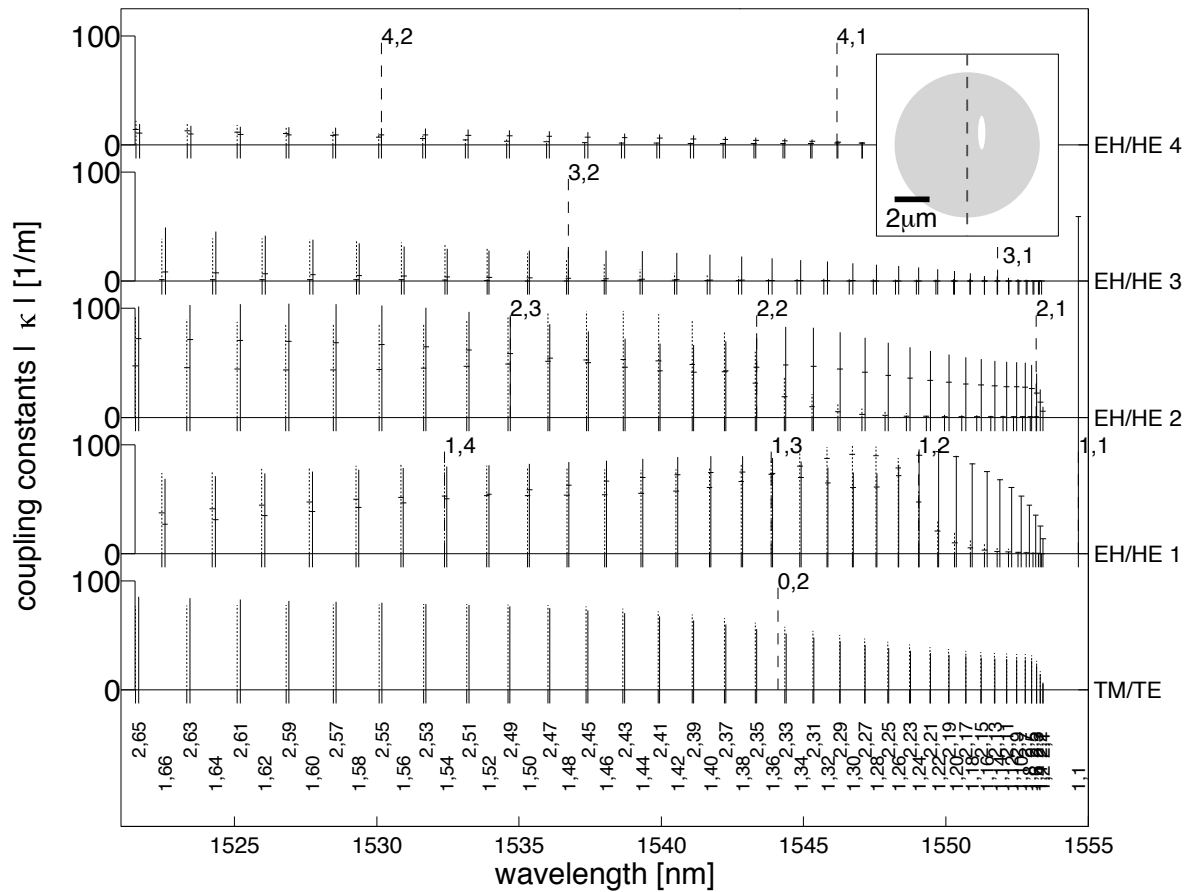
Fig. 6.4 Spectrally sorted cladding mode resonances and their corresponding coupling constants (vertically lines) for a micro-void grating that is displaced both in x and y direction (inset). The solid lines are TE or HE modes, the dotted lines represent TM and EH modes. Without loss of generality, only the even $HE_{1,1}$ mode is incident. The hybrid modes ($l \geq 1$) appear in degenerate pairs of even and odd modes. Their contributions are marked with the small vertical lines that divide the vertical ones: the lower part marks the part that is coupled in the even mode, while the upper part couples into the odd one. The vertical dashed lines are the virtual cut-offs that mark a principal change in the core fields of the cladding modes.

plotted on top of the even coupling constants $\kappa_{lm}^{\mathrm{even}}$, seperated by small horizontal dash. A general observation in this example, is that the coupling constants for a higher azimuthal mode class are usually smaller than those of the lower ones and that coupling to modes with $l > 4$ can already be neglected. Since the higher azimuthal modes are always degenerate with a lower one, they are hard to be observed directly. They can be observed indirectly in the interference patterns as will be shown in the next section. Another observation is that the coupling behaviour significantly changes for hybrid cladding modes in the quasi TE/TM regime and many of the rules that hold strictly for the overlaps of the core modes (see Sec. 3) do not hold anymore: e.g. coupling to EH modes is now generally possible and of the same order of magnitude.

6.4 Multi mode coupling

6.4.1 Optical characterization

A free beam setup (Fig. 6.5) similar to that of [Egg00] was used characterize the FBG spectrally as well as to be able to image the reflected cladding modes. In order to address the narrow resonances individually, a swept wavelength system (SWS) was used instead of a broad band source. It is a commercial system (JDS Uniphase), which consists of a narrow line-width external cavity laser diode. Its emission wavelength can be continuously swept from 1520 nm to 1570 nm with a resolution of 3 pm. The delivery fiber is polarization maintaining (PM), providing a linearly polarized beam whose axis of polarization can be controlled by rotating the end of the PM fiber. The light of the PM fiber was coupled out with a 20x microscope objective (NA= 0.35) in order to obtain a collimated beam. That beam was hence coupled into the core of the fiber containing the FBG to be probed, using a 40x microscope objective (NA= 0.65). An IR-sensitive photodiode was mounted at the end of the fiber. By synchronizing its signal with the wavelength of the SWS, full transmission spectra can be recorded.

For imaging, the wavelength of the SWS was tuned to the specific wavelength of the resonance. The light reflected by the FBG is collimated by the same 40x objective, which has been used to launch the light into the core. A silvered mirror (reflectivity
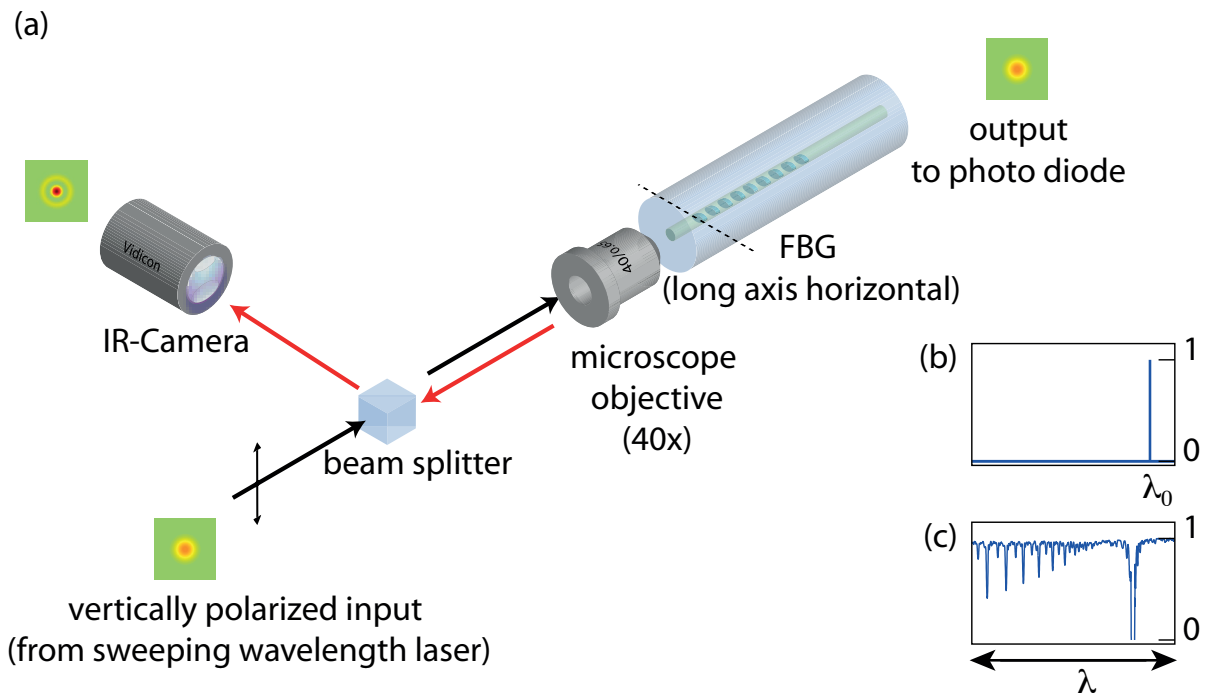
Fig. 6.5 Setup for measuring and imaging cladding mode coupling (a). The fundamental core mode of the single mode fiber is exited by free beam coupling with a microscope objective. Light source is a tunable narrow bandwith wavelength laser system. The insets (b) and (c) display the signal of the photo diode, which measures the transmitted amount of light. The spectra are normed for the signal measured at a wavelength λ_0 with no grating resonance (b). Tuning the wavelength while measuring the signal hence delivers a high resolution transmission spectrum (c). This allows for tuning the wavelength exactly at the cladding mode resonances for imaging the reflected modes.

≈ 50 percent) is placed in between launch and probe fiber for directing the reflected light to an IR sensitive camera (Vidicon).

A polarizer can be inserted before the camera to determine the polarization. By rotating the polarizer, four polarization classes can be distiguished:

- *Linear polarization:* The mode pattern does not change, if the linear polarizer is inserted. Rotating the polarizer does not change the pattern but its intensity, with the position of maximum and minimum intensity differing by 90°,

- *Radial polarization:* Inserting the polarizer introduces two intensity maxima along the axis of the polarizer and two *minima perperpendicular* to it. Rotating the polarizer, rotates this pattern but does not change its intensity.

- *Azimuthal rotation:* Analog to the radial polarization, but with the intensity maxima perpendicular and the *minima parallel* to the axis of the polarizer.

- *Complex or no polarization:* The mode patterns do not fit any of the above observations.

6.4.2 Multimode results with labelling and spectrum

Fig. 6.6 shows the transmission spectrum of the investigated FBG. The position of all resonance pairs could be numerically reproduced as described in Sec. 6.3. The labels (ℓ, m) agree with Fig. 6.4, identifying two sets of cladding modes resonances: those with $\ell = 1$ and those with $\ell = 2$, keeping in mind, that at these resonances modes with odd l or even l are degenerate. The radial index m counts both EH and HE modes within one of the sets. For each doublet, only the higher wavelength HE resonance is labelled.

At each resonance, the mode pattern was imaged. Typical mode patterns that were observed are plotted in Fig. 6.7. Qualitatively, there are three kinds of patterns: "rings" (Fig. 6.7 (a)), "bow ties" (Fig. 6.7 (b)) and "quad ties" (Fig. 6.7 (c,d)). These terms only refer to the number of lobes. However, there are many combinations of azimuthal modes that yield the same number of lobes as will be discussed in the following.

The horizontal lines in Fig. 6.6 indicicate, which patterns could be observed in which wavelength regime for both the $\ell = 1$ resonances (red) and the $\ell = 2$ resonances.
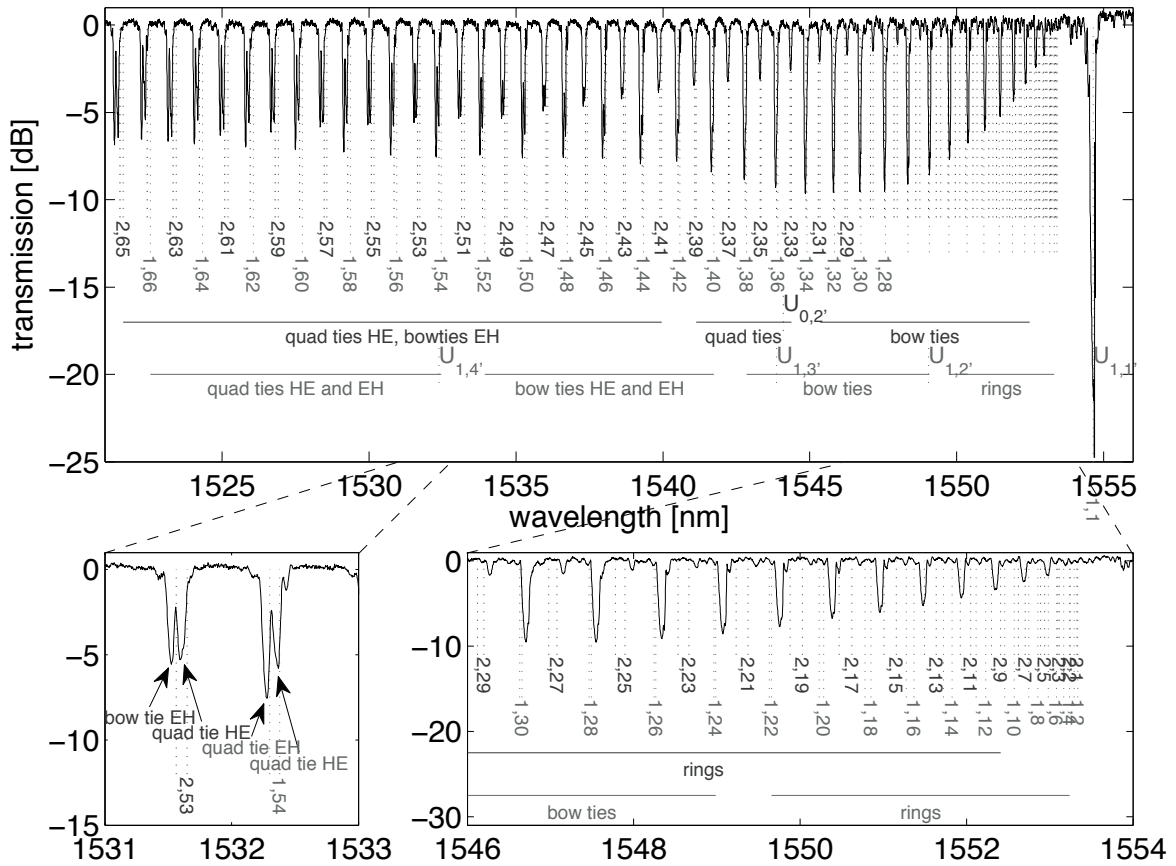
Fig. 6.6 Investigated transmission spectra with lowest azimuthal order vectorial labels (l, m). All numbers refer to the HE resonance, which is always the longer wavelength of the EH/HE or TE/TM doublets. The lower labels denote $\ell = 1$ modes, higher labels denote $\ell = 2$ modes. Horizontal lines below the spectrum indicate the range over which mode patterns of various form were observed. The virtual cutoffs are also labeled. The lower plots are magnifications of the main plot.

(1,18) 1550.79nm   (1,45) 1539.06nm   (2,39) 1540.91nm   (1,63) 1525.63nm
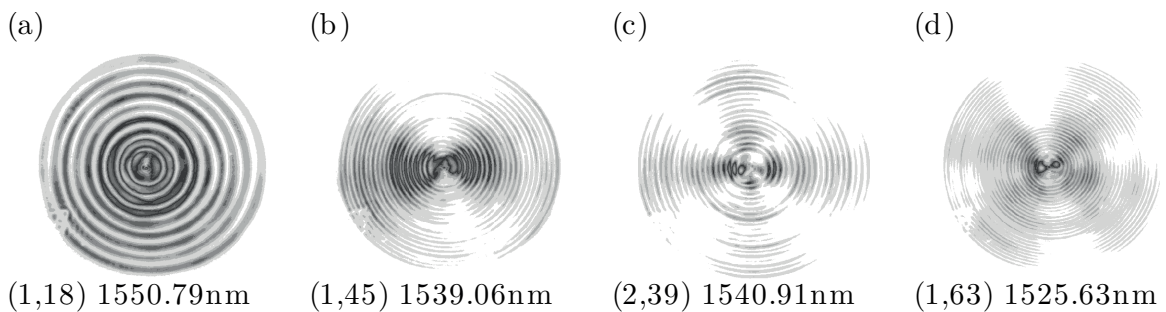
Fig. 6.7 Typical observed mode patterns of each class: (a) ring, (b) bow tie, (c) and (d) quad tie. Labels indicate the mode indices and the wavelength at which they were observed.

In the following, the reflections at representative resonances are discussed, since the patterns within one regime are alike and only differ by their number of rings. The full measurement, comprising all images is printed in the appendix B.

Starting from the fundamental Bragg peak of the core mode at the right hand side of Fig. 6.6, the observed mode patterns were linearly polarized in the same direction as the incident laser light. At the $\ell = 1$ resonances, patterns were ring-like, starting to exhibit a bow-tie like distribution approximately 5 nm from the Bragg peak. In contrast, the $\ell = 2$ resonances are bow tie shaped from the start.

At the point were the doublets appear in the spectrum (approximately 12 nm to the shorter wavelength side of the Bragg peak) the polarization of the mode patterns also change: The higher wavelength resonance of the doublet is predominantly azimuthally polarized, while the shorter wavelength resonance exhibits a mostly radial polarization. In this regime the patterns of the $\ell = 1$ resonances keep having a two-fold symmetry, with the axis of the higher wavelength resonance being perpendicular to the shorter wavelength one. The $\ell = 2$ mode patterns now have four lobes.

Approximately 20 nm to the shorter wavelength side of the fundamental Bragg peak, the polarization becomes more complex and cannot be unambiguously attributed. The mode patterns itself are now fourfold for both $\ell = 1$ and $\ell = 2$ resonances.

6.5 Reconstruction of the multi mode reflections

The three layer model has proven to be apt to correctly predict all resonances and their precise spectral position (Fig. 6.6). With this knowledge it is possible to answer for each resonance, what azimuthally degenerate cladding modes *could* possibly couple. The open question now is, to what extend the core mode the FBG *does* couple to these modes. The answer of the latter question heavily relies on whether the first question has been correctly answered. Have the resonances been correctly identified and labelled with the indices l and m? A good regime to test this, are those resonances, where coupling to a single counter propagating mode can be assumed. With the prerequisite that the intensities and polarizations of those resonances are correctly rendered by the

three-layer model, the multi mode reflections can be treated with confidence.

6.5.1 Conversion to a single mode

Even for highly localized FBG there are several subsets of the $\ell = 1$ resonances, where one can assume that the core mode couples only to a single cladding mode. In such cases, the expected mode profile is easily found in terms of the longitudinal component of the Poynting vector S_z. While the analytical expressions of the fields for $r > a_1$ become very lengthy [Erd97b, Tho11b, Tsa89a], the core fields ($r < a_1$) take the same form as the classic two-layer model [Sni61a] and S_z have the form

$$S_z(l, m) = \tfrac{1}{2}|E_{lm}|^2 \frac{\bar{n}}{Z_0} \frac{u_{lm}^2}{4} \left[(1-P)(1-Q)J_{l-1}(u_1 r)^2 + (1+P)(1+Q)J_{l+1}(u_1 r)^2 \right.$$
$$\left. -2(1-PQ)J_{l-1}(u_1 r)J_{l+1}(u_1 r)\cos[2(l\phi + \varphi)] \right]. \quad (6.4)$$

Here E_{lm} is a mode amplitude, Z_0 is the impedance of free space, $u_{lm} = (2\pi/\lambda)\sqrt{n_1^2 - \bar{n}^2}$, $Q = P\bar{n}_{lm}^2/n_1^2$ and P is a mode-dependent parameter that characterizes the relative EH/HE nature of the mode. Fig. 6.8 shows the measured (top row) and calculated (bottom two rows) mode profiles for a number of types $\ell = 1$ resonances which are now discussed.

The first case for which the reflection is to a single mode are resonances below the $U_{1,2'}$ cut-off. In that regime, most coupling constants are zero (Fig. 6.4) and in particular there is coupling to $EH_{1,m}$ modes, since they do not yet contribute to the electric field within the core. Coupling to cladding modes of higher azimuthal order l is negligibly small for the same reason [Tho11b]. Again, the forward propagating mode is solely the even $HE_{1,1}$ mode. Since the cladding modes for $m < U_{1,2'}$ are purely linearly polarized within the core, the electric field of the even $HE_{1,1}$ is perpendicular to an odd $HE_{1,m}$ at every point within the core. Thus the resulting coupling integrals are always zero - independent of the FBG cross-section [Tho11b]. Consequently only coupling to even $HE_{1,m}$ modes is possible.

For $m < U_{1,2'}$, $P \approx \pm 1$ and $Q \approx P$ so the second term in Eq. 6.4 with the cosine dependence drops out and the mode intensity is azimuthally constant. The electric and magnetic fields for the cladding have the same azimuthal dependence (their analytic

expressions are given in the appendix). Thus, the computed intensity patterns of the $HE_{1,m}$ modes are ring-like while their polarization is linear (Fig. 6.8 (a,b)). In the investigated FBG, these are the $\ell = 1$ resonances between the fundamental Bragg peak and 1550 nm (Fig. 6.6). In this regime, the observed cladding modes (Fig. 6.8 (f,g)) are in excellent agreement with the predicted single mode reflections (Fig. 6.8 (a,b)): The measured and computed intensity S_z exhibits an equal number of rings. This confirms the radial index m of the analytical model in addition to the right resonance wavelength. The observed patterns exhibits almost no azimuthal dependence, which also agrees with the analytical expression as described above. In Sec. 6.4.1, it was observed that the modes in this wavelength regime were linearly polarized, with the axis of polarization parallel to that of the incident light. This behavior is also replicated by the computed single mode $HE_{1,m}$ fields. Because there is no coupling into the odd modes, the axis of polarization remains invariant. Thus the reflected pure $HE_{1,m}$ fields are linearly polarized along the y-axis, as the incident $HE_{1,1}$ mode (bottom row of Fig. 6.8 (a,b)) .

Above the $U_{1,2'}$ cut-off, the core mode can also couple to EH modes. The hybrid mode parameter now satisfies $|P| < 1$ for HE and $|P| > 1$ for EH modes (Sec. 3.2), so the cosine term in Eq. 6.4 becomes relevant. The modes now exhibit a $\cos(2\phi l)$ or more complex azimuthal intensity pattern. For the $\ell = 1$ resonances, these are the $\cos(2\phi)$ bow-ties (Fig. 6.8 (d,e), top). As explained in Sec. 3.4 the modes can now be regarded as quasi-TE or quasi-TM. Accordingly, the HE fields are predominantly azimuthally (Fig. 6.8 (d), top) and the EH fields radially polarized (Fig. 6.8 (e), top). However, the HE and EH modes are almost degenerate between the $U_{1,2'}$ and $U_{1,3'}$ cutoff (Fig. 6.4). Consequently, in this "intermediate" regime the mode patterns are already multi-mode and add to a predominantely linearly polarized superposition (Fig. 6.8 (c)).

Between the $U_{1,3'}$ and $U_{1,4'}$ cut-off, HE and EH modes can be separated again but are neither strictly single mode, since the coupling coefficients for the degenerate odd set of modes are now non-zero. However, the coupling to the odd mode set is still significantly smaller than to the even set, so that assuming single mode coupling to the even modes is a very good approximation. Indeed, the experimentally observed mode patterns ((1,38)-(1,52)) are hardly rotated (Fig. 6.8 (i,j)) with respect to the axis of polarization of the incident light: the azimuthally polarized HE bow ties are aligned along the

y-axis (Fig. 6.8 (d,i)), whereas the radially polarized EH bow ties are perpendicular (Fig. 6.8 (e,j)).

In conclusion, the vectorial three-layer model correctly renders the radial and azimuthal features of the intensity (Fig. 6.8, middle row) and the electric field (Fig. 6.8, bottom row), for single mode and predominantly single mode resonances. This excellent agreement with the experimental observations assures, that the analytical vector modes will provide solid building blocks for reproducing the multi-mode resonances, as will be described in the next section.
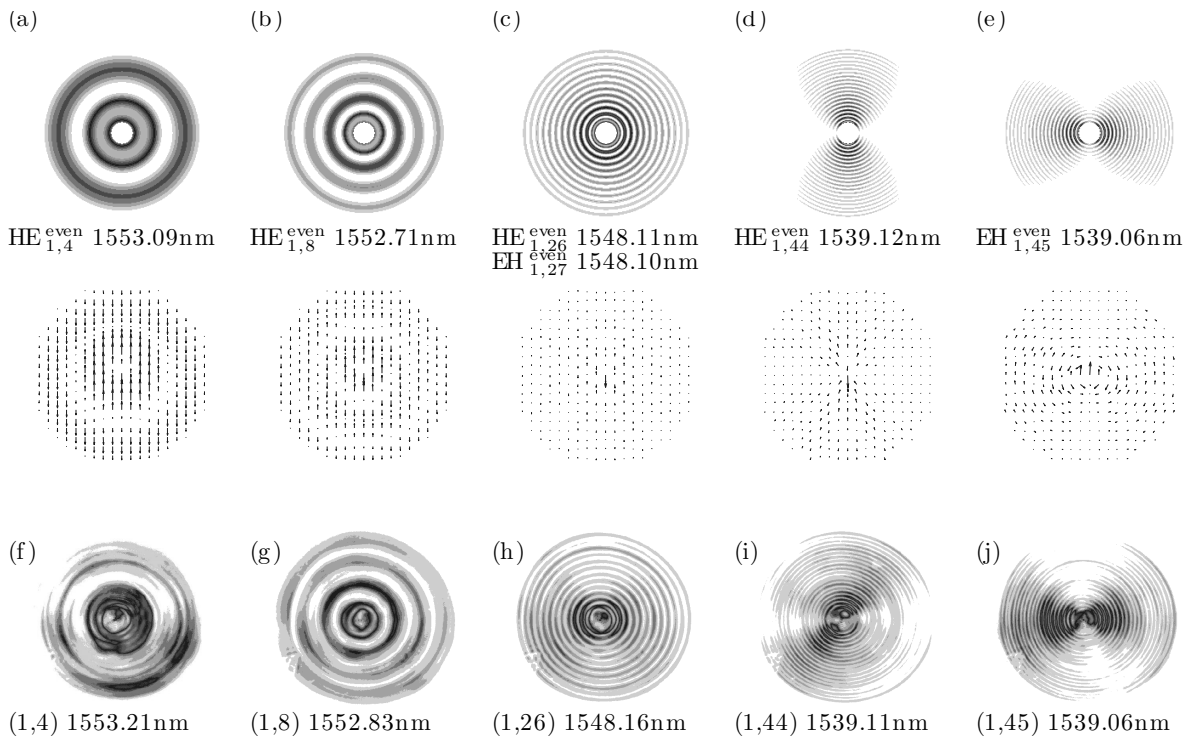

(a)   (b)   (c)   (d)   (e)

$HE_{1,4}^{even}$ 1553.09nm $HE_{1,8}^{even}$ 1552.71nm $HE_{1,26}^{even}$ 1548.11nm $EH_{1,27}^{even}$ 1548.10nm $HE_{1,44}^{even}$ 1539.12nm $EH_{1,45}^{even}$ 1539.06nm

(f)   (g)   (h)   (i)   (j)

(1,4) 1553.21nm   (1,8) 1552.83nm   (1,26) 1548.16nm   (1,44) 1539.11nm   (1,45) 1539.06nm

Fig. 6.8 Computed intensity distributions S_z (Fig. (a) - (e), top) and transversal electric fields E_t (Fig. (a) - (e), bottom). The bottom row (Fig. (f) - (j)) shows the corresponding measured patterns. Patterns (f) - (h) were fully linearly polarized, (i) was predominantly azimuthally polarized while the mode pattern at shorter wavelength (j) had a predominantly radial polarization. Note that all computed intensity distributions are single $l = 1$ modes, except for pattern (c), which is a superposition of the almost degenerate HE and EH mode with absolute square amplitudes of 0.5 and 0.4 respectively (for more explanation see next section).

6.5.2 Conversion to multiple modes

To reproduce the multimode reflection patterns, one has to compute the individual reflectivities of the degenerate modes from their coupling constants. Since the investigated FBG is point-by-point written, it can be assumed that the grating does not change over its length L, neither in its period nor its strength. In a single mode reflection regime, the peak reflectivity could now be computed with $R = \tanh^2 \kappa L$ (e.g. [Erd97b]). Unfortunately, such simple solutions do not exist for multimode reflection, and the coupled mode equations have to be solved numerically [Erd97a]. Since the aim is not to compute the whole spectrum, but only the peak reflectivity of the degenerate modes at one resonance, these equations can be greatly simplified. At a resonance with N degenerate modes, the detuning (the phase mismatch) can be assumed to be zero for each mode. This reduces the coupled mode equations (Eq. 2.31) to a set of $N + 1$ coupled mode equations for the complex amplitudes A_{11} of the co-propagating core mode and the counterpropagating cladding modes B_{lm}:

$$\frac{\mathrm{d}A_{11}(z)}{\mathrm{d}z} = \sum_{l,m} -i\kappa_{lm} B_{lm}(z) \tag{6.5}$$

$$\frac{\mathrm{d}B_{lm}(z)}{\mathrm{d}z} = i\kappa_{lm} A_{11}(z). \tag{6.6}$$

This system of ordinary differential equations is then solved with the boundary conditions $A_{11}(z = -L/2) = 1$ and $B_{lm}(z = +L/2) = 0$. The percentage of light reflected into the cladding mode (l, m) is $R_{lm} = |B_{lm}(z = -L/2)|^2$. Since the fiber has been cleaved right at the position of the FBG (Fig. 6.5), the FBG starts at the end facet of the fiber where the light is coupled in. Because of shortness of the grating itself, both propagation-related phase changes and inter-modal coupling through fiber bends can be neglected for reflected light.

The reflected fields $\mathbf{E} = \sum B_{lm}\mathbf{E}_{lm}$ and $\mathbf{H} = \sum B_{lm}\mathbf{H}_{lm}$ are reconstructed by adding the fields of the modes with their respective amplitudes. The intensity of the reflected mode pattern is the real part of the Poynting vector $\mathbf{S} = \frac{1}{2}\mathbf{E} \times \mathbf{H}^*$. Since only the z component of $\mathbf{S}$ is real, it is given by $S_z = \frac{1}{2}(E_r H_\phi^+ - E_\phi H_r^*)$. In the following we use this procedure for reproducing the representative mode patterns shown in Fig. 6.9 ($\ell = 1$ modes) and Fig. 6.10 ($\ell = 2$ modes).

While for the previously discussed $\ell = 1$ resonances beyond the $U_{1,2'}$ cutoff it was not obvious from the pattern alone whether the reflected field was composed of single or multiple modes, the patterns observed beyond the $U_{1,4'}$ are clearly multimode. The observed asymmetries (Fig. 6.9 (b,d)) cannot result from a single mode, because then it would have a single azimuthal dependence following $\exp(i\phi l)$. Instead, the HE resonances now show a second, narrower 'bowtie', which is perpendicularly oriented to the $l = 1$ bowtie (Fig. 6.9 (b)). Reconstruction of its pattern using the calculated coupling coefficients reveals, that this feature results from a coherent superposition of odd $HE_{1,m}$ and $HE_{3,m}$ modes (Fig. 6.9 (a)). The same applies for the adjacent EH resonance (Fig. 6.9 (c)). In both cases, the resulting intensity distribution agrees with the observed pattern. Thus, the patterns are indeed a superposition of the even and odd $l = 1$ modes with light carried in the $l = 3$ mode. Note that this also holds for the adjacent resonance pairs (Appendix B).

(a)

$0.60 \ HE_{1,56}^{even}$
$0.10 \ HE_{1,56}^{odd}$

$0.00 \ HE_{3,54}^{even}$
$0.14 \ HE_{3,54}^{odd}$

(b)

$(1,56) \ 1530.65\,nm$

(c)

$0.43 \ EH_{1,57}^{even}$
$0.15 \ EH_{1,57}^{odd}$

$0.00 \ EH_{3,55}^{even}$
$0.19 \ EH_{3,55}^{odd}$
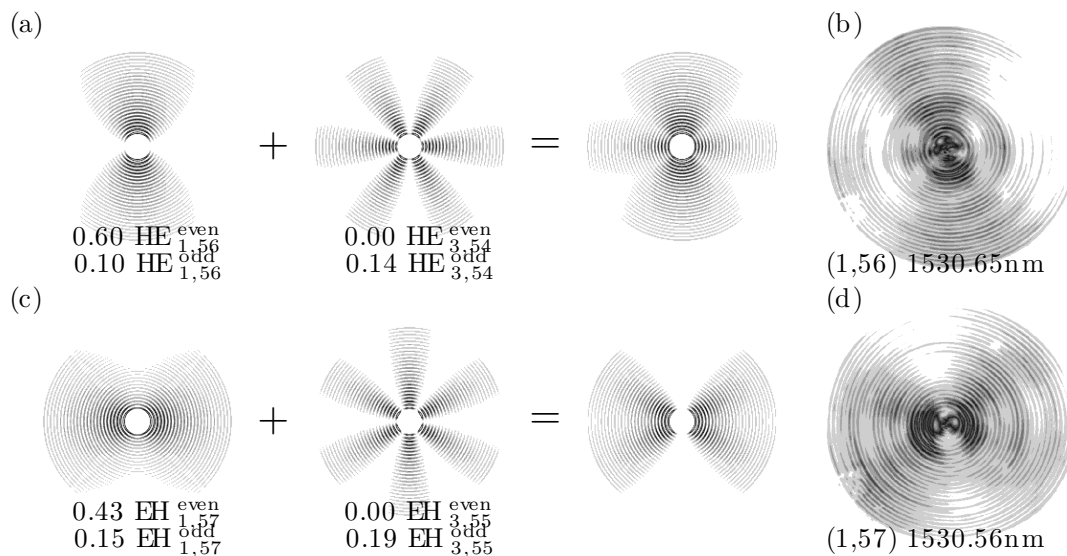
(d)

$(1,57) \ 1530.56\,nm$

Fig. 6.9 Computed ((a) and (c)) and measured ((b) and (d)) mode patterns for $\ell = 1$ multimode resonances.

In contrast to the $\ell = 1$, the $\ell = 2$ resonances are always multimode: below the $U_{0,2'}$ cut-off, TM, TE and even and odd $HE_{2,m}$ modes are degenerate ((Fig. 6.10) (a)). The EH modes are detuned and their coupling-coefficients are negligibly small. Above the $U_{0,2'}$ cut-off, the TE mode is still degenerate with the HE modes, the TM mode however now falls together with the EH modes ((Fig. 6.10) (d,f)). For the investigated grating the

$U_{0,2'}$ cut-off is located at 1544 nm, right at the transition point, where the modal images of the resonances start to exhibit a fourfold symmetry (Fig. 6.6).
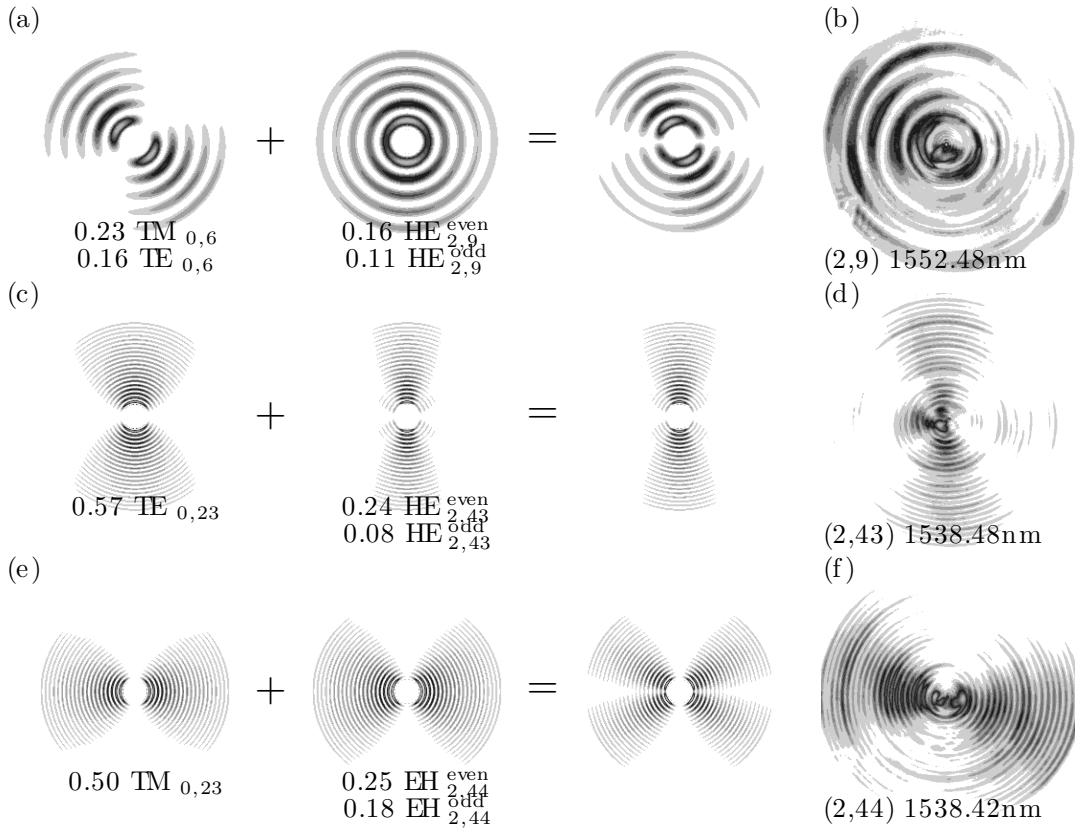
(a)
(b)

0.23 TM $_{0,6}$
0.16 TE $_{0,6}$

0.16 HE $_{2,9}^{\text{even}}$
0.11 HE $_{2,9}^{\text{odd}}$

(2,9) 1552.48nm

(c)
(d)

0.57 TE $_{0,23}$

0.24 HE $_{2,43}^{\text{even}}$
0.08 HE $_{2,43}^{\text{odd}}$

(2,43) 1538.48nm

(e)
(f)

0.50 TM $_{0,23}$

0.25 EH $_{2,44}^{\text{even}}$
0.18 EH $_{2,44}^{\text{odd}}$

(2,44) 1538.42nm

Fig. 6.10 Computed ((a),(c) and (e)) and measured ((b),(d) and (f)) mode patterns for $\ell = 2$ multimode resonances.

6.6 Conclusion

The aim of this chapter was to explore, to which extend the different mode classes can be accessed with a femtosecond pulse written fiber Bragg grating. This question could not have been answered with pre-knowledge, which modes are degenerate at each resonance. Without applying the full vectorial model of three layer step index fiber [Tsa89b], this study would not have been successful. The "virtual cut-offs" as they were introduced in Sec. 3.4, coincidence with the principal changes in the mode pattern. The relevant azimuthal mode classes were correctly predicted for the given wavelength regimes. This way, the polarization behavior for entire wavelength regimes can be identified. Each azimuthal mode class displays two fundamental coupling regimes: one,

where it behaves similar to equivalent hybrid core modes and one where the modes can be treated as quasi TE/TM. Apart from the expected coupling of the core mode $HE_{1,1}$ to cladding modes of the same azimuthal class $HE_{1,m}$, coupling to different azimuthal classes could be observed for a highly localized FBG. For the particular FBG, coupling to $TE_{0,m}$, $TM_{0,m}$, $HE_{1,m}$, $EH_{1,m}$, $HE_{2,m}$, $EH_{2,m}$, $HE_{3,m}$ and $EH_{3,m}$ cladding modes could be identified. Application examples of highly localized FBG with tailored cladding mode contributions will be discussed in Sec. 7.2 and Sec. 7.3.

7 Applications

The preceding chapters centered on how the cross section of ultra short pulse written FBG affects core and cladding mode coupling. In this chapter several examples are highlighted that demonstrate how the mode response of the fiber grating can be tailored for specific applications. Firstly, it will be demonstrated how the stability of a few mode fiber cavity benefits from suppression of mode conversion resonances. Highly localized FBG enable access to high radial order cladding modes as well as selected azimuthal groups. This will be discussed in the second and third section with emphasis on fiber sensor and laser applications.

7.1 Stable few mode fiber laser cavities

Ultra short pulse written FBG are especially attractive for applications in fiber lasers, since they can be directly inscribed into the active fiber cores . This feature has enabled monolithic splice-free continuous wave fiber cavities (Fig. 7.1). After the first demonstrations [Lai06, Wik06] in erbium-doped fibers, this concept was quickly adapted for other active fibers. Lasers could be realized with output wavelengths ranging from 1.064 nm [Wik07, Jov07, Jov07, Ber09c, Got11], encompassing 1480 nm [And07, And08] and providing emission in the eye-safe far IR, like 2 µm [Zha09a, Zha09b, Son09] up to 2.8 µm [Ber09a]. Most recently, a monolithic laser in a band gap fiber could be demonstrated [Got11]. However, all the aforementioned examples were realized in single mode fibers. With these configurations power scaling was possible up to 100 W [Jov07], limited by non-linear effects. Transitions to large mode area step index fibers were tried in Thulium doped fiber but yielded unstable multi modal output [Zha09a].
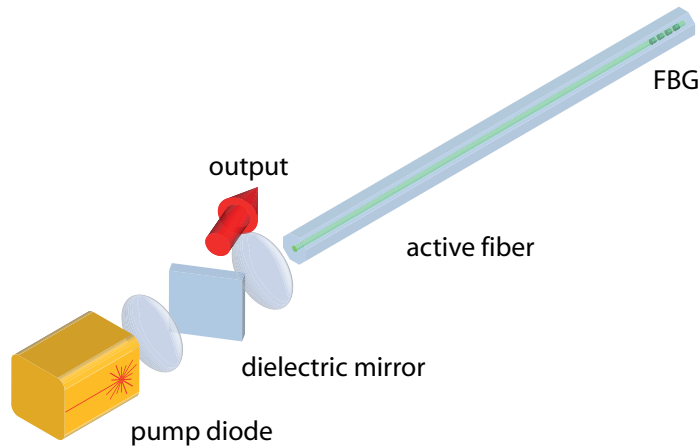
Fig. 7.1 Laser setup for characterizing the performance of the large cross-section FBG in active LMA fibers. Note that a single piece of fiber is used and no splices were necessary. In this case, the fiber cavity is determined by the FBG and the Fresnel reflection at the other fiber end.

Radius	Refractive index
$a_1 = 10.5 \ \mu m$	$n_1 = 1.4466$
$a_2 = 200 \ \mu m$	$n_2 = 1.4454$

Tab. 7.1 Fiber geometry of the Nufern LMA-YDF-20/400 fiber.

For the following examples, an ytterbium doped step index large mode area (LMA) fiber (Nufern LMA-YDF-20/400) was used, which allows for drastic power scaling. Its geometrical properties are summarized in Tab. 7.1. At 1080 nm the core has a V-parameter (Eq. 2.23) of $V = 3.7$. It therefore supports three (scalar) LP modes: $LP_{0,1}$, $LP_{1,1}$ and $LP_{0,2}$ [Sal91].

A continuous wave fiber laser cavity was obtained by inscribing high reflective (HR) FBG at the end of up to ten meter long fibers (Fig. 7.1). The other end of the fiber has been cleaved and polished and serves as a broad band low reflectivity mirror due to approximately 4 percent Fresnel reflection. The fiber is pumped with a diode that delivers up to 500 W of IR output at 976 nm. A dielectric mirror in between diode and fiber end facet is used as output coupler. The FBG is mounted on a Peltier element in order to stabilize the output wavelength.

An unstable multi-wavelength output like in [Zha09a] could also be observed with fiber cavities, where a transversally inhomogenous large cross-section FBG has been inscribed. The resulting output spectra in Fig. 7.2 have been recorded in 1 s intervals. Always, multiple peaks are present, whose amplitude is never stable. In addition, the HR grating is leaking up to 30 percent of the output power in higher order mode (inset). The laser output is of poor beam quality ($M^2 > 2.6$). With this very unstable cavity, power scaling is barely possible above 50 W and often requires a renewal of fiber and FBG [Han88]. The instabilities can be explained with the large cross-section FBG supporting *mode conversion* resonances as characterized in detail in Sec. 5.3.2.
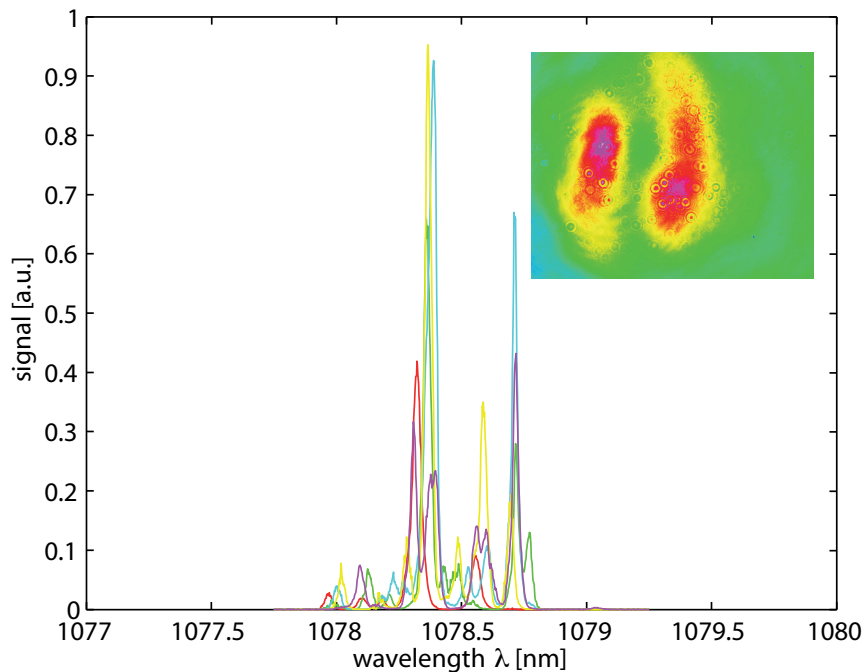
Fig. 7.2 Output spectrum of a non-stable fiber cavity, showing several snapshots taken each second. The inset shows the light that leaks out *behind* the high reflectivity FBG.

A mode conversion suppressing large cross-section FBG similar to the one investigated in sec. 5.3.3 yielded a much more stable output. It has been inscribed using the phase mask scanning technique as detailed in sec. 4.3. The stage with phase mask and fiber was translated by $d_x = 40$ µm perpendicular to the fiber axis with a velocity of $v_x = 0.5$ mm/min while fiber and phase mask were exposed to 250 µJ pulses. Thus, the large cross-section FBG covers the whole core and its surrounding. The grating length

is $L = 10$ mm and the grating period $\Lambda = 0.743$ µm, reflecting 1080 nm light in second order (Eq. 5.1). The spectrum is dominated by the broad self coupling peak (Fig. 7.3) similar to the spectrum of the large cross-section FBG in Fig. 5.7.
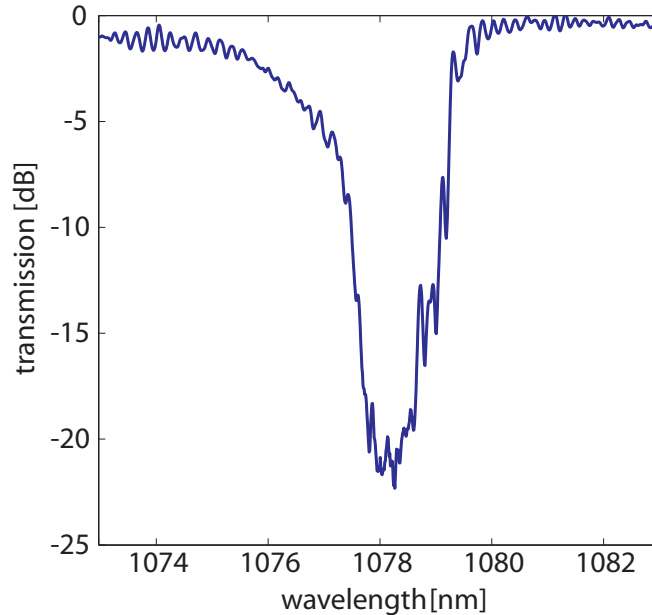

Fig. 7.3 Transmission spectrum of large cross section FBG in a ytterbium doped LMA fiber (Nufern LMA-YDF-20/400).

At 30 W, the cavity with the mode conversion suppressing large cross-section FBG lases at two wavelengths (Fig. 7.4 (a)) with stable output (root mean square of less than 0.5 percent). The output beam was spectrally separated with the aid of a highly tilted bulk diffraction grating [Stu11]. The resulting pictures (inset of Fig. 7.4(a)) reveal, that the two laser peaks correspond to the $LP_{0,1}$ and $LP_{1,1}$ mode. Lasing at the $LP_{0,2}$ resonance could not be observed.

It was possible to scale the output power above 200 W, with an overall efficiency of 43 percent, only limited by the power of the pump diode. At these power levels, the bandwidth of the emission peaks broadened and a third peak to the higher wavelength side appeared (Fig. 7.4 (b)). An explanation for these effects could be the inhomogenous thermal longitudinal profile of the FBG due to insufficient cooling. This can cause a shift of the resonant wavelength as well as spectral broadening due to a chirped period [Erd97b].
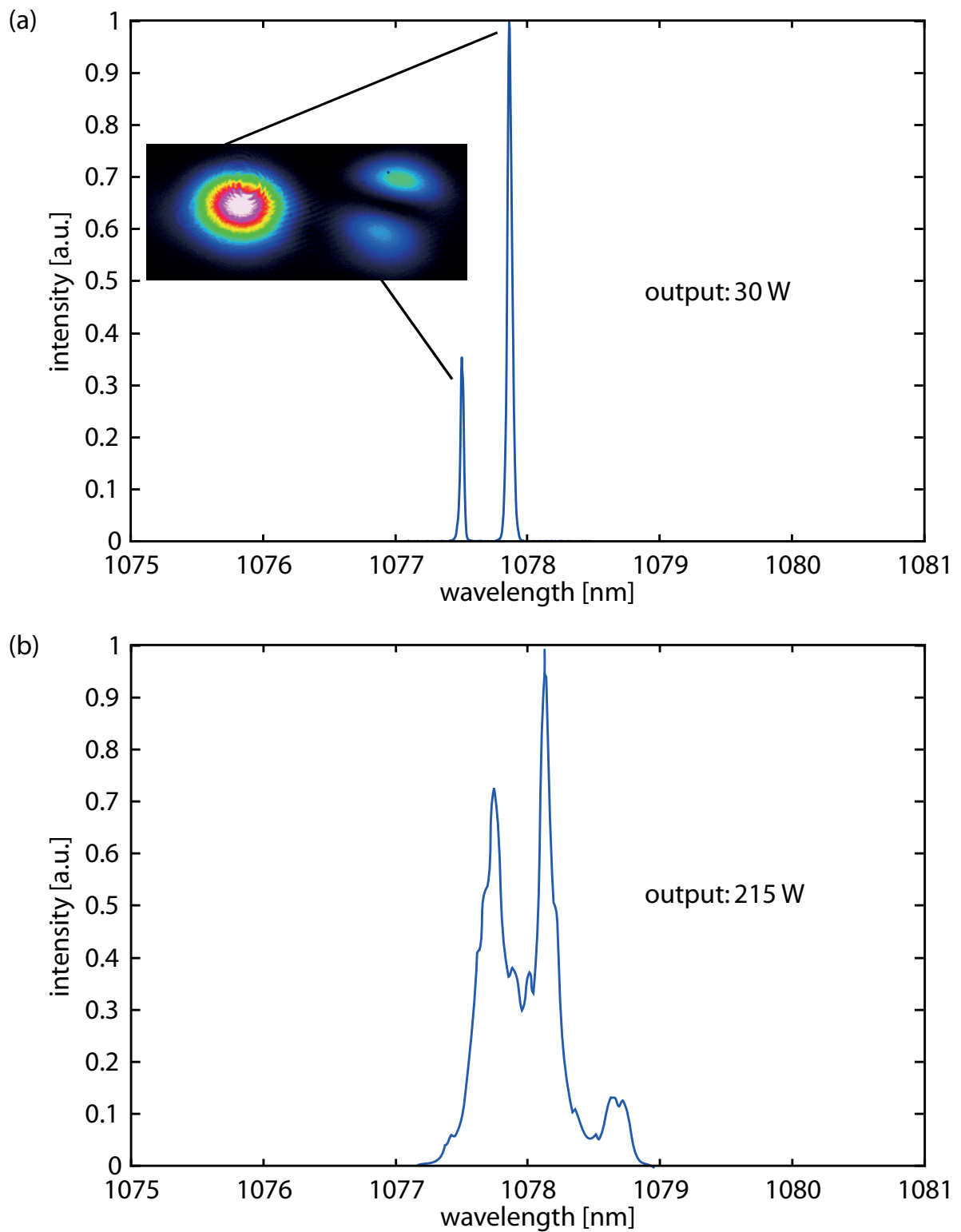
Fig. 7.4 Output spectrum of the monolithic fiber laser cavity for 30 W (a) and 215 W (2). The inset in Fig. (a) shows the spectrally separated beam profile [Stu11].

Ongoing research is on further improving beam quality of the laser by suppressing the $LP_{1,1}$ as well with a modified Fabry-Perot cavity [Stu10]. In conclusion, the stability of the few mode fiber laser cavity depends on how well mode conversion is avoided. There are however scenarios, where a mixed mode cavity might be desired. An example will be discussed in sec. 7.3.

7.2 Accessing high radial order cladding modes

Rather than for lasers, mode converting gratings are used for fiber sensors. Here, coupling to higher order modes is desired in order to make the signal of the fundamental mode sensitive to fiber bends, temperature or the outer refractive index [Ker97]. The higher the radial order of the cladding mode, the stronger the mode interacts with the exterior of the fiber via its evanescent field. An impressive recent example for such a sensor are fibers that are layered with gold or copper nano particles. Here, the plasmon resonances have been excited with weakly tilted FBG [She08, Sha11], reacting sensitive to the exterior refractive index. Heavily tilted FBG can be used to access EH modes of higher radial order, realizing highly responsive strain and refractive index sensors with low thermal dependence [Zho06]. However, tilting the fiber grating comes at the expense of higher insertion loses due to radiation mode coupling [Wal09, Erd96].

Highly localized FBG can serve as an alternative to tilted FBG (Eq. 3.12), since strong coupling to high radial order FBG can be achieved with low insertion losses. An example of a direct written FBG ($L = 40$ mm, $r_c > 1$ μm) is plotted in Fig. 7.5: the fundamental Bragg peak at 1540 nm in (Fig. 7.5) is more than -50 dB deep. Likewise, the cladding mode resonances to the lower wavelength side of the Bragg wavelength are very strong. Here, the amount of core light that is coupled into cladding modes surpasses 70 percent at resonances even 20 nm from the Bragg wavelength [Tho11b].

Because of the steep refractive index contrast of the micro-void, the longitudinal refractive index profile of the FBG can be assumed to be almost rectangular (Eq. 2.27), which yields strong higher Fourier components (Eq. 2.26). While the second Fourier order reflection can be observed in the wavelength regime of standard telecommunication

fibers between 1500 nm and 1600 nm (Eq. 2.36), the first order Bragg-peak is located in the mid-IR around $\lambda = 3\ \mu m$. The tail of first order cladding mode resonances reaches down to the second order Bragg peak, thus spanning a whole octave of the spectrum (see peaks in Fig. 7.5 at $\lambda > 1540$ nm.).
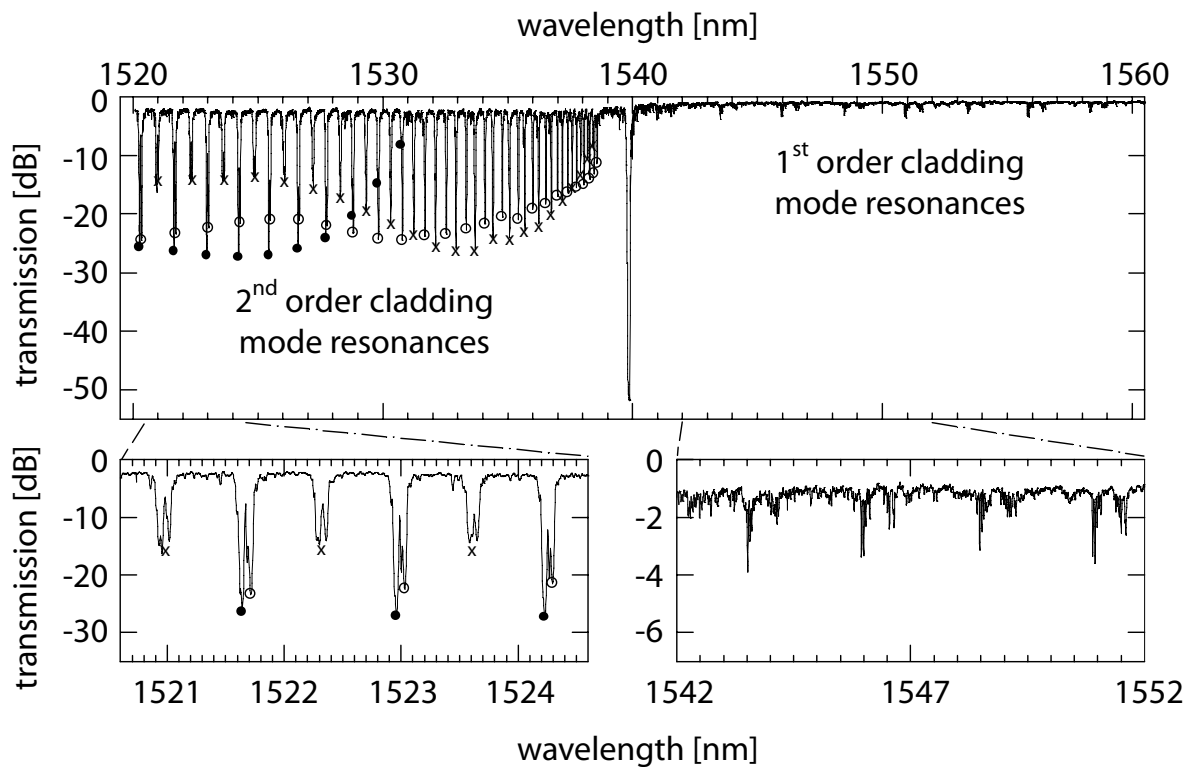

Fig. 7.5 Transmission spectrum of a strong FBG written with the point by point technique and ultra short pulses. Strong resonances that result from the first and second Fourier order of the grating can be observed. The second order reflection peak of the fundamental core mode is located at 1540 nm. At the shorter wavelength side, the second order cladding mode resonances can be observed. Below 1530 nm, the second order resonances appear as doublets (left inset). This is also the case for the tail of the first order resonances ($\lambda > 1542$ nm).

The three well defined envelopes can be identified in the spectrum (marked with circles and crosses). The envelopes marked with circles correspond to odd l resonances while the crosses mark even l resonances as detailed in sec. 6.3. Below 1530 nm, coupling to EH modes also becomes significant (filled circles). This coupling can be explained by the transition to the quasi-TM and quasi TE regime (sec. 3.4): Although the modes

are formally hybrid HE and EH modes, their fields are predominantly radially and azimuthally polarized. The HE/EH doublets (Fig. 7.5, left inset) can be exploited as polarization filters [Mou09] or for discriminating strain and temperature of the fiber [Zho06].

7.3 Selective excitation of cladding mode classes

A recent approach to realize high power fiber lasers is to use the cladding of the fiber as amplifying medium as well [Ram08, Suz08, SR11]. Here, one FBG sets the lasing wavelength as narrow band cavity mirror, while a second fiber grating (either a LPG or a FBG) converts from core to cladding modes. Linearly polarized and circular symmetric cladding modes are desired for efficient pump conversion and stability [Ram08]. Thus, an ideal mode converter should target only a small subset of the cladding modes: $HE_{1,m}$ modes with $u'_{1m} < U_{1,2'}$, since cladding mode fields with a higher normalized wavenumber exhibit an azimuthal dependence (see sec. 3.4). In this regime, coupling to higher azimuthal order modes of up to $l = 3$ has to be considered, as can be deduced from Fig. 3.2. Hybrid modes of higher azimuthal index l can be neglected, since they have no field at the core, which is expressed by their virtual cut-offs $U_{l,1'} > U_{1,2'}$.

In a standard telecommunication fiber as used for Erbium fiber lasers (Tab. 6.1), the first eleven $HE_{1,m}$ cladding modes are circular symmetric (Fig. 6.4). For the cladding mode spectra plotted in Fig. 7.6, the $U_{1,2'}$ cut-off is located at 1549 nm, marked with a vertical dashed line. In the wavelength regime from 1549-1555 nm, only coupling to the $TE_{0,m}$, $TM_{0,m}$, $HE_{1,m}$, $HE_{2,m}$ and $HE_{3,m}$ cladding modes has to be considered. The transversal cross section of the FBG can now be used to enhance or suppress coupling to one or more of these mode classes. For this particular example, it would favorable to avoid coupling to any other than the $HE_{1,m}$ modes. This can be achieved by centering the highly localized FBG (Fig. 6.3). Fig. 7.6 (a,c) show the measured spectra for two different radial positions r_c of the highly localized FBG (compare Fig. 6.2). Corresponding spectra have been rendered according to the approximate position of the micro-voids as it could be deduced by microscope pictures (Fig. 7.6 (c,d)). Note that the better the FBG is centered, the weaker the coupling to even l cladding modes becomes, so that the cladding mode

spectrum for pure $l = 1$ mode coupling has only one envelope.

In conclusion, *highly localized* FBG can enhance coupling to cladding mode. The precise control of the transversal position of the highly localized FBG allows for selective excitation of cladding mode classes.
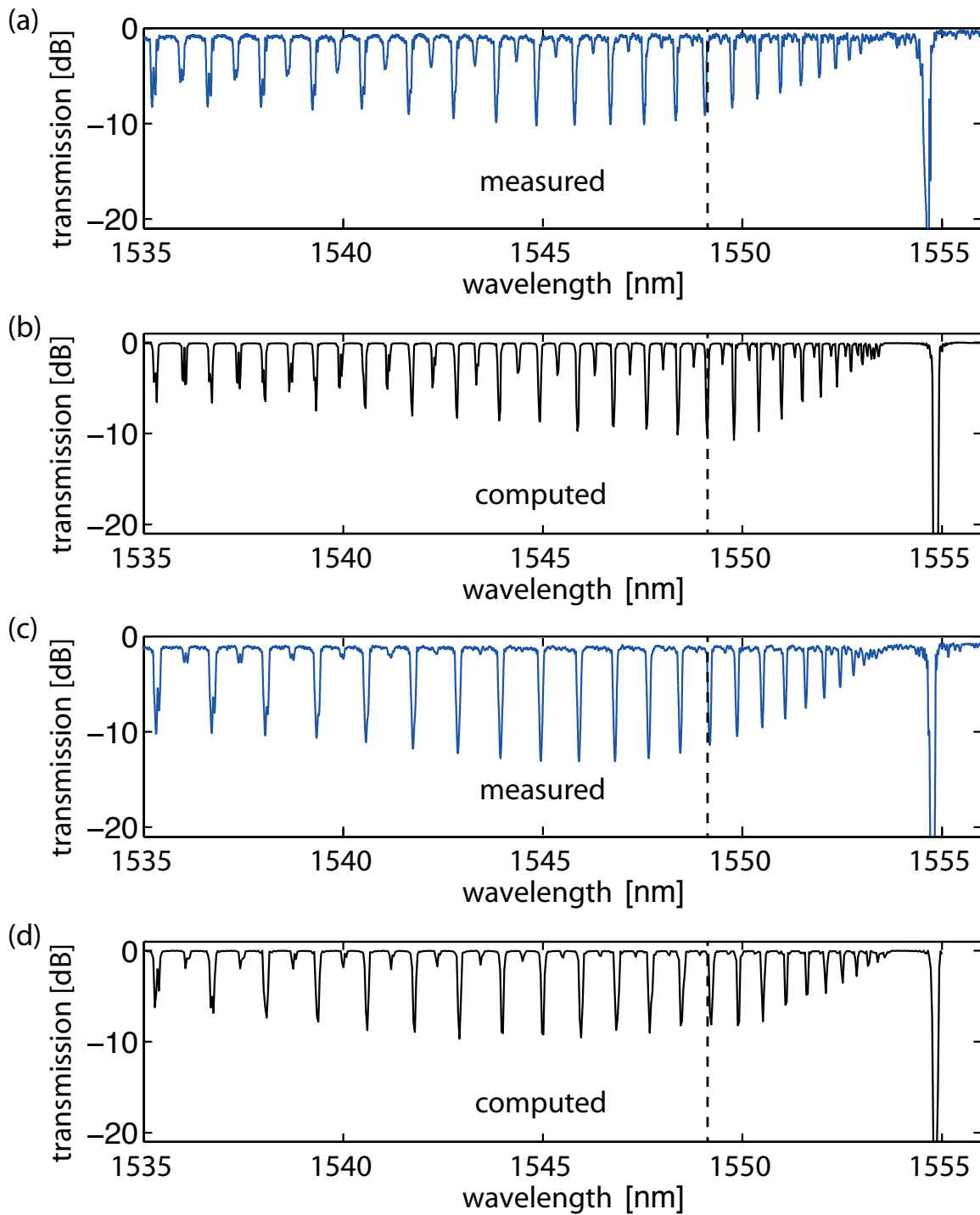
Fig. 7.6 Comparison of the measured spectra of highly localized FBG being differently well centered ((a) and (c)). Spectra have been computed for a radial displacement r_c of 0.7 µm (b) and 0.3 µm (d).

8 Conclusion and outlook

Focussed ultra short laser pulses allow for a defined and localized refractive index modification that does not depend on the photo sensitivity of the material [Nol03, Gat08]. These properties enable new possibilities for the fiber grating design, because the cross section can now be tailored. Fiber gratings with very large cross sections can be realized as well highly localized partial modifications of the fiber core. The aim of this thesis was a fundamental analysis of the interaction of the propagating light with such gratings.

In contrast to classic fiber gratings, many more fiber modes can be accessed since gratings with more elaborate symmetries can be inscribed. Especially coupling to higher azimuthal order modes is now possible. This made it necessary to extend existing theoretical work on fiber Bragg grating coupling [Erd97a, Lee01], in order to take such modes into account. Based on the foundation of the coupled mode theory [Kog79] and the vectorial expressions of step index fiber modes [Sni61a, Sny78, Tsa89b], the general coupling behavior of bound core and cladding modes was investigated.

For the experimental analysis of the coupling properties, the fiber grating spectra had to be supplemented with spatial measurements. Intensity and polarization have to be taken into account in order to resolve ambiguities of the modal content. Employing a spatial light modulator, the spectral response of Bragg gratings in few mode fiber were investigated for different modal excitation. A detailed analysis revealed the higher azimuthal order mode content in cladding mode reflection of a highly localized FBG [Tho11b].

These experimental methods and the theoretical frame work served as foundation for designing the spatial features of the fiber grating in regard to specific applications. A high reflectivity FBG with mode conversion suppression was inscribed in an ytterbium

doped large mode area fiber. Hence, with this monolithic fiber cavity, stable two mode lasing at high powers could be demonstrated. In a single mode fiber, coupling to specific azimuthal classes of cladding modes can be controlled by the radial position of a highly localized FBG. This ability can be used to tailor the cladding mode coupling for specific sensor and mode conversion applications.

In conclusion, ultra short pulse written FBG allow for a new generation of tailored in-fiber optical elements. Ongoing and future work is on combining these new transversal design possibilities with longitudinal and non-linear features: E.g. ultra-broad, apodized FBG [Tho07, Voi09, Ber09b, Voi11] for dispersion management in all-fiber ultrashort pulse laser or Fabry-Perot cavities with transversally varying cross section for further mode discrimination [Stu10].

A Three layered step index fiber

Dispersion relations

The TE resonances were found by solving the dispersion relation

$$J\left(Kp_l(a_2) + \frac{r_l(a_2)}{u_2}\right) - \frac{1}{u_2}\left(Kq_l(a_2) + \frac{s_l(a_2)}{u_2}\right) = 0, \tag{A.1}$$

and the TM modes with

$$J\left(Kp_l(a_2) + \frac{n_2^2}{n_3^2}\frac{r_l(a_2)}{u_2}\right) - \frac{n_2^2}{n_1^2}\frac{1}{u_2}\left(Kq_l(a_2) + \frac{n_2^2}{n_3^2}\frac{s_l(a_2)}{u_2}\right) = 0. \tag{A.2}$$

The hybrid EH and HE modes have a more impressive dispersion relation with

$$\zeta_0 = \zeta_0', \tag{A.3a}$$

where

$$\zeta_0 = \frac{1}{\sigma}\frac{u_2\left(JK + \frac{\sigma^2 v_{21} v_{32}}{n_2^2 a_1 a_2}\right)p_l(a_2) - Kq_l(a_2) + Jr_l(a_2) - \frac{1}{u_2}s_l(a_2)}{-u_2\left(\frac{v_{32}}{n_2^2 a_2}J - \frac{v_{21}}{n_1^2 a_1}K\right)p_l(a_2) + \frac{v_{32}}{n_2^2 a_2}q_l(a_2) + \frac{v_{21}}{n_1^2 a_1}r_l(a_2)} \tag{A.3b}$$

$$\zeta_0' = \sigma\frac{u_2\left(\frac{v_{32}}{a_2}J - \frac{n_3^2 v_{21}}{n_2^2 a_1}K\right)p_l(a_2) - \frac{v_{32}}{a_2}q_l(a_2) - \frac{v_{21}}{a_1}r_l(a_2)}{u_2\left(\frac{n_3^2}{n_2^2}JK + \frac{\sigma^2 v_{21} v_{32}}{n_1^2 a_1}\right)p_l(a_2) - \frac{n_3^2}{n_1^2}Kq_l(a_2) + Jr_l(a_2) - \frac{n_2^2}{n_1^2 u_2}s_l(a_2)}. \tag{A.3c}$$

Here, the wave numbers

$$u_{lm}^2 = (2\pi/\lambda)^2(n_1^2 - \bar{n}^2), \qquad u_2^2 = (2\pi/\lambda)^2(n_2^2 - \bar{n}^2), \qquad w_3^2 = (2\pi/\lambda)^2(\bar{n}^2 - n_3^2), \tag{A.4}$$

are defined and

$$\sigma = il\bar{n}, \qquad v_{21} = \frac{1}{u_2^2} - \frac{1}{u_{lm}^2}, \qquad v_{32} = \frac{1}{w_3^2} + \frac{1}{u_2^2}, \qquad J = \frac{J_l'(u_{lm}a_1)}{u_{lm}J_l(u_{lm}a_1)}, \qquad K = \frac{K_l'(w_3 a_2)}{w_3 K_l(w_3 a_2)}. \tag{A.5}$$

The dispersion relations include Bessel-functions of the first and second kind J_n and N_n as well as modified Bessel-functions K_n of the second kind. In addition, the products

$$p_l(r) = J_l(u_2 r) N_l(u_2 a_1) - J_l(u_2 a_1) N_l(u_2 r), \tag{A.6a}$$

$$q_l(r) = J_l(u_2 r) N_l'(u_2 a_1) - J_l'(u_2 a_1) N_l(u_2 r), \tag{A.6b}$$

$$r_l(r) = J_l'(u_2 r) N_l(u_2 a_1) - J_l(u_2 a_1) N_l'(u_2 r), \tag{A.6c}$$

$$s_l(r) = J_l'(u_2 r) N_l'(u_2 a_1) - J_l'(u_2 a_1) N_l'(u_2 r), \tag{A.6d}$$

are used, where the prime stands for differentiation with respect to the total argument. Furthermore, the constant factor

$$C_{lm} = \frac{\pi a_1 u_{lm}^2 J_l(u_{lm} a_1)}{2} \tag{A.7}$$

is introduced to abbreviate the field expressions.

Virtual cut-off for TE and TM modes

Note that the dispersion relations for TE (Eq. A.1) and TM (Eq. A.2) have no discontinuities. Thus, the "virtual cut-off" definition as in section 3.4 does not apply in the strict sense here. An equivalent transition $U_{0,2'}$ can be defined for the wave vector u_1, where the TE and TM mode fields start to have their first ring within the core can be easily evaluated by setting $J_0'(u_1 a_1) = -J_1(u_1 a_1) = 0$, which happens at $u_1 a_1 = 3.8317$, slightly before $U_{2,2'}$.

Fields

TE fields

In cylindrical coordinates (r, ϕ, z), the electric $\mathbf{E}$ and magnetic $\mathbf{H}$ fields inside the core $(r < a_1)$ can be expressed in terms of Bessel functions J_n of the first kind as

$$E_z = \quad 0 \tag{A.8a}$$

$$E_r = \quad 0 \tag{A.8b}$$

$$E_\phi = \quad iE_{lm}u_1 J_0'(u_1 r)e^{i(\beta z - \omega t)} \tag{A.8c}$$

$$H_z = \quad E_{lm}\frac{\bar{n}}{Z_0}\frac{u_1^2}{\beta}J_0(u_1 r)\,e^{i(\beta z - \omega t)} \tag{A.8d}$$

$$H_r = -iE_{lm}\frac{\bar{n}}{Z_0}u_1 J_0'(u_1 r)\,e^{i(\beta z - \omega t)} \tag{A.8e}$$

$$H_\phi = \quad 0, \tag{A.8f}$$

Inside the cladding $(a_1 \leq r \leq a_2)$:

$$E_z^{\mathrm{cl}} = \quad 0 \tag{A.9a}$$

$$E_r^{\mathrm{cl}} = \quad 0 \tag{A.9b}$$

$$E_\phi^{\mathrm{cl}} = \quad iE_{lm}C_{lm}u_2 \left(-Jr_0(r) + \frac{s_0(r)}{u_2}\right)e^{i(\beta z - \omega t)} \tag{A.9c}$$

$$H_z^{\mathrm{cl}} = \quad E_{lm}C_{lm}\frac{\bar{n}}{Z_0}\frac{u_2^2}{\beta}\left(-Jp_0(r) + \frac{q_0(r)}{u_2}\right)e^{i(\beta z - \omega t)} \tag{A.9d}$$

$$H_r^{\mathrm{cl}} = (-)iE_{lm}C_{lm}\frac{\bar{n}}{Z_0}u_2 \left(-Jr_0(r) + \frac{s_0(r)}{u_2}\right)e^{i(\beta z - \omega t)} \tag{A.9e}$$

$$H_\phi^{\mathrm{cl}} = \quad 0. \tag{A.9f}$$

TM fields

In cylindrical coordinates (r, ϕ, z), the electric $\mathbf{E}$ and magnetic $\mathbf{H}$ fields inside the core $(r < a_1)$ can be expressed in terms of Bessel functions J_n of the first kind as

$$E_z = -iE_{lm}\bar{n}\frac{u_i^2}{\beta}J_0(u_1 r)e^{i(\beta z - \omega t)} \tag{A.10a}$$

$$E_r = -E_{lm}\bar{n}u_1 J_0'(u_1 r)e^{i(\beta z - \omega t)} \tag{A.10b}$$

$$E_\phi = 0 \tag{A.10c}$$

$$H_z = 0 \tag{A.10d}$$

$$H_r = 0 \tag{A.10e}$$

$$H_\phi = E_{lm}\frac{1}{Z_0}u_1 J_0'(u_1 r)e^{i(\beta z - \omega t)}, \tag{A.10f}$$

Inside the cladding $(a_1 \le r \le a_2)$:

$$E_z^{\text{cl}} = iE_{lm}C_{lm}\bar{n}\frac{u_2}{\beta}\left(-Jp_0(r) + \frac{n_2^2}{n_1^2}\frac{q_0(r)}{u_2}\right)e^{i(\beta z - \omega t)} \tag{A.11a}$$

$$E_r^{\text{cl}} = \left\{-\frac{u_2^2 n_1^2}{u_1 n_2^2}\right\}E_{lm}C_{lm}\bar{n}\frac{u_1}{u_2}\left(-Jr_0(r) + \frac{n_2^2}{n_1^2}\frac{s_0(r)}{u_2}\right)e^{i(\beta z - \omega t)} \tag{A.11b}$$

$$E_\phi^{\text{cl}} = 0 \tag{A.11c}$$

$$H_z^{\text{cl}} = 0 \tag{A.11d}$$

$$H_r^{\text{cl}} = 0 \tag{A.11e}$$

$$H_\phi^{\text{cl}} = \{u_2\}E_{lm}C_{lm}\frac{1}{Z_0}\left(-Jr_0(r) + \frac{n_2^2}{n_1^2}\frac{s_0(r)}{u_2}\right)e^{i(\beta z - \omega t)}. \tag{A.11f}$$

HE/EH fields

In cylindrical coordinates (r, ϕ, z), the electric $\mathbf{E}$ and magnetic $\mathbf{H}$ fields inside the core $(r < a_1)$ can be expressed in terms of Bessel functions J_n of the first kind as

$$E_z = E_{lm}\frac{u_1^2}{\beta}PJ_l(u_1r)\sin(l\phi+\varphi)e^{i(\beta z-\omega t)} \tag{A.12a}$$

$$E_r = iE_{lm}\frac{u_1}{2}\left[(1-P)J_{l-1}(u_1r)+(1+P)J_{l+1}(u_1r)\right]\sin(l\phi+\varphi)e^{i(\beta z-\omega t)} \tag{A.12b}$$

$$E_\phi = iE_{lm}\frac{u_1}{2}\left[(1-P)J_{l-1}(u_1r)-(1+P)J_{l+1}(u_1r)\right]\cos(l\phi+\varphi)e^{i(\beta z-\omega t)} \tag{A.12c}$$

$$H_z = E_{lm}\frac{\bar{n}}{Z_0}\frac{u_1^2}{\beta}J_l(u_1r)\cos(l\phi+\varphi)\,e^{i(\beta z-\omega t)} \tag{A.12d}$$

$$H_r = iE_{lm}\frac{\bar{n}}{Z_0}\frac{u_1}{2}\left[-\left(1-P\frac{n_1^2}{\bar{n}^2}\right)J_{l-1}(u_1r)+\left(1+P\frac{n_1^2}{\bar{n}^2}\right)J_{l+1}(u_1r)\right]\cos(l\phi+\varphi)\,e^{i(\beta z-\omega t)} \tag{A.12e}$$

$$H_\phi = -iE_{lm}\frac{\bar{n}}{Z_0}\frac{u_1}{2}\left[-\left(1-P\frac{n_1^2}{\bar{n}^2}\right)J_{l-1}(u_1r)-\left(1+P\frac{n_1^2}{\bar{n}^2}\right)J_{l+1}(u_1r)\right]\sin(l\phi+\varphi)\,e^{i(\beta z-\omega t)}, \tag{A.12f}$$

with the transverse wavevector $u_1 = (2\pi/\lambda)\sqrt{n_1^2-\bar{n}^2}$. The constant $Z_0 = \sqrt{\mu_0/\epsilon_0} \approx 376.7\Omega$ is the electromagnetic impedance in vacuum. Note that in these expressions $\bar{n}, \beta, u_1$ and P all depend on the mode indices l and m. In particular, the mode parameter

$$P = P_{lm} = -\frac{\bar{n}_{lm}i\zeta_0}{n_1^2} \tag{A.13}$$

characterizes the relative strength of the longitudinal field components, and is used to classify modes as HE or EH.

The expressions for the fields in the cladding and air regions are as follows: Inside the cladding $(a_1 \leq r \leq a_2)$:

$$E_z^{cl} = E_{lm}C_{lm}\frac{u_2^2\sigma}{n_2^2\beta l}\left[G_2 p_l(r)-\frac{n_2^2\zeta_0}{n_1^2u_2}q_l(r)\right]\sin(l\phi+\varphi)\,e^{i(\beta z-\omega t)} \tag{A.14a}$$

$$E_r^{cl} = iE_{lm}C_{lm}\left(-\frac{lF_2}{r}p_l(r)+\frac{l}{u_2r}q_l(r)-\frac{\sigma}{ln_2^2}\left[u_2G_2r_l(r)-\frac{n_2^2\zeta_0}{n_1^2}s_l(r)\right]\right)\sin(l\phi+\varphi)\,e^{i(\beta z-\omega t)} \tag{A.14b}$$

$$E_\phi^{cl} = -iE_{lm}C_{lm}\left(\frac{\sigma}{n_2^2}\left[\frac{G_2}{r}p_l(r)-\frac{n_2^2\zeta_0}{n_1^2u_2r}q_l(r)\right]+u_2F_2r_l(r)-s_l(r)\right)\cos(l\phi+\varphi)\,e^{i(\beta z-\omega t)} \tag{A.14c}$$

$$H_z^{\text{cl}} = iE_{lm}C_{lm}\frac{1}{Z_0}\frac{u_2^2\sigma}{\beta l}\left[F_2 p_l(r) - \frac{1}{u_2}q_l(r)\right]\cos(l\phi + \varphi)\,e^{i(\beta z - \omega t)} \tag{A.15a}$$

$$H_r^{\text{cl}} = -E_{lm}C_{lm}\frac{1}{Z_0}\left(l\frac{G_2}{r}p_l(r) - l\frac{n_2^2\zeta_0}{n_1^2 u_2 r}q_l(r) - \frac{\sigma}{l}\left[u_2 F_2 r_l(r) - s_l(r)\right]\right)\cos(l\phi + \varphi)\,e^{i(\beta z - \omega t)} \tag{A.15b}$$
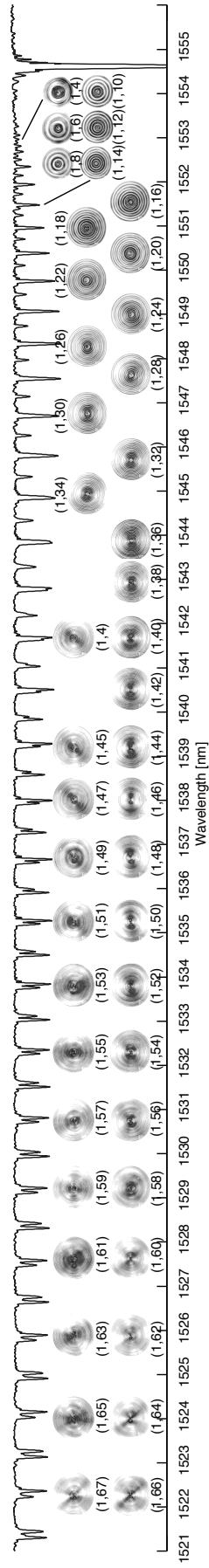
$$H_\phi^{\text{cl}} = -E_{lm}C_{lm}\frac{1}{Z_0}\left(\sigma\left[\frac{F_2}{r}p_l(r) - \frac{1}{u_2 r}q_l(r)\right] - u_2 G_2 r_l(r) + \frac{n_2^2\zeta_0}{n_1^2}s_l(r)\right)\sin(l\phi + \varphi)\,e^{i(\beta z - \omega t)} \tag{A.15c}$$
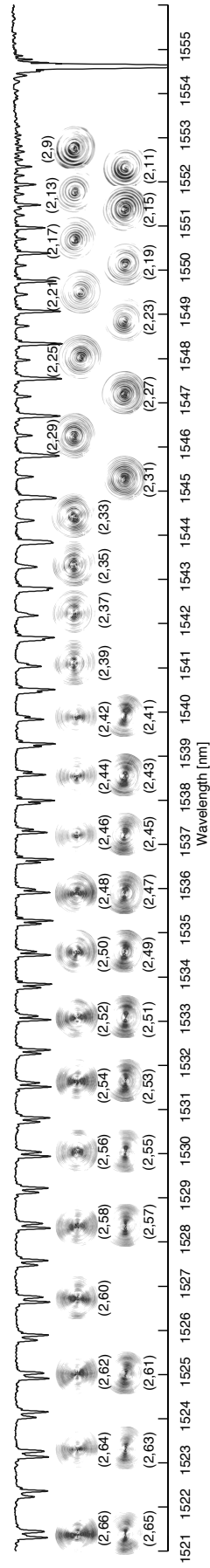
with the terms

$$C_{lm} = \frac{\pi a_1 u_{lm}^2 J_l(u_{lm}a_1)}{2}, \qquad F_2 = J - \frac{u_{21}\sigma\zeta_0}{n_1^2 a_1}, \qquad G_2 = \zeta_0 J + \frac{v_{21}\sigma}{a_1}. \tag{A.16}$$

B All imaged cladding modes

Bibliography

[And07] G. Androz, D. Faucher, M. Bernier, and R. Vallée, "Monolithic fluoride-fiber laser at 1480 nm using fiber Bragg gratings," Opt. Lett. **32**, 1302 (2007).

[And08] G. Androz, M. Bernier, D. Faucher, and R. Vallée, "23 W single transverse mode thulium-doped ZBLAN fiber laser at 1480 nm," Opt. Express **16**, 16019 (2008).

[Ban08] S. Bandyopadhyay, J. Canning, M. Stevenson, and K. Cook, "Ultrahigh-temperature regenerated gratings in boron-codoped germanosilicate optical fiber using 193 nm," Opt. Lett. **33**, 1917 (2008).

[Bec08] M. Becker, J. Bergmann, S. Brückner, M. Franke, E. Lindner, M. W. Rothhardt, and H. Bartelt, "Fiber Bragg grating inscription combining DUV sub-picosecond laser pulses and two-beam interferometry," Opt. Express **16**, 19169 (2008).

[Bec09] M. Becker, J. Bergmann, S. Brückner, E. Lindner, M. W. Rothhardt, K. Schuster, J. Kobelke, S. Unger, H. Bartelt, L. A. Fernandes, and P. V. S. Marques, "Fiber Bragg grating inscription with DUV femtosecond exposure and two beam interference," Proc. of SPIE **7386**, 73862Y (2009).

[Ber07] M. Bernier, D. Faucher, R. Vallée, A. Saliminia, G. Androz, Y. Sheng, and S. L. Chin, "Bragg gratings photoinduced in ZBLAN fibers by femtosecond pulses at 800 nm," Opt. Lett. **32**, 454 (2007).

[Ber09a] M. Bernier, D. Faucher, N. Caron, and R. Vallée, "Highly stable and efficient erbium-doped 28 µm all fiber laser," Opt. Express **17**, 16941 (2009).

[Ber09b] M. Bernier, Y. Sheng, and R. Vallée, "Ultrabroadband fiber Bragg gratings written with a highly chirped phase mask and infrared femtosecond pulses,"

Opt. Express **17**, 3285 (2009).

[Ber09c] M. Bernier, R. Vallée, B. Morasse, C. Desrosiers, A. Saliminia, and Y. Sheng, "Ytterbium fiber laser based on first-order fiber Bragg gratings written with 400nm femtosecond pulses and a phase-mask," Opt. Express **17**, 18887 (2009).

[BH04] J. Bland-Hawthorn, M. Englund, and G. Edvell, "New approach to atmospheric OH suppression using an aperiodic fibre Bragg grating," Opt. Express **12**, 5902 (2004).

[Bla10] R. J. Black and L. Gagnon, "Optical Waveguide Modes: Polarization, Coupling and Symmetry," McGrawHill (2010).

[Can08] J. Canning, "Fibre gratings and devices for sensors and lasers," Laser & Photon. Rev. **2**, 1 (2008).

[Dav96] K. M. Davis, K. Miura, N. Sugimoto, and K. Hirao, "Writing waveguides in glass with a femtosecond laser," Opt. Lett. **21**, 1729 (1996).

[Dür04] F. Dürr, H. Limberger, R. Salathé, F. Hindle, M. Douay, E. Fertein, and C. Przygodzki, "Tomographic measurement of femtosecond-laser induced stress changes in optical fibers," Appl. Phys. Lett. **84**, 4983 (2004).

[Eat08] S. M. Eaton, H. Zhang, M. L. Ng, J. Li, W.-J. Chen, S. Ho, and P. R. Herman, "Transition from thermal diffusion to heat accumulation in high repetition rate femtosecond laser writing of buried optical waveguides," Opt. Express **16**, 9443 (2008).

[Egg00] B. Eggleton, P. Westbrook, C. White, C. Kerbage, R. Windeler, and G. Burdge, "Cladding-mode-resonances in air-silica microstructure optical fibers," J. Lightwave Technol. **18**, 1084 (2000).

[Erd96] T. Erdogan and J. E. Sipe, "Tilted fiber phase gratings," J. Opt. Soc. Am. A **13**, 296 (1996).

[Erd97a] T. Erdogan, "Cladding-mode resonances in short- and long-period fiber grating filters," J. Opt. Soc. Am. A **14**, 1760 (1997).

[Erd97b] T. Erdogan, "Fiber grating spectra," J. Lightwave Technol. **15**, 1277 (1997).

[Erd00] T. Erdogan, "Cladding-mode resonances in short- and long-period fiber grat-

ing filters: errata," J. Opt. Soc. Am. A **17**, 2113 (2000).

[Fer98]   M. E. Fermann, "Single-mode excitationof multimode fibers with ultrashort pulses," Opt. Lett. **23**, 52 (1998).

[Fer01]   E. Fertein, C. Przygodzki, H. Delbarre, A. Hidayat, M. Douay, and P. Niay, "Refractive-Index Changes of Standard Telecommunication Fiber through Exposure to Femtosecond Laser Pulses at 810 cm," Appl. Opt. **40**, 3506 (2001).

[Gam06]   E. G. Gamaly, S. Juodkazis, K. Nishimura, H. Misawa, B. Luther-Davies, L. Hallo, P. Nicolai, and V. T. Tikhonchuk, "Laser-matter interaction in the bulk of a transparent solid: Confined microexplosion and void formation," Phys. Rev. B **73**, 214101, (c) 2006: The American Physical Society (2006).

[Gam07]   E. Gamaly, B. Luther-Davies, A. Rode, S. Joudkazis, H. Misawa, L. Hallo, P. Nicolai, and V. Tikhonchuk, "Laser-matter interaction in the bulk of transparent dielectrics: Confined micro-explosion," Journal of Physics: Conference Series **59**, 5 (2007).

[Gat08]   R. Gattass and E. Mazur, "Femtosecond laser micromachining in transparent materials," Nature Photonics **2**, 219 (2008).

[Got11]   R. Goto, R. J. Williams, N. Jovanovic, G. D. Marshall, M. J. Withford, and S. D. Jackson, "Linearly polarized fiber laser using a point-by-point Bragg grating in a single-polarization photonic bandgap fiber," Opt. Lett. **36**, 1872 (2011).

[Gra09]   E. Grace and S. Lewis, "Probing LMA optical fibres with real-time SLM," CLEO Europe Conference Digest CJ2.6–Wed (2009).

[Gro04]   D. Grobnic, C. W. Smelser, S. J. Mihailov, R. B. Walker, and P. Lu, "Fiber Bragg Gratings With Suppressed Cladding Modes Made in SMF-28 With a Femtosecond IR Laser and a Phase Mask," Photonics Technol. Lett. **16**, 1864 (2004).

[Han88]   D. P. Hand and P. S. J. Russell, "Solitary thermal shock waves and optical damage in optical fibers - The fiber fuse," Opt. Lett. **13**, 767 (1988).

[Hew96]   S. Hewlett, J. D. Love, G. Meltz, T. Bailey, and W. Morey, "Coupling characteristics of photo-induced Bragg gratings in Depressed-and matched-cladding fibre," Opt. and Quantum Electron. **28**, 1641 (1996).

[Hil78]   K. O. Hill, Y. Fujii, D. C. Johnson, and B. S. Kawasaki, "Photosensitivity in optical fiber waveguides: Application to reflection filter fabrication," Appl. Phys. Lett. **32**, 647, (c) 1978: American Institute of Physics (1978).

[Hil90]   K. O. Hill, B. Malo, K. A. Vineberg, F. Bilodeau, D. Johnson, and I. Skinner, "Efficient mode conversion in telecommunication fibre using externally written gratings," Electron. Lett. **26**, 1270 (1990).

[Ito06]   K. Itoh, W. Watanabe, and S. Nolte, "Ultrafast processes for bulk modification of transparent materials," MRS bulletin **31**, 620 (2006).

[Jet07]   S. Jetschke, S. Unger, U. Röpke, and J. Kirchhof, "Photodarkening in Yb doped fibers: experimental evidence of equilibrium states depending on the pump power," Opt. Express **15**, 14838 (2007).

[Jov07]   N. Jovanovic, M. Åslund, A. Fuerbach, S. D. Jackson, G. D. Marshall, and M. J. Withford, "Narrow linewidth, 100 W cw Yb-doped silica fiber laser with a point-by-point Bragg grating inscribed directly into the active core," Opt. Lett. **32**, 2804 (2007).

[Jov09]   N. Jovanovic, J. Thomas, R. J. Williams, M. J. Steel, G. D. Marshall, A. Fuerbach, S. Nolte, A. Tünnermann, and M. J. Withford, "Polarization-dependent effects in point-by-point fiber Bragg gratings enable simple, linearly polarized fiber lasers," Opt. Express **17**, 6082 (2009).

[Kai09]   T. Kaiser, D. Flamm, S. Schröter, and M. Duparré, "Complete modal decomposition for optical fibers using CGH-based correlation filters," Opt. Express **17**, 9347 (2009).

[Kao66]   K. Kao and G. Hockham, "Dielectric-fibre surface waveguides for optical frequencies," Electrical Engineers, Proceedings of the Institution of **113**, 1151 (1966).

[Kas99]   R. Kashyap, *Fiber Bragg gratings*, Academics Press (1999).

[Kaz07]   P. G. Kazansky, W. Yang, E. Bricchi, J. Bovatsek, A. Arai, Y. Shimotsuma, K. Miura, and K. Hirao, ""Quill" writing with ultrashort light pulses in transparent materials," Appl. Phys. Lett. **90**, 1120 (2007).

[Ker96]   A. Kersey, "A Review of Recent Developments in Fiber Optic Sensor Technol-

ogy," Optical Fiber Technology **2**, 291 (1996).

[Ker97]   Kersey, "Fiber grating sensors," Lightwave Technology, Journal of **15**, 1442 (1997).

[Kog79]   H. Kogelnik, "Theory of Dielectric Waveguides," Topics in Applied Physics **7**, 15 (1979).

[Lai06]   Y. Lai, A. Martinez, I. Khrushchev, and I. Bennion, "Distributed Bragg reflector fiber laser fabricated by femtosecond laser inscription," Opt. Lett. **31**, 1672 (2006).

[Lee00]   K. S. Lee and T. Erdogan, "Fiber Mode Coupling in Transmissive and Reflective Tilted Fiber Gratings," Appl. Opt. **39**, 1394 (2000).

[Lee01]   K. Lee and T. Erdogan, "Fiber mode conversion with tilted gratings in an optical fiber," J. Opt. Soc. Am. A **18**, 1176 (2001).

[Lin11a] E. Lindner, J. Canning, C. Chojetzki, S. Brückner, M. Becker, M. Rothhardt, and H. Bartelt, "Thermal regenerated type IIa fiber Bragg gratings for ultrahigh temperature operation," Optics Communications **284**, 183, elsevier B.V. (2011).

[Lin11b] E. Lindner, J. Canning, C. Chojetzki, S. Brueckner, M. Becker, M. Rothhardt, and H. Bartelt, "Post-hydrogen-loaded draw tower fiber Bragg gratings and their thermal regeneration," Appl. Opt. **50**, 2519 (2011).

[Loh98]   W. H. Loh, B. N. Samson, L. Dong, G. J. Cowle, and K. Hsu, "High Performance Single Frequency Fiber Grating-Based Erbium:Ytterbium-Codoped Fiber Lasers," Journal of Lightwave Technology **16**, 114 (1998).

[Mar75]   J. Marburger, "Self-focusing: Theory," Progress in Quantum Electronics **4**, 35 (1975).

[Mar04]   A. Martinez, M. Dubov, I. Khrushchev, and I. Bennion, "Direct writing of fibre Bragg gratings by femtosecond laser," Electron. Lett. **40**, 1170 (2004).

[Mar05]   A. Martinez, I. Khrushchev, and I. Bennion, "Thermal properties of fibre Bragg gratings inscribed point-by-point by infrared femtosecond laser," Electron. Lett. **41**, 176 (2005).

[Mar10]   G. Marshall, R. Williams, N. Jovanovic, M. J. Steel, and M. J. Withford, "Point-by-point written fiber-Bragg gratings and their application in complex grating designs," Opt. Express **18**, 19844 (2010).

[Mau10]   S. Mauger, L. Bergé, and S. Skupin, "Self-focusing versus stimulated Brillouin scattering of laser pulses in fused silica," New Journal of Physics **12**, 103049 (2010).

[Mih04]   S. J. Mihailov, C. W. Smelser, D. Grobnic, R. B. Walker, P. Lu, H. Ding, and J. Unruh, "Bragg Gratings Written in All-SiO2 and Ge-Doped Core Fibers With 800-nm Femtosecond Radiation and a Phase Mask," J. Lightwave Technol. **22**, 94 (2004).

[Mih08]   S. J. Mihailov, D. Grobnic, C. W. Smelser, P. Lu, R. B. Walker, and H. Ding, "Induced Bragg Gratings in Optical Fibers and Waveguides Using an Ultrafast Infrared Laser and a Phase Mask," Laser Chem. **2008**, 1 (2008).

[Mil00]   J. D. Mills, C. W. J. Hillman, B. H. Blott, and W. S. Brocklesby, "Imaging of Free-Space Interference Patterns Used to Manufacture Fiber Bragg Gratings," Appl. Opt. **39**, 6128 (2000).

[Mou09]   C. Mou, P. Saffari, H. Fu, K. Zhou, L. Zhang, and I. Bennion, "Single- and dual-wavelength switchable erbium-doped fiber ring laser based on intracavity polarization selective tilted fiber gratings," Appl. Opt. **48**, 3455 (2009).

[Nei02]   M. A. A. Neil, F. Massoumian, R. Juškaitis, and T. Wilson, "Method for the generation of arbitrary complex vector wave fronts," Opt. Lett. **27**, 1929 (2002).

[Nic08]   J. W. Nicholson, A. D. Yablon, S. Ramachandran, and S. Ghalmi, "Spatially and spectrally resolved imaging of modal content in large-mode-area fibers," Opt. Express **16**, 7233 (2008).

[Nol97]   S. Nolte, C. Momma, H. Jacobs, A. Tünnermann, B. N. Chichkov, B. Wellegehausen, and H. Welling, "Ablation of metals by ultrashort laser pulses," J. Opt. Soc. Am. B **14**, 2716 (1997).

[Nol03]   S. Nolte, M. Will, J. Burghoff, and A. Tuennermann, "Femtosecond waveguide writing: a new avenue to three-dimensional integrated optics," Appl. Phys. A **77**, 109 (2003).

[Oth97]   A. Othonos, "Fiber Bragg gratings," Review of Scientific Instruments (1997).

[PM05]   P. Pérez-Millián, J. Cruz, and M. Andrés, "Active Q-switched distributed feedback erbium-doped fiber lasers," Appl. Phys. Lett. **87**, 011104 (2005).

[Ram08]   S. Ramachandran, J. Fini, M. Mermelstein, J. W. Nicholson, S. Ghalmi, and M. F. Yan, "Ultra-large effective-area, higher-order mode fibers: A new strategy for high-power lasers," Laser & Photon. Rev. **2**, 429 (2008).

[Sal91]   B. E. A. Saleh, M. C. Teich, and J. W. Goodman, "Fundamentals of Photonics," Wiley (1991).

[Sha05]   O. Shapira, A. F. Abouraddy, J. D. Joannopoulos, and Y. Fink, "Complete Modal Decomposition for Optical Waveguides," Phys. Rev. Lett. **94**, 143902 (2005).

[Sha11]   L. Shao, J. Coyle, S. Barry, and J. Albert, "Anomalous permittivity and plasmon resonances of copper nanoparticle conformal coatings on optical fibers," Optical Materials Express **1**, 128 (2011).

[She08]   Y. Shevchenko, D. Blair, M. Derosa, and J. Albert, "DNA target detection using gold-coated tilted fiber Bragg gratings in aqueous media," "CLEO conference digest," CMJ4, Optical Society of America (2008).

[Sme04]   C. W. Smelser, D. Grobnic, and S. J. Mihailov, "Generation of pure two-beam interference grating structures in an optical fiber with a femtosecond infrared source and a phase mask," Opt. Lett. **29**, 17301732 (2004).

[Sme07]   C. W. Smelser, S. J. Mihailov, and D. Grobnic, "Characterization of Fourier components in type I infrared ultrafast laser induced fiber Bragg gratings," Opt. Lett. **32**, 1453 (2007).

[Sni61a]   E. Snitzer, "Cylindrical Dielectric Waveguide Modes," J. Opt. Soc. Am. **51**, 491 (1961).

[Sni61b]   E. Snitzer and H. Osterberg, "Observed Dielectric Waveguide Modes in the Visible Spectrum," J. Opt. Soc. Am. **51**, 499 (1961).

[Sny78]   A. W. Snyder and W. Young, "Modes of optical waveguides," J. Opt. Soc. Am. **68**, 297 (1978).

[Sny83]   A. Snyder, "Optical waveguide theory," books.google.com (1983).

[Son09]   C. W. Song, Y. J. Zhang, B. Q. Yao, Y. Wang, W. Wang, Y. L. Ju, and Y. Z. Wang, "Double-clad Tm3+-doped silica fiber laser with Bragg grating inscribed directly into active core by femtosecond laser," Laser Phys. **19**, 1009 (2009).

[SR11]   D. Sáez-Rodriguez, J. Cruz, A. Díez, and M. Andrés, "Fiber laser with combined feedback of core and cladding modes assisted by an intracavity long-period grating," Opt. Lett. **36**, 1839 (2011).

[Stu10]   F. Stutzki, C. Jauregui, C. Voigtländer, J. Thomas, J. Limpert, S. Nolte, and A. Tünnermann, "Passively stabilized 215-W monolithic CW LMA-fiber laser with innovative transversal mode filter," Proc. of SPIE **7580**, 75801K (2010).

[Stu11]   F. Stutzki, C. Jauregui, J. Limpert, and A. Tünnermann, "Real-time characterisation of modal content in monolithic few-mode fibre lasers," Electronics Letters **47**, 274 (2011).

[Suz08]   S. Suzuki, A. Schülzgen, and N. Peyghambarian, "Single-mode fiber laser based on core-cladding mode conversion," Opt. Lett. **33**, 351 (2008).

[Tho07]   J. Thomas, E. Wikszak, T. Clausnitzer, U. Fuchs, U. Zeitner, S. Nolte, and A. Tünnermann, "Inscription of fiber Bragg gratings with femtosecond pulses using a phase mask scanning technique," Appl. Phys. A **86**, 153 (2007).

[Tho11a] J. Thomas, M. Heinrich, P. Zeil, V. Hilbert, K. Rademaker, R. Riedel, S. Ringleb, C. Dubs, J.-P. Ruske, S. Nolte, and A. Tünnermann, "Laser direct writing: Enabling monolithic and hybrid integrated solutions on the lithium niobate platform," Phys. Stat. Sol. A **208**, 276 (2011).

[Tho11b] J. Thomas, N. Jovanovic, R. G. Becker, G. D. Marshall, M. J. Withford, A. Tünnermann, S. Nolte, and M. J. Steel, "Cladding mode coupling in highly localized fiber Bragg gratings: modal properties and transmission spectra," Opt. Express **19**, 325 (2011).

[Tsa89a] C. Tsao, D. Payne, and W. Gambling, "Modal characteristics of three-layered optical fiber waveguides: a modified approach," J. Opt. Soc. Am. A **6**, 555 (1989).

[Tsa89b] C. Y. H. Tsao, D. N. Payne, and W. A. Gambling, "Modal characteristics of

three-layered optical fiber waveguides: a modified approach," J. Opt. Soc. Am. A **6**, 555 (1989).

[Tün05]   A. Tünnermann, T. Schreiber, F. Röser, A. Liem, S. Höfer, H. Zellmer, S. Nolte, and J. Limpert, "The renaissance and bright future of fibre lasers," Journal of Physics B: Atomic **38**, S681 (2005).

[Val07]   R. Vallée, M. Bernier, A. Saliminia, and S. L. Chin, "Fiber Bragg Gratings Based on 1D Filamentation of Femtosecond Pulses," Bragg Gratings, Photosensitivity, and Poling in Glass Waveguides BWB3 (2007).

[Voi09]   C. Voigtländer, J. Thomas, E. Wikszak, P. Dannberg, S. Nolte, and A. Tünnermann, "Chirped fiber Bragg gratings written with ultrashort pulses and a tunable phase mask," Opt. Lett. **34**, 1888 (2009).

[Voi11]   C. Voigtländer, R. G. Becker, J. Thomas, D. Richter, A. Singh, A. Tünnermann, and S. Nolte, "Ultrashort pulse inscription of tailored fiber Bragg gratings with a phase mask and a deformed wavefront," Opt. Materials Express **1**, 633 (2011).

[Wal09]   R. B. Walker, S. J. Mihailov, D. Grobnic, P. Lu, and X. Bao, "Direct evidence of tilted Bragg grating azimuthal radiation mode coupling mechanisms," Opt. Express **17**, 14075 (2009).

[Wik04]   E. Wikszak, J. Burghoff, M. Will, and S. Nolte, "Recording of fiber Bragg gratings with femtosecond pulses using a" point by point" technique," Conference on Lasers and Electro-Optics, San Francisco, California CThM7 (2004).

[Wik06]   E. Wikszak, J. Thomas, J. Burghoff, B. Ortaç, J. Limpert, S. Nolte, U. Fuchs, and A. Tünnermann, "Erbium fiber laser based on intracore femtosecond-written fiber Bragg grating," Opt. Lett. **31**, 2390 (2006).

[Wik07]   E. Wikszak, J. Thomas, S. Klingebiel, B. Ortaç, J. Limpert, S. Nolte, and A. Tünnermann, "Linearly polarized ytterbium fiber laser based on intracore femtosecond-written fiber Bragg gratings," Opt. Lett. **32**, 2756 (2007).

[Wik09]   E. Wikszak, "Inscription of fiber Bragg gratings in non-photosensitive and rare-earth doped fibers applying ultrafast lasers," PhD Thesis 1–112 (2009).

[Wil04]   M. Will, "Ultrakurzpulsinduzierte Brechzahlmodifikationen in transparenten

Festkörpern," PhD Thesis (2004).

[Zha09a] Y. Zhang, C. Song, and W. Wang, "Multi-peak output Tm-doped silica fiber laser based on femtosecond-written multi-mode fiber Bragg grating," Laser Phys. **19**, 1854 (2009).

[Zha09b] Y. J. Zhang, W. Wang, S. F. Song, and Z. G. Wang, "Ultra-narrow linewidth Tm3+-doped fiber laser based on intra-core fiber Bragg gratings," Laser Phys. Lett. **6**, 723 (2009).

[Zho06]   K. Zhou, L. Zhang, X. Chen, and I. Bennion, "Optic sensors of high refractive-index responsivity and low thermal cross sensitivity that use fiber Bragg gratings of >80° tilted structures," Opt. Lett. **31**, 1193 (2006).

Zusammenfassung

Um Licht effizient zu leiten, werden in der modernen Optik Spiegel, Prismen und Linsen mehr und mehr durch Glasfasern ersetzt. Innerhalb der Faser kann sich das Licht nur noch in bestimmten Transversalzuständen ausbreiten, den sogenannten "Moden". Je kleiner die Geometrie des Wellenleiters ist, desto weniger unterschiedliche Moden werden unterstützt. Monomodefasern besitzen einen Faserkern, der nur eine einzige Mode führt. Mit solchen Fasern können Lichtsignale nahezu verlustfrei über hunderte Kilometer übertragen werden [Kao66]. Aus diesem Grund bilden sie heute das Rückgrat nahezu aller terrestrischen Telekommunikationsnetzwerke. Lichtleitfasern, die höhere Moden unterstützen, werden hingegen als Sensoren eingesetzt, um zum Beispiel Temperaturen, Zug- und Dehnungsspannungen, Beschleunigung oder Flüssigkeiten zu vermessen. Da diese Sensoren sehr robust sind und günstig in grosser Stückzahl hergestellt werden können, finden sie weite Verbreitung angefangen von den Lebenswissenschaften bis hin zu den "intelligenten Bauten" moderner Architektur [Ker96].

Darüber hinaus werden seltenerdotierte Glasfasern für moderne Lasersysteme eingesetzt. Dies hat mehrere Gründe: Aufgrund des großen Verhältnisses von Oberfläche zu Volumen besitzen Fasern hervorragende thermo-optische Eigenschaften. Sehr gute Strahlqualität kann auch bei Leistungsskalierung erhalten werden. Hervorragende Pumplichtabsorption und Effizienz werden durch die große Wechselwirkungslänge erreicht. Der Nachteil dieses Konzeptes ist allerdings, dass die starke Führung des Lichtes nichtlineare Effekte wie stimulierte Raman Streuung begünstigt. Um diese Effekte zu begrenzen muss die Leistungsdichte reduziert werden, was durch Vergrößerung des Querschnitts des Faserkerns erreicht werden kann. Mit Großkernfasern erreichen kommerzielle Faserlasersysteme mittlerweile Ausgangsleistungen von über zehn Kilowatt [Tün05].

Für alle diese Anwendungsfelder von Glasfasern besteht ein großer Bedarf klassische Optiken durch faserintegrierte Komponenten zu ersetzen. Hier bilden faserintegrierte Beugungsgitter die Grundlage, um schmal- und breitbandige Filter, Spiegel und Modenkonverter ohne externe Elemente zu realisieren [Hil78, Hil90]. Sogenannte *Faser-Bragg-Gitter* (FBG), die als Reflektoren eingesetzt werden, besitzen Gitterperioden, die meist kleiner als ein Mikrometer sind. Um zwischen Moden zu konvertieren, die sich in die selbe Richtung ausbreiten, muss hingegen eine weitaus geringere Phasendifferenz überwunden werden, weshalb die Perioden solcher *langperiodischer Gitter* (LPG) von einigen hundert Mikrometer bis in den Millimeterbereich reichen können.

Etablierte Einschreibetechniken basieren auf einem Brechzahlhub, der durch Absorption von ultraviolettem Licht im Glas ausgelöst wird. Die Bandlücke des Glases ist jedoch meist zu groß für solche Absorptionsprozesse und muss deshalb durch die Dotierung mit Defekt-Ionen gesenkt werden. Aus diesem Grund werden die Faserkerne in einem zusätzlichen Prozess vor der Einschreibung beispielsweise Bor oder Wasserstoff ausgesetzt [Kas99], was die Photoempfindlichkeit erhöht. Mit dieser Technik können in Single-Mode-Fasern Faser-Gitter mit nahezu beliebig komplexen spektralen Eigenschaften realisiert werden [BH04]. Allerdings stößt die UV-Lasereinschreibetechnik bei seltenerddotierten Fasern an ihre Grenzen, da hier bei den Konzentrationen der verschiedenen Dotierungselemente Kompromisse nötig sind [Loh98, PM05].

Zusätzlich verlängern sich bei Großkernfasern sowohl der Prozess der Photoempfindlichkeitserhöhung als auch die Belichtungszeit selbst. Daher werden die Fasergitter bisher in seperaten, photoempfindlichen Fasern realisiert, die anschließend mit der seltenerddotierten Faser durch Spleiße verbunden werden. Für diese Lösung müssen die Modenfeldgrößen der verschieden Faserstücke angepasst werden, was üblicherweise mittels verjüngten Fasern, sogenannten "Tapern", erreicht wird. All diese Lösungsansätze erweisen sich jedoch als problematisch [Han88], wenn die Ausgangsleistung des Faserlasers gesteigert werden soll. Zudem können im photoempfindlichen Fasermaterial leistungsmindernde Schwärzungseffekte auftreten [Jet07].

In den letzten Jahren konnte durch Einsatz von Ultrakurzpulslaser hochpräzise Mikromaterialbearbeitung von Metallen [Nol97], Gläsern [Dav96, Nol03, Gat08] und Kristallen [Tho11a] demonstriert werden. In transparenten Medien ist es möglich mit fokussierten,

ultrakurzen Pulsen so große Lichtleistungsdichten zu erreichen, dass nicht-lineare Absorptionsprozesse ausgelöst werden, die zu permanenter Strukturänderung führen [Ito06]. Da diese Modifikationen meist auf den konfokalen Bereich beschränkt sind, können dreidimensionale Strukturen mittels Bewegung der Probe innerhalb des Materials geschrieben werden [Nol03, Gat08].

Heute werden Ultrakurzpulslaser mehr und mehr für die Fasergittereinschreibung eingesetzt [Fer01, Mih04, Mar04, Tho07, Bec08]. Durch die herausragenden Eigenschaften der nicht-linearen Photoabsorption, können nun Fasergitter direkt in photounempfindliche [Fer01], insbesondere seltenerddotierte Fasern [Mar04, Wik06] mit hohem Kontrast und niedrigen Verlusten [Mar10] eingeschrieben werden. Außerdem weisen ultrakurzpulsgeschriebene Fasergitter eine Temperaturresistenz bis zu 1000° C auf [Mar05].

Ultrakurzpulslaser erlauben ebenfalls Fasergittergeometrien, die weitgehend unabhängig von der Faser sind: Die ansonsten benötigte Photoempfindlichkeit des Kerns schränkt nicht länger die möglichen Brechzahländerungen ein. Stattdessen kann die Querschnittsfläche des Gitters mittels der Fokussierung des Einschreibelasers vorgegeben werden. *Großflächige FBG* (LCFBG) sind nun möglich, ebenso wie *hochlokalisierte FBG* (HLFBG), die nur einen kleinen Teil des Faserkerns ausfüllen. Diese Dissertation behandelt die neuen Möglichkeiten, die Reflektionseigenschaften dieser Fasergitter in mehr- und hochmodigen Fasern durch ihren Querschnitt maßzuschneidern.

Im Gegensatz zu herkömmlichen Fasergittern können nun weitaus mehr Moden durch das ultrakurzpulsgeschriebene Fasergitter interagieren, da die Geometrie des Gitters nicht mehr eingeschränkt ist. Speziell die Kopplung zu höheren Azimuthalmoden ist nun möglich. Daher war es notwendig, bestehende theoretische Grundlagen der Fasergitteroptik [Erd97a, Lee01] zu erweitern, um diese Moden ebenfalls zu berücksichtigen. Basierend auf dem Ansatz der gekoppelten Moden [Kog79] und den analytischen Vektorfeldausdrücken für Stufenindexfasern [Sni61a, Sny78, Tsa89b] wurde das fundamentale Kopplungsverhalten für gebundene Kern- und Mantelmoden untersucht.

Für die experimentelle Analyse der Kopplungseigenschaften müssen die Spektren der Fasergitter mit räumlichen Messungen ergänzt werden. Intensität und Polarization sind nötig, um den Modeninhalt zu beschreiben. Mittels eines rechnergesteuerten Holo-

gramms konnten die spektralen Eigenschaften der FBG für unterschiedliche Modenanregung vermessen werden. Außerdem erlaubte die detailierten Analyse der Mantelmodenresonanzen, den Anteil von höheren Azimuthalmoden zu identifizieren [Tho11b].

Diese experimentellen Methoden und das theoretische Gerüst ermöglichen nun, die räumlichen Eigenschaften der Fasergitter hinsichtlich spezieller Anwendungen zu konzipieren. So wurde zum Beispiel ein hochreflektierendes FBG mit Unterdrückung von Modenkonversion in eine Ytterbium-dotierte Großkernfaser eingeschrieben. Ein monolitischer Faserresonator konnte mit diesem Element stabil bei hohen Leistungen auf zwei Moden betrieben werden. In monomodigen Fasern kann das Koppeln zu Mantelmoden mit der radialen Position des HLFBG gesteuert werden. Diese Eigenschaft ermöglicht das Optimieren des Koppelns in höhere Moden hinsichtlich Sensor- und Konversionsanwendungen.

Ultrakurzpulsgeschriebene FBG stellen daher eine neue Generation faserintegrierter Elemente dar. Weitere Forschungsarbeiten werden sich der Fragestellung widmen, wie die transversalen Kopplungseigenschaften mit longitudinalen Konzepten wie Apodization und Fabry-Perot-Resonatoren kombiniert werden können, um das Modenverhalten noch feiner zu beeinflussen.

Acknowledgements

---

[1]Who is better known under his real name Dr. Awesome.

Erklärung

Ich erkläre hiermit ehrenwörtlich, dass ich die vorliegende Arbeit selbständig und ohne unzulässige Hilfe Dritter sowie ohne Benutzung anderer als der angegebenen Hilfsmittel und Literatur angefertigt habe. Aus anderen Quellen direkt oder indirekt übernommene Daten und Konzepte sind unter Angabe der Quellen gekennzeichnet.

Bei der Auswahl und Auswertung folgendes Materials haben mir die nachstehend aufgeführten Personen in der jeweils beschriebenen Weise unentgeltlich geholfen:

1. Graham Marshall und Nemanja Jovanovic: Herstellung der hochlokalisierten Fasergitter,

2. Edward Grace: Algorithmus zur Echtzeit-Ansteuerung des Spatial-Ligtht-Modulators.

Weitere Personen waren an der inhaltlich-materiellen Erstellung der vorliegenden Arbeit nicht beteiligt. Insbesondere habe ich hierfür nicht die entgeltliche Hilfe von Vermittlungs- bzw. Beratungsdiensten („Promotionsberatern"oder anderen Personen) in Anspruch genommen. Niemand hat von mir unmittelbar oder mittelbar geldwerte Leistungen für Arbeiten erhalten, die im Zusammenhang mit dem Inhalt der vorgelegten Dissertation stehen.

Die Arbeit wurde bisher weder im In- noch im Ausland in gleicher oder ähnlicher Form einer anderen Prüfungsbehörde vorgelegt.

Teile dieser Arbeit wurden aus Prioritätsgründen bereits veröffentlicht bzw. zur Veröffentlichung eingereicht.

Die geltende Promotionsordnung der Physikalisch-Astronomischen Fakultät ist mir bekannt.

Ich versichere ehrenwörtlich, dass ich nach bestem Wissen die reine Wahrheit gesagt und nichts verschwiegen habe.

Jena, 6. Januar 2012   Jens Ulrich Thomas